# A Study of Homogenization and Precipitation Hardening Behaviour of Mg-Ca-Zn Alloys

by

Ashkan Shadkam

A thesis
presented to the University of Waterloo
in fulfillment of the
thesis requirement for the degree of
Master of Applied Science
in
Mechanical Engineering

Waterloo, Ontario, Canada, 2008

## AUTHOR'S DECLARATION

I hereby declare that I am the sole author of this thesis. This is a true copy of the thesis, including any required final revisions, as accepted by my examiners.

I understand that my thesis may be made electronically available to the public.

# Abstract

Microstructural evolution during heat treatment and the precipitation hardening response of Mg-Ca-Zn alloys were investigated. The binary Mg-2.5Ca alloy was chosen as the base alloy and the effects of adding one and two wt% zinc on the microstructural characteristics and precipitation hardening of the alloy system were studied. The as-cast microstructure of all three alloys showed dendritic solidification of α-Mg and the formation of the eutectic mixtures and/or multiple phases within the interdendritic regions. Homogenization heat treatment of the binary alloy removed the dendritic structure of α-Mg and spherodized the lamellar eutectic of α-Mg+$Mg_2Ca$. Homogenization heat treatment in the ternary Mg-Ca-Zn alloys resulted in the formation of α-Mg grains with $Mg_2Ca$ and zinc-containing particles mainly dispersed along the grain boundaries. The EDS analysis suggested that zinc is incorporated in $Mg_2Ca$ particles. To study the precipitation hardening response of the alloys, homogenized alloys were aged at 175°C, 200°C and 220°C. At all three isothermal aging temperatures, the binary alloy showed only a slight increase in hardness, i.e. from 50 VHN in the homogenized state to approximately 53 VHN when peak aged. On the other hand, adding zinc was found to promote the age hardening response of the ternary alloys and caused the hardness to increase up to 70 VHN at the peak-aged condition. To further study the precipitation hardening behavior of the alloys, DSC and IC studies were conducted on the homogenized, as–quenched, alloys. The DSC result of the binary alloy showed only one exothermic heat effect, while the ternary alloys showed multiple exothermic peaks. Analysis of the DSC and IC traces, along with the evaluation of the slight increase in microhardness, suggested that non-coherent equilibrium precipitates formed in the aged binary alloy. In addition, it was suggested that the formation of coherent precipitates during aging can be the cause of the pronounced increase in hardness in the aged ternary alloys. The IC traces of the alloys were used to evaluate the kinetics of precipitation in the ternary alloys. It was concluded that increasing aging temperature from 175°C to 220°C greatly increased the precipitation rate. Finally

the JMAK model was fit to the experimentally analyzed data for the evolution of the relative volume fraction of precipitates. It was found that the experimentally analyzed data was reasonably well described by the JMAK model. The corresponding JMAK kinetic parameters k and n were relatively close for the two ternary alloys at any aging temperature. The temperature dependence of k was modeled using the Arrhenius-type rate relationship. This analysis resulted in a smaller value for the apparent activation energy in the ternary alloy containing the higher zinc level, i.e. in Mg-2Ca-2Zn alloy.

# Acknowledgements

Many individuals helped me throughout this work that I should take this opportunity to acknowledge them. First, I would like to thank my academic supervisor Prof. Shahrzad Esmaeili for all the helpful discussions we had during my studies at the University of Waterloo. I take this opportunity to express my warm and sincere thanks for her support and patience with me. Her deep insight into the topic and solutions she suggested to tackle problems are greatly acknowledged.

I would also like to thank Dr. Youqan Ding at the electron microscopy laboratory at the University of Waterloo for all the helpful suggestions during my SEM works. Dr. Xiaogang Li is also warmly thanked for the assistance with the XRD experiments and analysis.

Dr. Daryoush Emadi for supplying as-cast bars and all contributions to this project, and Dr. V.Y.Gertsman for conducting TEM investigations both from CANMET-MTL are warmly thanked. Mr. Paul Mason from Thermo-calc Software Inc. is also thanked for providing the melting points for Mg-Ca-Zn alloys.

During my studies at Waterloo, I had the opportunity to meet some great individuals. I would like to thank Dr.Hari Simha for all the discussions we had over long Sunday nights. I want to thank my group members, Panthea Sepehrband, Roger Carrick and especially Brian Langelier for the assistance in metallography preparation and microhardness measurments. Our former group member, Dan Cluff is greatly appreciated for all constructive comments and discussions on the best way to present the experimental results. I should not forget to thank a good friend of mine, Alex Bardelick, PhD candidate from solid mechanics group, for all the good moments we had over coffee. Also, Ali Mohebi, a really good friend of mine is greatly thanked for all the encouragement he gave me during my last term at the University of Waterloo.

Financial support for the present investigation was provided by NSERC Canada and is greatly acknowledged. CANMET-MTL is also appreciated for supporting this project through an AUAF program grant.

Finally, I want to extend my warm and sincere thanks to three individuals whom without their love, support and encouragement I would never have been able to stand at this point of my life. My parents, Halleh and Ali, are warmly thanked for all their supportive calls and e-mails during my 2 years in graduate studies in Sweden and Canada. They have always firmly stood up by my side and believed in me. I should not forget my kind brother, Arash who always loves and supports me. And last not least, I want to thank my kind uncle, Alireza, who has been a great friend of mine through my life.

## Dedication

*I take this opportunity to dedicate this thesis to my parents, Halleh and Ali for their unconditional love, support and dedication.*

# Table of Contents

# List of Tables



.

# List of Figures

# Chapter 1
# Introduction

Magnesium alloys offer exceptional properties such as light weight, e.g. the lowest density of constructional metallic materials, good castability and recyclablity [Mordike and Ebert 200l]. Currently dramatic emphasis is placed on weight reduction in the transportation sector to minimize car emissions, and there is renewed interest in magnesium alloys with a focus on developing novel alloys to be used in powertrain components [King 2007]. Conventional magnesium alloys, e.g. Mg-Al-Zn (AZ) and Mg-Al-Mn (AM), have applications limited to 150°C due to poor creep and corrosion resistance [Gao *et al.* 2005]. Due to the aforementioned limitations there is a need for the development of high temperature magnesium alloys for use in the transportation industry.

Recently, calcium (Ca) has been reported to be effective in promoting creep resistance of Mg alloys [Suzuki *et al*. 2005]. The commercial AXJ530 (Mg-5Al-3Ca-0.15Sr, wt.%) is reported to have superior creep properties than those of the AE42 (Mg-4Al-2RE, wt.%), the benchmark in creep resistant magnesium alloys [Suzuki *et al*. 2005]. Zinc has been added to magnesium alloys to increase hardness by solid solution hardening [Polmear 2006]. In addition, Mg-Zn alloys show precipitation hardening potential and specifically, it is reported that zinc enhances the precipitation hardening response of Mg-Ca alloys [Nie and Muddle 1997, Bamberger *et al*. 2006, Oh *et al*. 2005].

Current available research regarding physical metallurgy of Mg-Ca-Zn alloys is small, and the present research aims to further the knowledge of microstructure and precipitation

hardening in this novel alloy system. In the present investigation, the dilute Mg- 2.5 wt% Ca system is considered as the basis for the alloy development. Zinc is added to the base Mg-Ca alloy as the second alloying element. The microstructural evolution and precipitation hardening response of the alloys are investigated using optical and electron microscopy, microhardness, thermal analysis (DSC and IC) and XRD techniques. A literature survey indicates that DSC and IC analysis in magnesium alloys is rarely performed and this research brings new perspective to studying precipitation behavior in Mg alloys.

# Chapter 2
# Literature Review

## 2.1 Introduction

In this chapter an introduction to the general properties of magnesium and commercially available magnesium alloys will be provided. This will be followed by a brief discussion on the development of novel magnesium alloys. Phase diagrams and microstructural characteristics of Mg-Ca-Zn alloys will be discussed. This chapter will also emphasize the physics behind homogenization heat treatments of as-cast microstructures and precipitation hardening mechanisms in all alloys, and specifically in Mg alloys. Discussion on precipitation hardening behavior of Mg-Ca-Zn alloys will bring an end to this chapter.

## 2.2 Magnesium Alloys

### 2.2.1 General Considerations

Magnesium is the fourth most abundant element following iron, oxygen and silicon, with resources of 190 times of nickel and cobalt [Watari 2006]. Raw ores of magnesium are: $MgCO_3.CaCO_3$ (dolomite) and $MgCO_3$ (magnesite). Magnesium is industrially manufactured via electrolysis and thermal reduction [Watari 2006]. Although magnesium was discovered by Davy in 1808, for the first time it was industrially used in the $20^{th}$ century [Mordike and Ebert 2001]. Magnesium production has witnessed fluctuations through 20th century, from production peak at World War II, i.e. 228 kt, to the production recession afterwards [King 2007]. Since late 1990s there has been a renewed interest to use magnesium alloys in the

automotive and aviation industries; in 2000 magnesium production reached close to 400kt [King 2007]. Current industrial magnesium applications are presented in Figure 2.1.

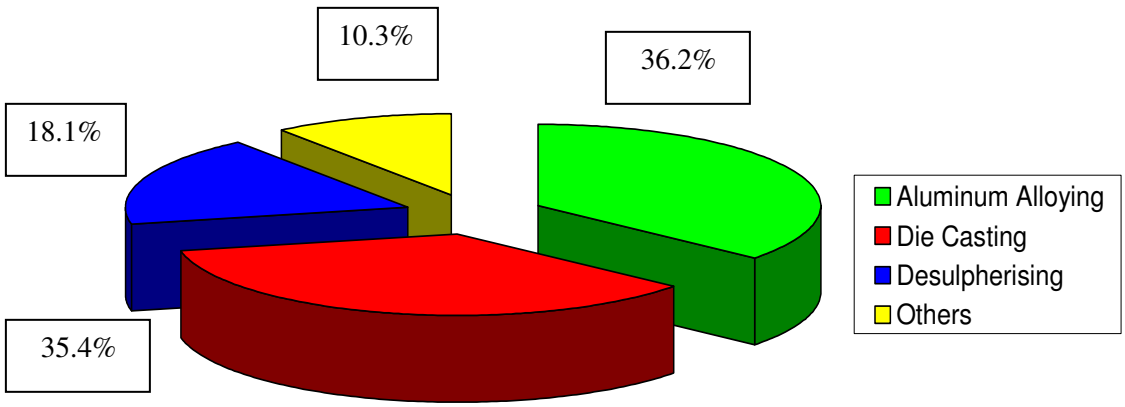


Figure 2.1: Industrial applications of Magnesium in 2003 [King 2007].

Comparing physical properties of magnesium presented in Table 2.1 with those of mainstream constructional metals, i.e. iron and aluminum, highlights advantages of magnesium over these metals in terms of light weight and high specific strength. Aside from physical properties, key features of mechanical behavior of magnesium stem from HCP crystal structure, and its atomic diameter of (0.320 nm) that favors solid solubility of a broad range of alloying elements notably aluminum and zinc [Polmear 2006]. The HCP crystal structure of magnesium inherently lowers its workability compared to the FCC aluminum and therefore only hot working of magnesium can successfully be performed [Hosford 2005]. On the other hand, the Hall-Petch relationship has four times more significance in

magnesium mechanical properties than in aluminum suggesting grain refinement is an important aspect of tailoring mechanical properties of magnesium alloys [Watari 2006].

Table 2.1: Physical properties of Mg, Fe and Al [Watari 2006].

| Metal name | Specific gravity | Melting point (°C) | Boiling point (°C) | Latent heat of melting (kJ/kg, J/cm³) | Specific heat (kJ/kg·K, J/cm³·K) | Coefficient of linear expansion x $10^6$ | Tensile strength (MPa) | Elongation | Hardness HB |
|---|---|---|---|---|---|---|---|---|---|
| Mg | 1.74 | 650 | 1110 | 368, 640 | 1.05, 1.84 | 25.5 | 98 | 5 | 30 |
| Al | 2.74 | 660 | 2486 | 398, 1088 | 0.88, 2.43 | 23.9 | 88 | 45 | 23 |
| Fe | 7.86 | 1535 | 2754 | 272, 213 | 0.46, 3.68 | 11.7 | 265 | 45 | 67 |

The most important advantages of magnesium and its alloys are [Polmear 2006, Mordike and Ebert 2001]:

- High specific strength
- Good castability
- Good machinability due to the soft texture
- Recyclability

### 2.2.2 Commercial Magnesium Alloys

The aim of adding alloying elements to pure magnesium is to increase the strength and low corrosion resistance of pure magnesium and enhance creep resistance of magnesium

[Mordike and Ebert 2001]. Mainstream magnesium alloys are classified as AZ (Mg-Al-Zn) and AM (Mg-Al-Mn) series. Aluminum and zinc increase strength by solid solution hardening. Aluminum also increases castability, making the alloys suitable for die-casting [Hu *et al.* 2003]. Manganese removes impurities such as Fe and Cu from Mg, resulting in substantial increase in a corrosion resistance [Polmear 2006].

Wrought magnesium alloys, i.e. ZK60 (Mg-Zn-Zr), ZM21 and AZ alloys are mainstream magnesium alloys for extrusion products [Bettles and Gibsson 2005]. Zirconium in ZK series is well known to refine the grain structure of Mg alloys and increases the tensile yield strength and toughness [Polmear 2006]. Wrought alloys offer superb tensile properties to their cast counterparts even though there is a yield point asymmetry arising from a strong formed texture [Bettles and Gibson 2005]. Somekawa and Mukai [2007] have recently shown that hot extrusion of Mg-0.3 at% Ca-1.8 at% Zn resulted in good balance of yield strength and fracture toughness, Fig 2.3, which are higher than those of the conventional wrought magnesium alloys.

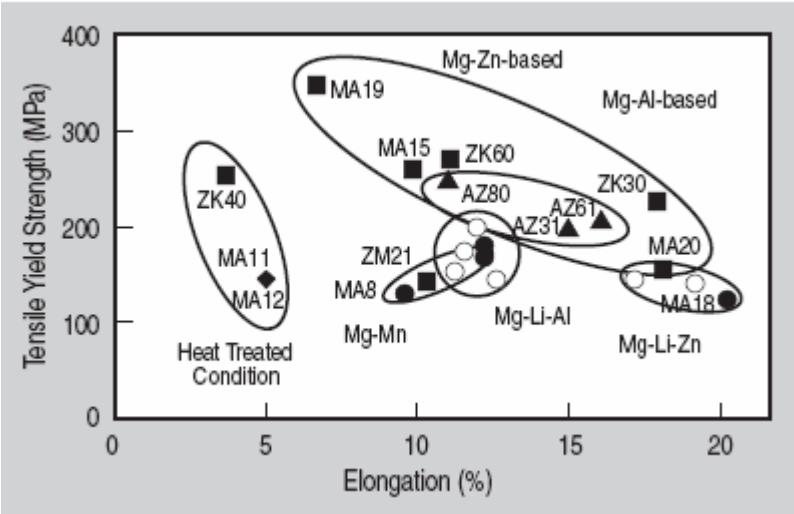


Figure 2.2: Tensile Strength and elongation for the most common commercial wrought magnesium alloys presented by solid symbols while number of experimental alloys are shown by open circles [Bettles and Gibson 2005].

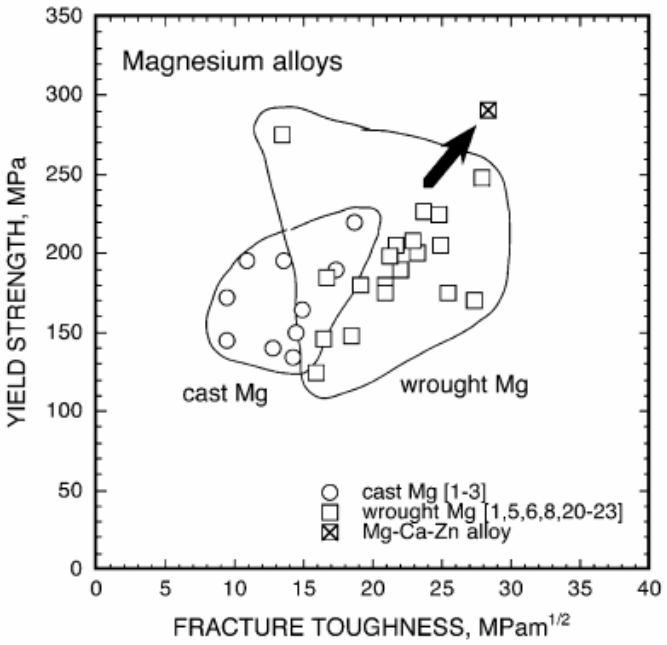


Figure 2.3**:** The relationship between yield strength and fracture toughness of magnesium alloys [Somekawa and Mukai 2007].

### 2.2.3 Novel Magnesium Alloy Development

Alloy development in magnesium is an effort to achieve specific requirements such as creep resistance, ductility, or high specific strength. Fig 2.4 summarizes the different directions taken in the development of magnesium alloys.

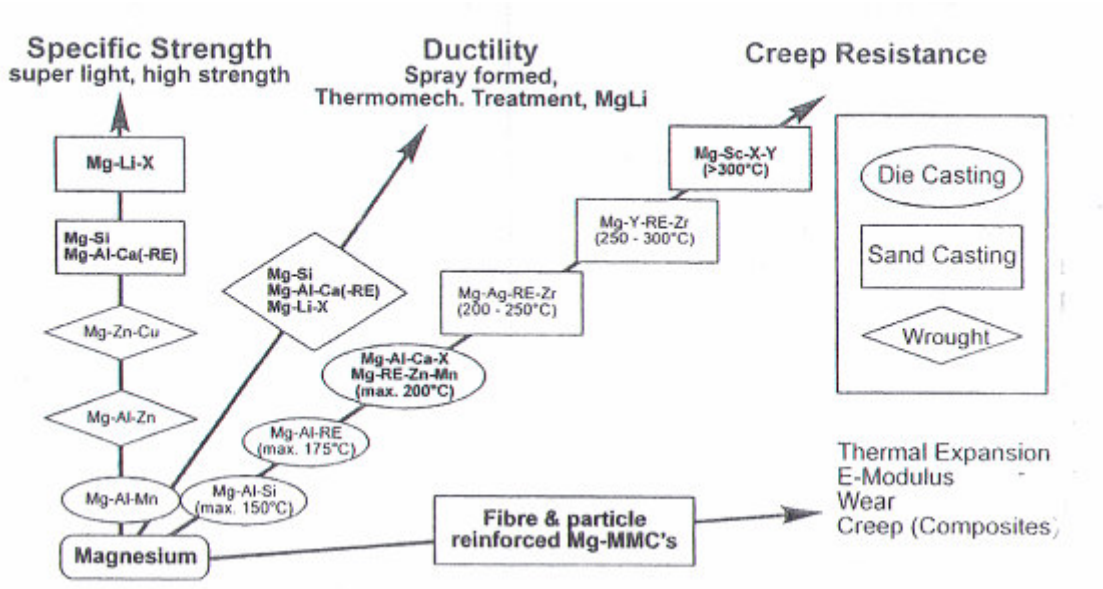


Figure 2.4: Directions in magnesium alloy development [Mordike and Ebert 2001].

In recent years, magnesium alloy development is targeting new auto, aerospace and biomedical applications [Beals *et al.* 2007]. For instance, efforts in developing new magnesium alloys suitable for powertrain applications have resulted in the production of AJ62 (Mg-6Al-2Sr-0.4MN), utilized in BMW engine blocks [King 2007], and AE44 (Mg-4Al-4RE), utilized in GM engine cradles [Bettles and Gibson 2005]. Meanwhile, alloy

systems containing Sc and Gd offering higher creep resistance are candidates for aerospace engine applications [Beals *et al.* 2007, Suzuki *et al* 2005].

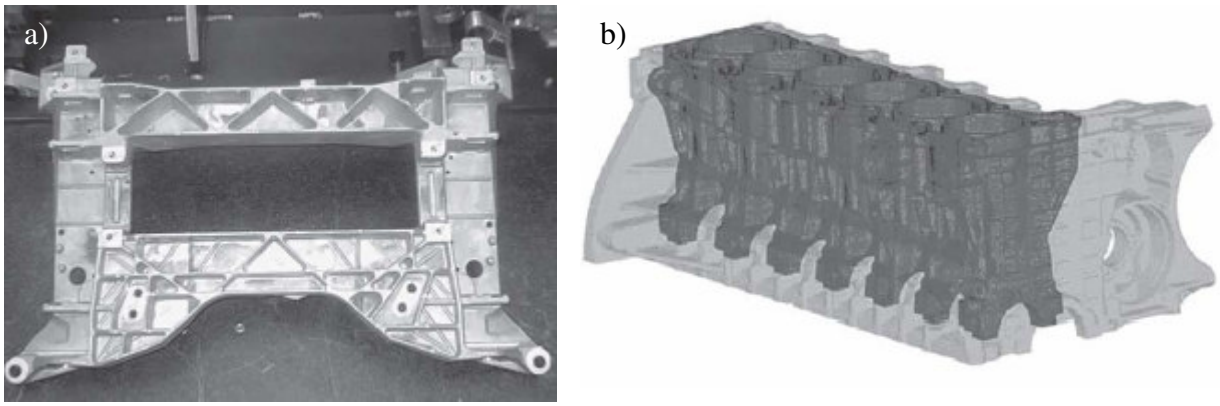


Figure 2.5: Commercially creep resistant magnesium alloys: a) AE44 used in engine cradle of a Corvette [Beals *et al.* 2007] b) AJ62 alloy shown in the schematic figure of a composite BMW engine (darker region represents Al inserts).

Development of magnesium alloys to be used as implants is currently one of the forefronts in magnesium research. Magnesium is considered to be biocompatible and ($Mg^{2+}$) is an important ion in the human body, i.e. the fourth most abundant cation in the human body, making magnesium potentially a promising candidate for biomedical applications [Witte *et al.* 2006]. Studies show magnesium has a constructive role in bone formation [Witte *et al.* 2006].

## 2.3 Mg-Ca-Zn Alloys

In this section magnesium alloy development based on calcium and zinc will be reviewed. Phase diagrams as well as microstructural characteristics will be brought forward.

#### 2.3.1.1 Ca and Zinc in Mg alloy development

Recently calcium has gained much interest as an alloying element in developing creep resistant magnesium alloys for power train applications [Hu *et al.* 2003]. Calcium is an inexpensive alloying element compared to rare earth elements, it has low density (1.55 $g/cm^3$), and the Mg-Ca system shows potential for precipitation hardening [Nie and Muddle 1997]. Meanwhile, calcium improves oxidation resistance of magnesium at temperatures above 480° C [You 2000]. Researchers have also shown that adding calcium increases the ignition temperature of magnesium, Fig 2.6, which is beneficial not only in melting processes [Polmear 2006] but also for potential auto and aerospace applications regarding the safety issues [Watari 2006]. As Fig 2.6 shows, calcium bearing magnesium alloy shows no sign of extensive combustion compared to the non-calcium bearing magnesium alloy. Pros and cons of adding calcium to magnesium as a major alloying element compared to aluminum are presented in Fig 2.7.

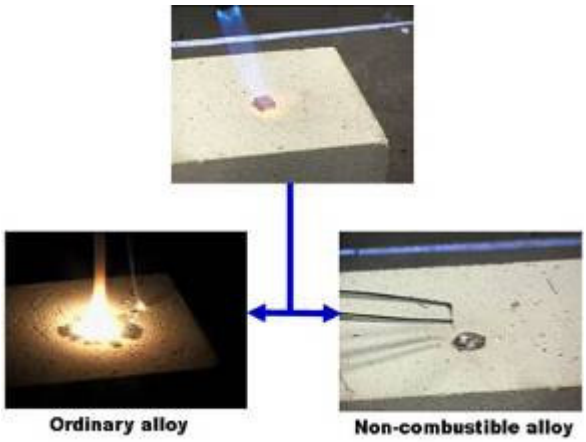


Figure 2.6: Non-combustible Ca bearing magnesium alloy [AIST 2007].

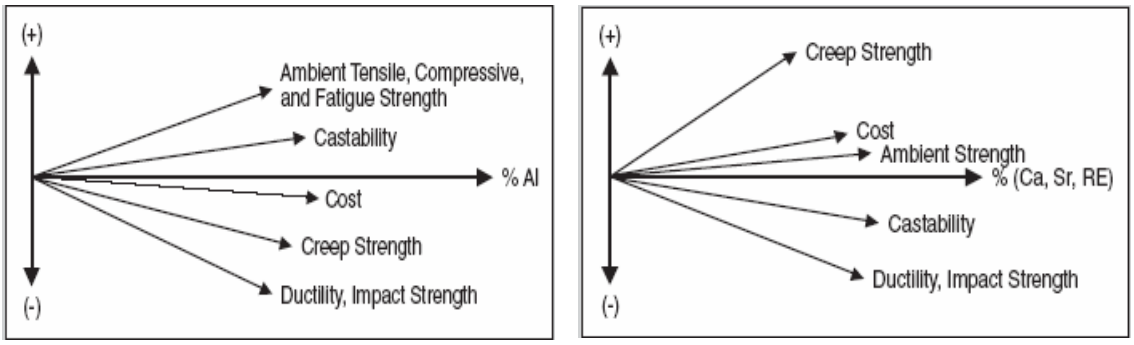


Figure 2.7: Effects of alloying elements on magnesium alloys (Al and Ca) [Aghion 2003].

Second major alloying element to be reviewed here is zinc. Zinc has high solid solubility in magnesium, i.e. up to 6.2 wt% which reduces to 2 wt. % at room temperature [Hashemi and Clark 1988]. This results in solid solution strengthening in zinc containing magnesium alloys. Zinc also promotes age hardening response of the magnesium alloys [Polmear 2006, Mendis *et al.* 2006] and increases fracture toughness of wrought magnesium alloys [Somekawa *et al.* 2006].

#### 2.3.1.2 Phase Diagrams

In this section, phase diagrams of Mg-Ca and Mg-Zn will be briefly reviewed and characteristics of these systems will be discussed. Binary phase diagram of Mg-Ca (Fig 2.8) shows solubility of Ca in magnesium matrix as 1.34 wt% at 515.5°C which declines to almost zero close to 200°C.

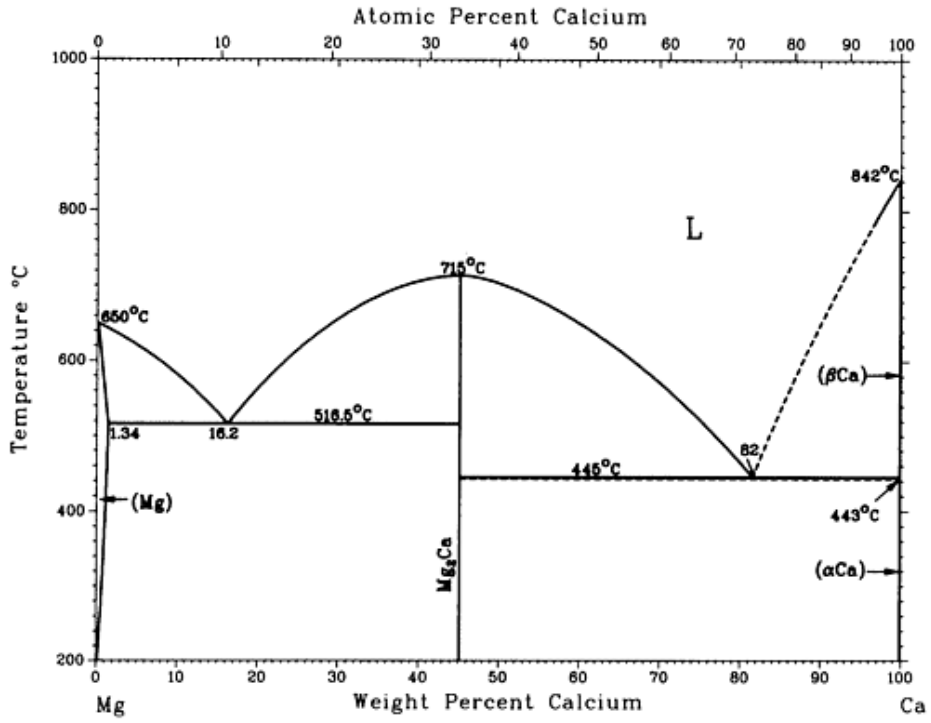


Figure 2.8: Mg-Ca binary phase diagram [Hashemi and Clark 1988].

Another important feature of Mg-Ca system is the presence of $Mg_2Ca$, the Laves phase which has a high melting point of 715°C. Laves phases have specific characteristics as close

packed intermetallic compounds with metallic behavior. Laves phases are formed if two conditions are met [Westbrook 1967]:

I. Electrochemical nature of the components must be similar.

II. The ratio between atomic radii of components must fall between 1 and 1.2.

Table 2-2 summarizes crystal structure and electronic configuration of Mg, Ca and Zn. All of those three elements have the same electronic configuration, i.e. $s^2$ configuration, and the atomic size ratios are 1.23 and 1.15 for Ca/Mg and Mg/Zn, respectively.

Table 2.2: Crystal structure and electronic properties of Mg, Ca and Zn [Hassen 1996].

| Element | Z | Crystal Structure | r(M) (A°) | $a_0$ (A) | $c_0$ (A) | $c_0/a_0$ | Electronic Configuration |
|---|---|---|---|---|---|---|---|
| Mg | 12 | HCP | 1.77 | 3.20927 | 5.21033 | 1.623 | [Ne] $3s^2$ |
| Ca | 20 | FCC | 2.184 | 5.576 | NA | NA | [Ar] $4s^2$ |
| Zn | 30 | HCP | 1.537 | 2.6648 | 4.9467 | 1.856 | [Ar] $3d^{10}$, $4s^2$ |

$Mg_2Ca$ has hexagonal structure [Westbrook 1967], i.e. the same hexagonal crystal structure as of magnesium. This phase can form in dilute Mg-Ca alloys due to the sharp decline in solubility of Ca in magnesium matrix, which is also the requirement for the alloy to undergo age hardening heat treatment [Martin 1980]. Developing age-hardenable Mg-Ca alloys have previously been studied [Nie and Muddle 1997].

Binary Mg-Zn phase diagram, Fig 2.9 shows high solubility of zinc, i.e. up to 6.2 wt% at 340°C. Several intermetallic compounds are seen in this phase diagram. Precipitation of rods of coherent $MgZn_2$ is known to render the maximum hardness in Mg-Zn alloys [Polmear 2006].

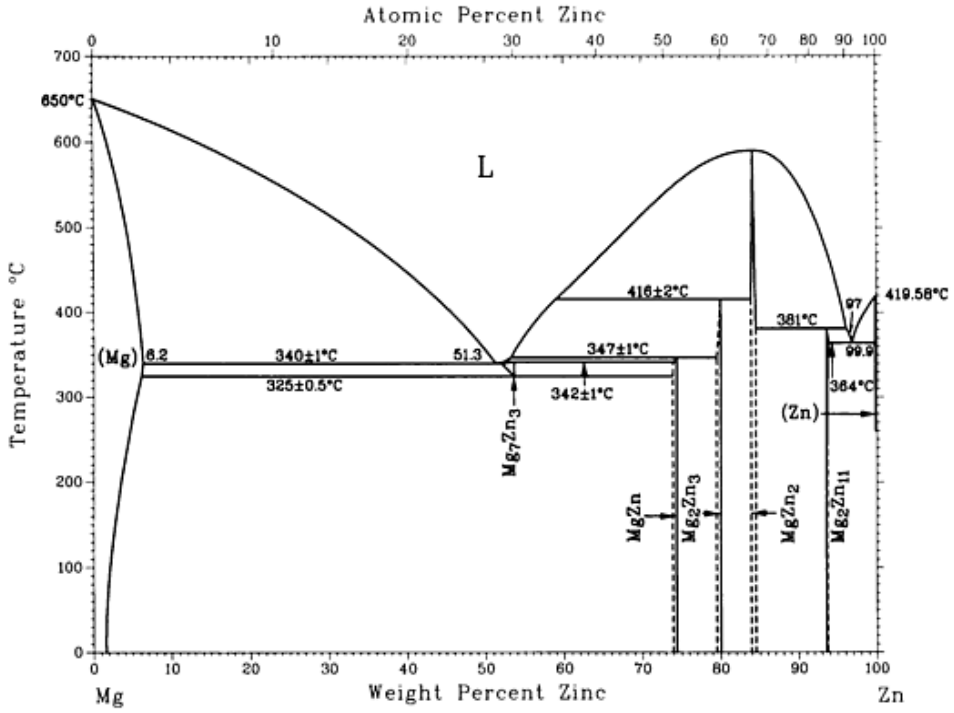


Figure 2.9: Mg-Zn binary phase diagram [Hashemi and Clark 1988].

#### 2.3.1.3 Microstructural Characteristics

As-cast microstructure of binary Mg-Ca alloys is comprised of primary α-Mg and eutectic colonies of α-Mg + $Mg_2Ca$ [Nie and Muddle 1997] which is in agreement with the phase diagram of the binary Mg-Ca system, Fig 2.8. It should be noted that, however, there are not extensive studies on the microstructural evolution of the binary Mg-Ca system in the literature. As-cast microstructure of dilute Mg-Ca-Zn alloys shows dendritic solidification of primary α-Mg dendrites followed by solidification of $Mg_2Ca$ particles [Zhong 2005]. Solidification is terminated by eutectic reactions in final pockets of eutectic within dendrites [Levi *et al.* 2006], Fig 2.10.

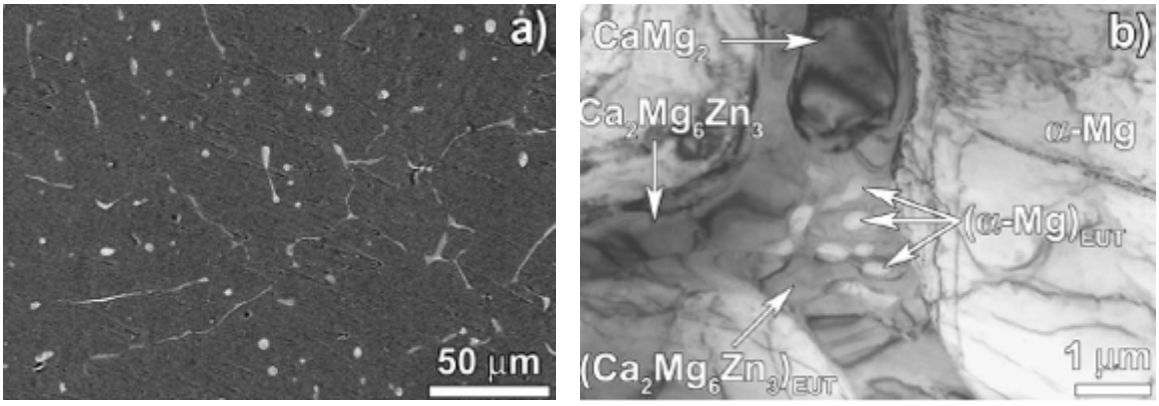


Figure 2.10: SEM image of as-cast microstructure of Mg-1.6 wt. %Ca-3.2 wt. %Zn alloy (a) and TEM bright field of a triple junction (b) [Levi *et al.* 2006].

## 2.4 Homogenization of As-Cast Structures

Microstructure of as-cast alloys often shows segregation of the alloying elements, resulting in non-uniform distribution of solute in the microstructure. This phenomenon, also known as coring, has an important implication in precipitation hardening alloys where according to the phase diagram final solidification of a single phase is expected, however in practice a large number of solute atoms segregate to grain boundaries during solidification [Reed-Hill and Abbaschian 1991]. For precipitation hardening thus it is needed that solute atoms are homogenously distributed through the matrix which is achieved by the homogenization heat treatment [Porter and Easterling 1992]. To express kinetics of homogenization, the simplest composition model that can be solved is if solute concentration $C_B$, varies sinusoidally with distance in one dimension as shown in Fig.2.11 [Porter and Easterling 1992, Reed-Hill and Abbaschian 1991 and Hosford 2007].

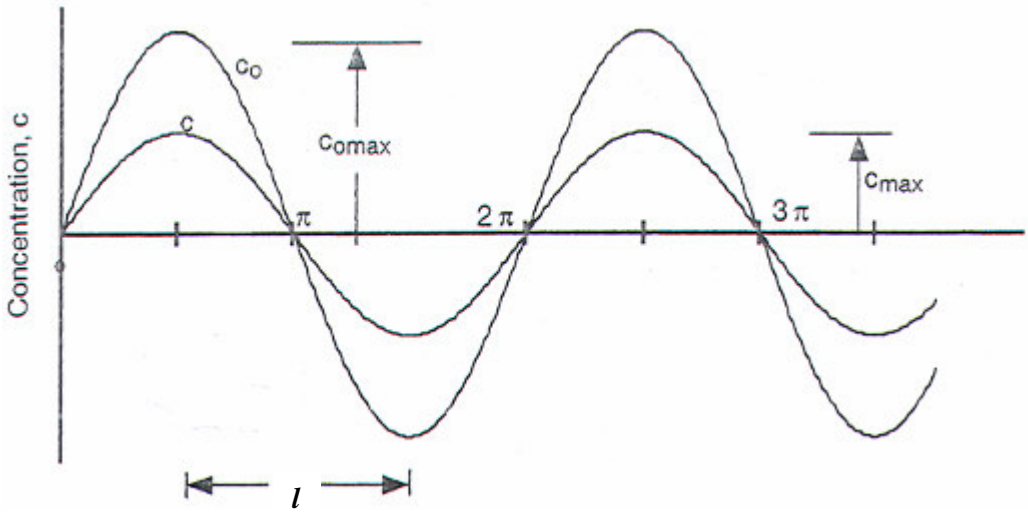


Figure 2.11: Sinusoidal concentration profile, $c_0$, resulting from interdendritic segregation, and final concentration profile, c, after homogenization [Hosford 2007].

In this simple model, at time $t = 0$ the concentration profile, C, is given by [Porter and Easterling 1992]:

$$C = \overline{C} + \beta_0 \sin \frac{\pi \times x}{l} \tag{2.1}$$

Where $x$ is distance, $l$ is one-half the dendrite arm spacing, $\overline{C}$ is the mean composition and $\beta_0$ is the concentration gradient amplitude. Assuming independence of diffusion coefficient of solute, $D_B$, and initial condition of (2.1), solution to the Fick's second law of diffusion, i.e. $\frac{\partial C_B}{\partial t} = D_B \frac{\partial^2 C_B}{\partial x^2}$, is [Porter and Easterling 1992, Glicksman 2000]:

$$C = \overline{C} + \beta_0 \sin \left(\frac{\pi \times x}{l}\right) \exp \left(\frac{-t}{\tau}\right) \tag{2.2}$$

$\tau$ is a constant called relaxation time and is given by [Reed-Hill and Abbaschian 1991, Porter and Easterling 1992]:

$$\tau = \frac{l^2}{\pi^2 D} \tag{2.3}$$

where D is a diffusion coefficient. When $t = \tau$, concentration gradient amplitude reduces to $\frac{\beta_0}{\tau}$ [Porter and Easterling 1992]. In practice, concentration gradients are different at different spots of the sample. Therefore, each region has its relaxation time and final relaxation time will be determined by the longest concentration wavelength [Porter and Easterling 1992].

Another important aspect of homogenization is dissolution of the second phase particles and diffusion of solute in the matrix. Dissolution kinetics will be discussed in more detail in section 2.5.5.3.

## 2.5 Precipitation Hardening

In this section, precipitation hardening mechanisms and precipitation kinetics will be briefly reviewed. A short historical review of this important strengthening mechanism is given followed by different hardening mechanisms due to the interaction between dislocations and precipitates. Precipitation kinetics will wrap up this section.

### 2.5.1 General Considerations

Precipitation hardening, or age hardening, was first discovered by Alfred Wilm in Germany in 1906. He attempted to harden Al-2 at% Cu by quenching the alloy in a similar manner to steel; and found yield strength increased with time at room temperature. The results were published in 1911 without explanation [Peckner 1964]. In 1937, for the first time Guinier and Preston by careful X-ray diffraction work in Al-Cu alloys solved this mystery. Diffuse scattering occurred outside but associated with the Brag reflections of the solid solution which were deduced to be due to solute-enriched regions in the solid solution [Peckner 1964].

Precipitation hardening involves precipitation of a second phase, which differs from the matrix in its composition or degree of order [Hassen 1996]. These precipitates hinder dislocations motion, resulting in the increase of the flow stress.

### 2.5.2 Hardening due to Solutes and Precipitates

Solute atoms increase the yield strength of crystalline materials by interacting with long range stress field of dislocations. Meanwhile, due to the size difference between solute atoms and solvent atoms of the matrix, stress field around solute atoms interact with that of the matrix, giving rise to the interaction energy between dislocation and solute atom [Courtney 2000].

It is often useful to introduce the soft and hard obstacle concept, phenomenological terms used to describe the interaction between the moving dislocation and an obstacle [Nembach 1997, Esmaeili 2002]. Fig2.12 shows a dislocation encountering an array of obstacles. The

angle φ is the measure of the obstacle strength. While weak obstacles are overcome with very small bending, (φ ~π), strong obstacle makes dislocation double back on itself (φ ~0°) [Kelly and Nicholson 1971].


Figure 2.12: Dislocation held up by a random array of obstacles in slip plane, (a) φ is small, strong obstacles while in case of weak obstacles in (b) dislocation is nearly straight (φ ≅ π) [Courtney 2000].

Solid solution strengthening can be discussed by the obstacle concept. If $L'$ is the effective obstacle spacing, and $b$ burgers vector of a dislocation, the increase in flow stress associated with the solute atom is [Courtney 2000]:

$$\tau = \frac{F_{\max}}{b \times L'} \tag{2.4}$$

Solute atoms can be considered as soft obstacles [Kelly and Nicholson, 1971], and $F_{\max}$ is on the order of $\frac{\mu b^2}{120}$ [Courtney, 2000], where $\mu$ is the shear modulus of the matrix. $L'$ is given as $\frac{b}{\sqrt{2c \times (\pi - \varphi)}}$, where $c$ is the solute concentration and $\varphi$ is the breaking angle;

$(\pi-\varphi)$ is very small , close to 1° [Courtney 2000]. Increase in yield strength correlates with concentration as $c^n$ where $n$ is between 0.3 and 0.5, i.e. ($\Delta\tau_y \propto \sqrt{c}$ ) [Courtney 2000].

### 2.5.3 Precipitation Hardening Mechanisms

In this section dislocation-obstacle interaction in age-hardened alloys will be reviewed in more detail. Two major types of interaction between dislocations and obstacles are particle shearing and looping mechanism around precipitates (Orowan looping) [Nembach 1997]. If precipitates are deformable, the intrinsic properties of the precipitates are more influential than precipitates size [Kelly and Nicholson 1971]. A moving dislocation on slip plane will choose the most energetically favorable mechanism to pass the field of obstacles [Peckner 1964].

#### 2.5.3.1 Deforming Particles

At the early stages of age hardening, the precipitates are small and coherent or semi coherent.

##### 2.5.3.1.1 Coherency Hardening

Formation of coherent interfaces increases free energy of the system by account of elastic strain fields around the coherent interface ($\Delta G_s$), Fig 2.13.

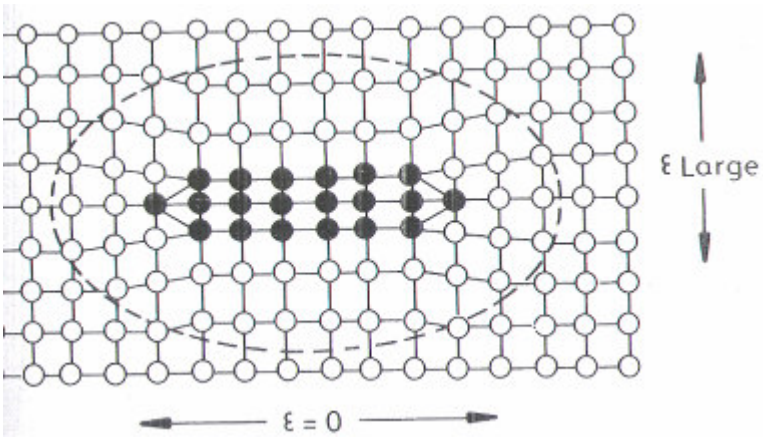


Figure 2.13: Development of coherency strains around disk-shaped precipitate [Porter and Easterling 1992].

Elastic strain energy ($\Delta G_s$) associated with unconstrained misfit, i.e. $\delta = \frac{a_p - a_m}{a_m}$, where $a_p$ and $a_m$ represent lattice parameters of precipitate and matrix respectively, can be formulated as [Porter and Easterling 1992]:

$$\Delta G_s \cong 4\mu\delta^2 \times V \tag{2.5}$$

where $\mu$ is the shear modulus of the matrix and V is the volume of unconstrained hole in the matrix. The increase in resolved shear stress as a result of coherent precipitates can also be expressed as a function of volume fraction of precipitates ($f$), coherency strain ($\varepsilon_{coh} = \frac{2}{3}\delta$), $\mu$, burgers vector and precipitate radius ($r$) by the following relation [Courtney 2000]:

$$\tau_{coh} \cong 7\left|\varepsilon_{coh}\right|^{\frac{2}{3}} \times \mu \times \sqrt{\frac{fr}{b}} \tag{2.6}$$

#### 2.5.3.1.2 Modulus Hardening

When dislocation enters a precipitate with shear modulus different than the matrix, $G_p$, the dislocation line tension which can be approximated as $\frac{Gb^2}{2}$ where G is the shear modulus of the matrix, alters [Courtney 2000]. This is shown schematically in Fig 2.14. Therefore if the shear modulus of the precipitate, $G_{p,}$ is larger than that of the matrix, $G_m$, a larger stress is required in order for the dislocation to move through the precipitate [Peckner 1964].

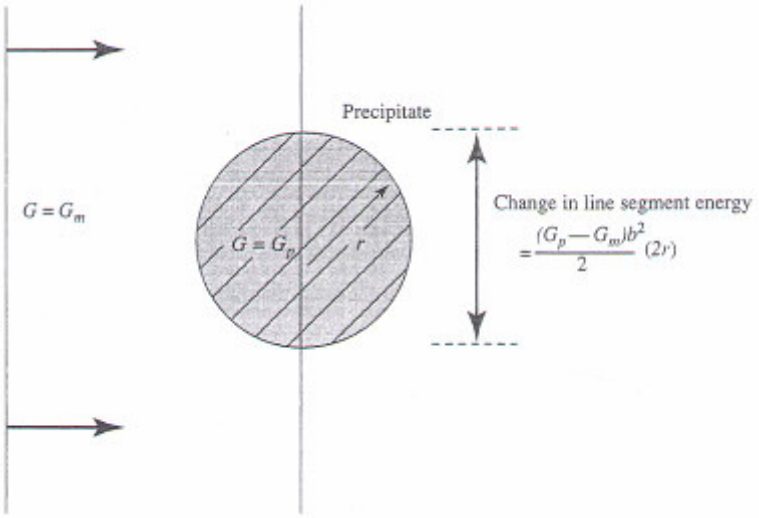


Figure 2.14: Dislocation entering a precipitate with radius r and shear modulus of Gp [Courtney 2000].

#### 2.5.3.1.3 Chemical Strengthening

Chemical strengthening arises from additional surface formed during cutting of a particle by a dislocation [Peckner 1964]. Formation of additional precipitate-matrix interface will increase free energy and work must be done by a dislocation [Courtney 2000]. This process schematically is shown in Figure 2.15.

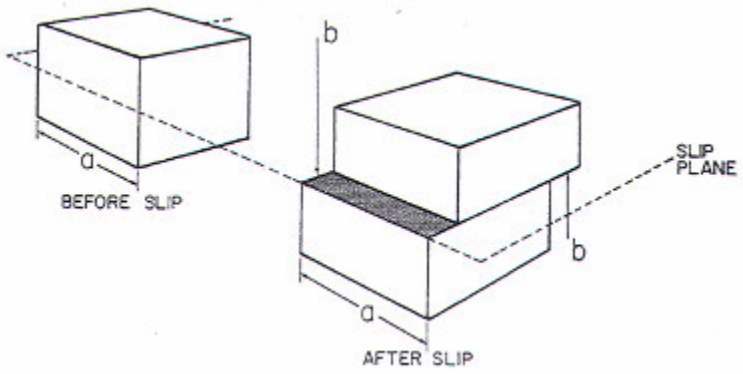


Figure 2.15: Shearing of a cube by plastic deformation and formation of additional surface [Peckner 1967].

After passage of dislocation with burgers vector, $b$, area ($2ab$) is formed; the energy spent for this process is ($2ab\Delta F_s$), where $\Delta F_s$ is the surface free energy per unit area of the surface.

To formulate chemical strengthening, precipitates with radius r, are cut by a dislocation and total increase in energy will be [Courtney 2000]:

$$\Delta G = 2\pi r \gamma_s b \tag{2.8}$$

where $\gamma_s$ is the particle-matrix interphase surface energy. Since the $F_{max}$ can be approximated as $\frac{dG}{dx}$, by recalling (2.4) shear stress required to push the dislocation through the particle will be [Peckner 1964]:

$$\tau_{chem} \cong \frac{\pi \times f \times \gamma_s}{2b} \tag{2.9}$$

2.5.3.1.4 Order Strengthening

If an ordered precipitate is cut by dislocation, Fig 2.16, an antiphase boundary of energy $E_{APB}$ is produced which represents a higher energy state [Hassen 1996].

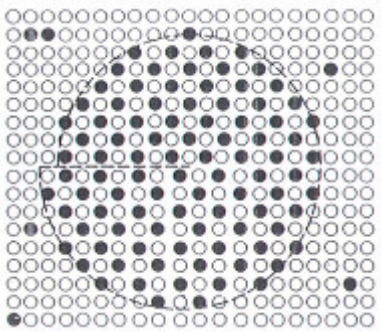

Figure 2.16: An ordered Ni3Al precipitate is cut by a dislocation in the Ni matrix (o)and Al (•)[Hassen 1996].

The problem can be treated as chemical strengthening and the increased shear strength can be postulated as:

$$\tau = \frac{\pi(ABPE)f}{2b} \tag{2.10}$$

where APBE is energy associated with formation of antiphase boundary.

At the early stages of precipitation and when APBE is low (e.g. when dislocations are widely separated), $\tau$ can be treated as [Courtney 2000]:

$$\tau_{ord} = 0.7G(\varepsilon_{ord})^{\frac{3}{2}}(\frac{fr}{b})^{\frac{1}{2}} \tag{2.11}$$

#### 2.5.3.2 Non-Deformable Particles, Orowan Looping

Orowan mechanism explains the hardening effect of precipitates when they have grown to the size that are no longer coherent with the matrix and therefore not shearable [Reed-Hill and Abbaschian, 1991]. Strengthening arises from the fact that the dislocations must bow out between two neighboring particles which is opposed by the line tension of dislocations. [Nembach 1997]. If the mean spacing between particles is L, the increase in shear strength associated with dislocation bowing in the matrix with shear modulus of $\mu$ is determined as [Courtney 2000, Gladman 1999]:

$$\tau_B = \frac{\mu b}{(L-2r)} \tag{2.12}$$

Orowan mechanism is schematically shown in Fig 2.17.

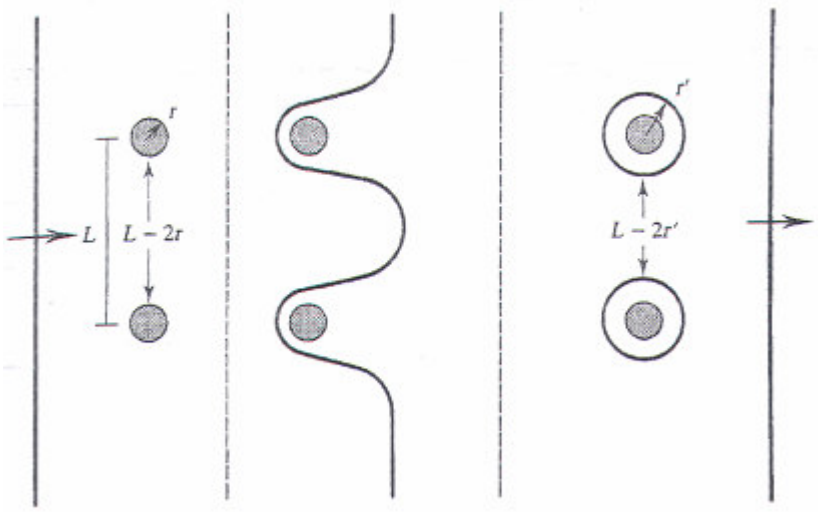


Figure 2.17: Dislocation bows out between non-deforming particles following by bypassing of obstacles; subsequent dislocation should pass smaller spacing and τB will increase [Courtny 2000].

A more detailed treatment of the Orowan mechanism in magnesium alloys will be given in section 2.6.3.

### 2.5.4 Superposition of Hardening Mechanisms

If there are distinct types of obstacles in the glide plane, hardening can be postulated as general form of [Nembach 1996]:

$$\tau_t^{\,k} = \tau_1^k + \tau_2^k \tag{2.13}$$

The exponent *k* lies between one and two. Linear Law, i.e. k=1, is used when both types of precipitates are sheared by dislocations, or there are few hard obstacles mixed in with many soft obstacles [Nembach 1996, Esmaeili 2002]. Pythagorean law applies if both types of obstacles are of the same strength [Nembach 1996].In the case of superimposing solid

solution hardening contributions of the matrix and hardening as a result of precipitates, linear law is applied [Ardell 1985].

### 2.5.5 Precipitation Kinetics

This section reviews the application of isothermal calorimetry as well as models to describe the kinetics of precipitation.

#### 2.5.5.1 Application of Isothermal Calorimetry in Determining Precipitation Kinetics

Isothermal calorimetry technique has recently been used to analyze the precipitation kinetics of aluminum alloys [Esmaeili *et al.* 2003 a and b, Esmaeili and Lloyd 2005 a, Poetter 2006, Sepehrband and Esmaeili 2008, Cluff and Esmaeili 2008]. According to the introduced methodology, the relative volume fraction of precipitates, $f_r$, after time t can be estimated as:

$$f_r = \frac{\int_0^t \frac{dQ}{dt} dt}{\int_0^{t_f} \frac{dQ}{dt} dt} \tag{2.14}$$

where, in general, $\int_0^t \frac{dQ}{dt} dt$ is the area under the IC trace up to the aging time t and $\int_0^t \frac{dQ}{dt} dt$ is the total amount of heat evolved as a result of precipitation up to the characteristic time $t_f$ when heat flow becomes too small to be measured. Application of IC technique in estimating relative volume fraction of precipitates is shown in Fig 2.18.

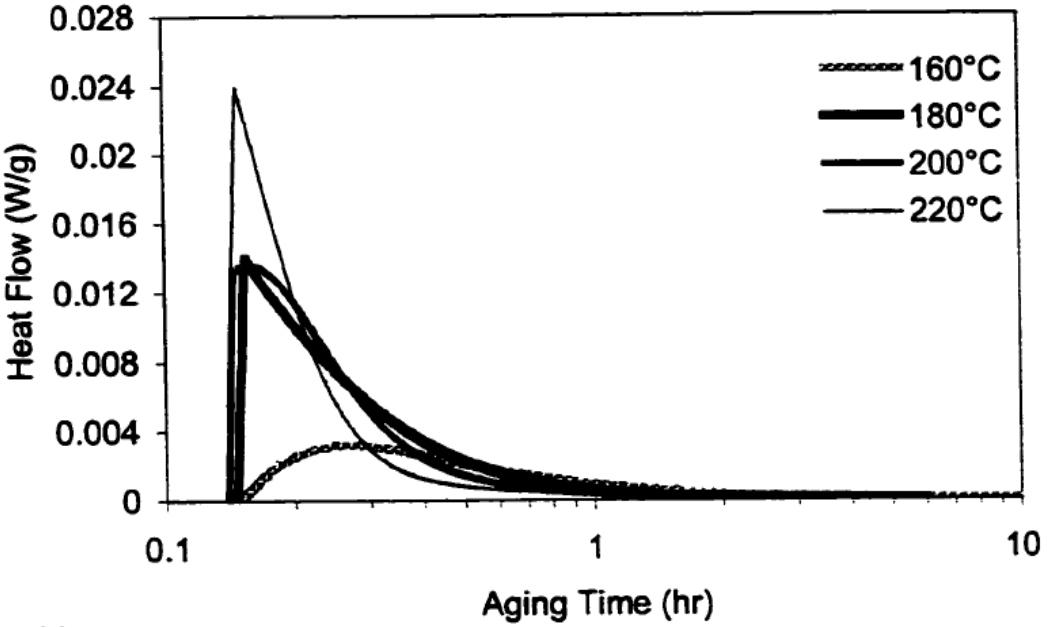


(a)

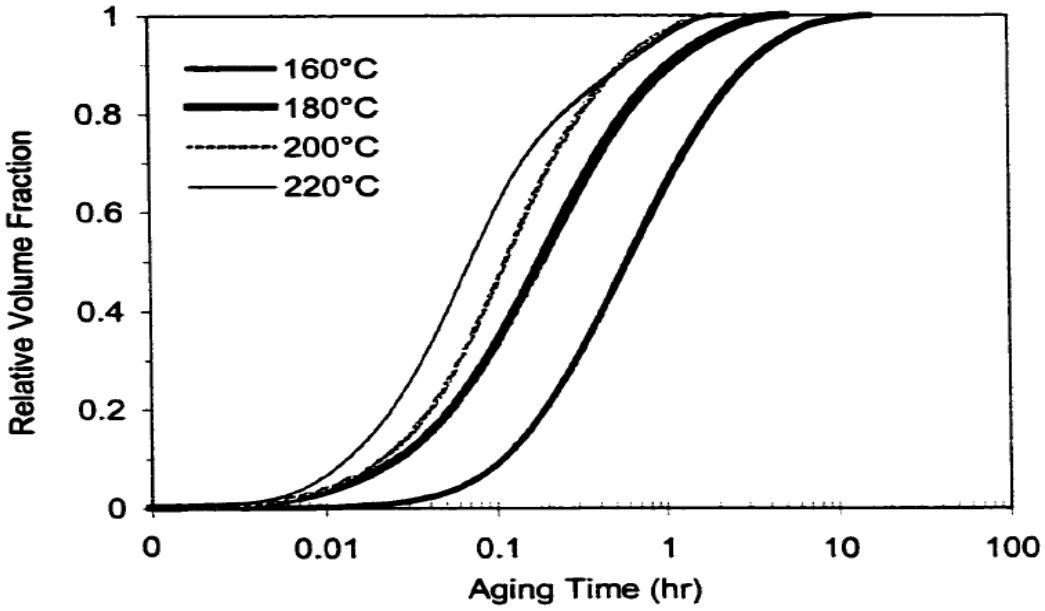


(b)

Figure 2.18: Isothermal calorimetry traces for the as-quenched AA6111 over the temperature range of 160°C-220°C (a) and the estimated relative volume fraction of precipitates from the traces (b) [Esmaeili 2002].

#### 2.5.5.2 Modeling of Precipitation Kinetics

Precipitation transformation in this work is considered as nucleation and growth type transformations. In these type of transformations, the volume fraction of transformed solid solution may be expressed by Johnson-Mehl, Avrami and Kolmogorov (JMAK) kinetics [Avrami 1939, Porter and Easterling 1992]:

$$f_{rppt} = 1 - \exp(-kt^n) \tag{2.15}$$

where t is time and n is a temperature independent numerical exponent that can vary from 1 to 4 [Porter and Easterling 1992]. On the other hand, k includes nucleation and growth rates and strongly depends on temperature [Porter and Easterling 1992]. Accordingly, the overall transformation kinetics after time t at an isothermal aging temperature T can be expressed as a function of both t and T, i.e. *f(t,T)*. The use of JMAK model on describing the kinetics of precipitation in AA6111 aluminum alloy [Esmaeili *et al.* 2003a] is demonstrated in Figure 2.19. It should be added that the experimental data in Fig 2.19 is the same as the data presented in Figure 2.18.b.

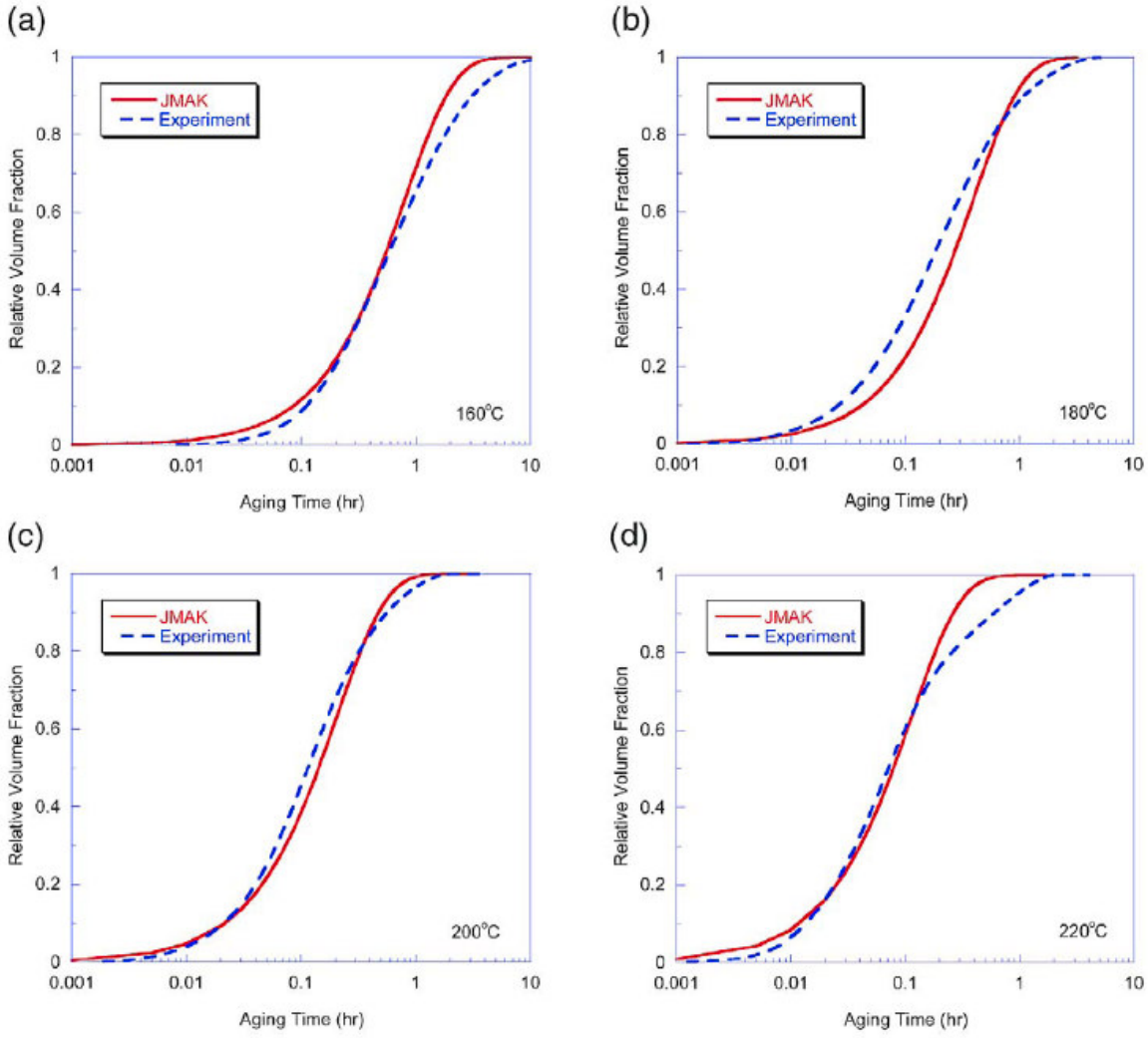


Figure 2.19: Comparison of relative volume fractions obtained using the JMAK model with the values obtained directly from the isothermal calorimetry data, 160°C (a), 180°C (b), 200°C (c) and 220°C [Esmaeili *et al.* 2003 a].

## 2.6 Precipitation Hardening in Mg Alloys

### 2.6.1 General Considerations

The phase diagrams of most magnesium alloy systems display the profile required for precipitation hardening, i.e. a decrease in solid solubility with temperature [Polmear 2006].

Age hardening responses in commercial magnesium alloys, however, are significantly less than the response observed in some aluminum alloys [Polmear 2006]. A summary of precipitation processes in magnesium alloys is given in Table 2.3.

Table 2.3: Possible precipitation processes in some magnesium alloys.

| Alloy System | Precipitation Process | Reference |
|---|---|---|
| Mg-Al | SSS $\rightarrow Mg_{17}Al_{12}$ | [Hort *et al.* 2006] |
| Mg-Zn(-Cu) | SSS $\rightarrow$ GP zones $\rightarrow$ $MgZn_2$ (rods, coherent) $\rightarrow$ $MgZn_2$ (discs, semicoherent) $\rightarrow$ $Mg_2Zn_3$ (trigonal, incoherent) | [Hort *et al.* 2006] |
| Mg-RE(Nd) | SSS $\rightarrow$ GP zones $\rightarrow$ $Mg_3Nd$ (NA, hcp) $\rightarrow$ $Mg_3Nd$ (fcc, semicoherent) $\rightarrow$ $Mg_{12}Nd$ (incoherent) | [Hort *et al.* 2006] |
| Mg-Sn | SSS $\rightarrow$ $Mg_2Sn$ | [Mendis *et al.* 2006] |
| Mg-Ca-Zn | SSS $\rightarrow$ $Ca_2Mg_6Zn_3$ (trigonal)<br>SSS $\rightarrow$ GP zones $\rightarrow$ $Mg_2Ca$(-Zn) | [Levi *et al.* 2006]<br>[Oh *et al*. 2005] |

### 2.6.2 Continuous and Discontinuous Precipitation

Continuous precipitation involves two successive processes, nucleation and growth. In precipitation reaction of the $\beta$ from supersaturated matrix $\alpha$, first, nuclei of the β form, homogeneously or heterogeneously, and subsequently these nuclei grow. Precipitation mainly occurs intragranularly [Papon *et al.* 2006]. Fig 2.20 schematically shows the continuous precipitation sequence.

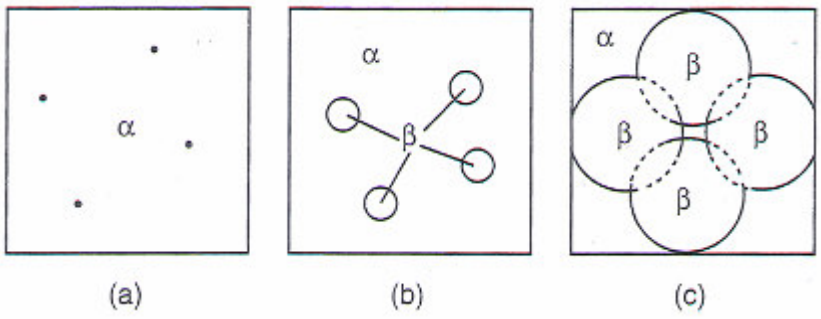


Figure 2.20: Continuous precipitation, (a) initial rapid nucleation of the phase β within initial phase α, (b) growth of phase β nuclei, (c) impingement of β phase fields [Papon 2006].

On the other hand, in discontinuous precipitation, precipitates mainly form within moving grain boundaries [Clark 1968]. Precipitation therefore is at the grain boundaries and the grain boundary moves with the growing tips of the precipitates [Porter and Easterling 1992]. Both continuous and discontinuous precipitation have been reported in Mg alloys [Clark 1968 and Celloto 2000]. Continuous precipitation of $Al_2Ca$ in Mg-Al-Ca alloys [Suzuki *et al*. 2007], $Mg_2Sn$ in Mg-Sn alloys [Mendis *et al.* 2006] $Mg_{17}Al_{12}$ in an Mg-Al-Zn alloy [Celloto 2000], and $MgZn_2$ in Mg-Zn alloys [Polmear 2006] have been reported in the literature. An example of discontinuous precipitation is the precipitation of β-$Mg_{17}Al_{12}$ at the grain boundaries in Mg-Al alloys, Fig.2.21 [Porter and Easterling 1992, Clark 1968]. As Celloto [2000] cites, both continuous and discontinuous precipitation of β-$Mg_{17}Al_{12}$ is seen in Mg-Al alloys.

Continuous or general precipitation leads to the finely distributed precipitates that are associated with good mechanical properties while discontinuous precipitation results in formation of coarse equilibrium phases at the grain boundaries [Porter and Easterling 1992].

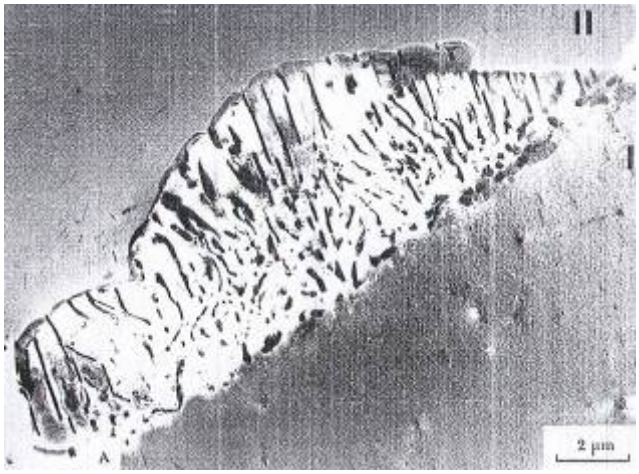


Figure 2.21: Discontinuous precipitation of $Mg_{17}Al_{12}$ in an Mg-9 at. %Al solution treated and aged for 1 hour at 220° C followed by 2 min at 310° C [Porter and Easterling 1992].

### 2.6.3 Effects of Precipitates Shape and Orientation on Precipitation Hardening Response of Mg Alloys

Shape, orientation and distribution of precipitates have long been recognized as important factors in determining the strength of alloys. The strengthening produced by the interaction of dislocations with a dispersion of incoherent, non-shearable particles is expressed by the Orowan mechanism [Knipling *et al.* 2006]. The increment in shear strength can be expressed as [Nie 2003]:

$$\Delta\tau = \frac{Gb}{2\pi\lambda\sqrt{1-\upsilon}}\ln\frac{d_p}{r_0} \tag{2.17}$$

where $\Delta\tau$ is the increment in shear strength , G is the shear modulus of the magnesium matrix, b is the burgers vector, $\lambda$ is the effective planar inter obstacle spacing while $d_p$ is the

mean planar diameter of the point obstacle and $r_0$ the core radius of dislocations ($\cong$b) [Nie 2003].

As equation (2.17) shows, $\Delta\tau$ is dependent on $\lambda$ which is a function of precipitate shape and orientation in the magnesium matrix. Table 2-4 summarizes the effective planar inter obstacle spacing for different precipitate shape and orientation where $f$, $d_t$ and $t_t$ are volume fraction of precipitates, precipitate diameter and precipitate thickness, respectively. It should be noted that by assuming that the volume fraction of each group of precipitates remains constant, change in precipitate shape from sphere to plate or rod will alter the number density of precipitates.

Table 2.4: Effect of precipitates arrangement on the effective inter-particle spacing [Nie 2003].

| Array of Obstacles | λ |
|---|---|
| Spherical Precipitates | $\left(\frac{0.779}{\sqrt{f}} - 0.785\right) d_t$ |
| Prismatic Plates $\left\{10\bar{1}0\right\}_\alpha$ or $\left\{2\bar{1}\bar{1}0\right\}_\alpha$ 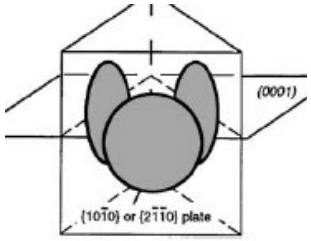  | $0.825\sqrt{\frac{d_t t_t}{f}} - 0.393 d_t - 0.866 t_t$ |
| Basal Plates 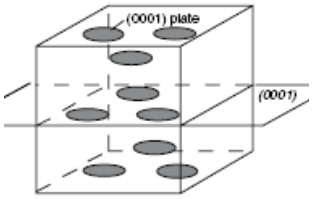  | $\left(\frac{0.953}{\sqrt{f}} - 1\right) d_t$ |
| [0001] Precipitate Rods $\left(l_t >> d_t\right)$ 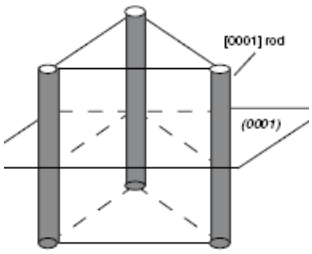  | $\left(\frac{0.953}{\sqrt{f}} - 1\right) d_t$ |

The relationship between effective inter-particle spacing, λ, with precipitate number density, is shown in Fig 2.22, showing the most effective precipitates in lowering λ and increasing the critical resolved shear stress of magnesium alloys are the prismatic plates.

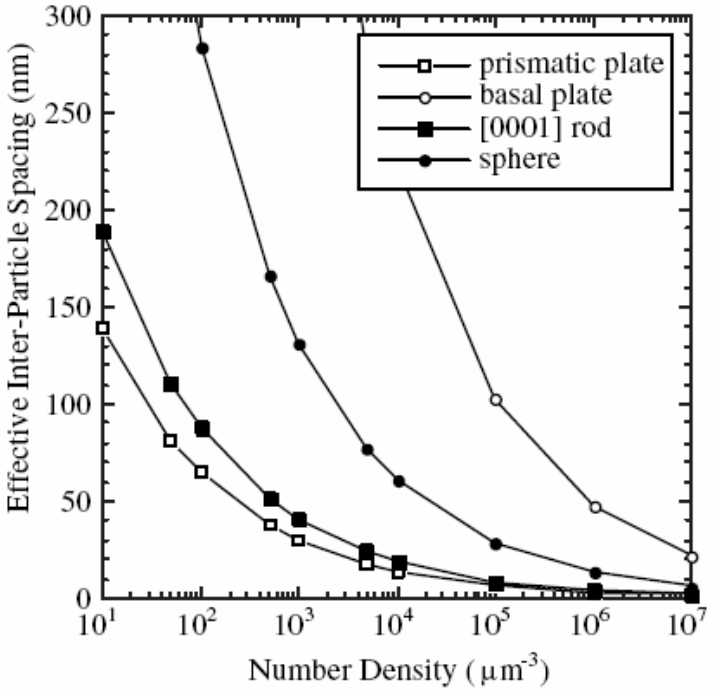


Figure 2.22: Variation of effective inter-particle spacing with number density of precipitates per volume in the magnesium matrix at a precipitate volume fraction of 0.04 [Nie 2003].

### 2.6.4 Precipitation Hardening in Dilute Magnesium Alloy Systems

#### 2.6.4.1 General Considerations

In this section, a summary of the precipitation-hardening behavior of heat-treatable magnesium alloys will be presented. Precipitation hardening of the mainstream AZ (Mg-Al-Zn) alloys, e.g. AZ91, has been investigated [Cellotto 2000 and Hutchinson *et al.* 2005]. The formation of equilibrium $Mg_{17}Al_{12}$ precipitates has been reported in both Mg-Al-Zn and Mg-Al systems [Hutchinson *et al.* 2005, Clark 1968]. The contribution to the hardness from dislocations-precipitates interaction is relatively small, compared to what is typically seen in precipitation hardened aluminum alloys, since precipitates are not effective in hindering basal slip [Hutchinson *et al.* 2005]. Another classic precipitation-hardenable system is the Mg-Zn system in the composition range of the 3-8 wt% zinc [Clark 1965]. Clark [1965] concludes that the hardening phase is the rod shaped transitional MgZn' phase with the crystal structure of the Laves phase $MgZn_2$. Age hardening responses of AZ91 and Mg-5 wt% Zn alloys are shown in Fig 2.23.

Precipitation hardening in a number of novel magnesium alloys has also been studied [e.g. Suzuki et al. 2007, Weiss *et al.* 2002]. Suzuki *et al.* [2007] have investigated precipitation hardening in the Ca-containing AXJ530 alloy and reported the precipitation of finely-dispersed $Al_2Ca$ phase during isothermal aging treatment. Age hardening response in AXJ530 has been shown in Figure 2.24. Suzuki *et al.* [2007] have also reported the morphology of $Al_2Ca$ precipitate and its orientation relationship with the matrix, as well as the TTT diagram for the formation of this precipitate.

To wrap up this chapter, a survey on age hardening response of the dilute Mg-Ca-Zn system will be presented.

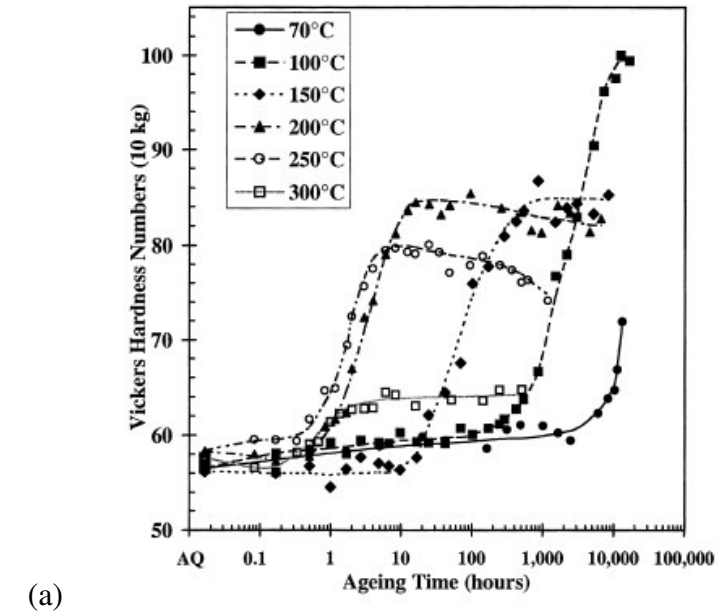


(a)

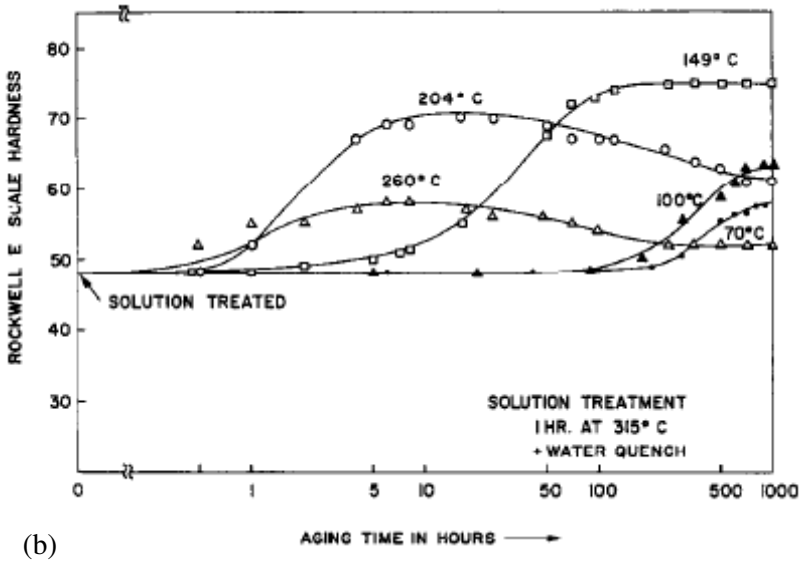


(b)

Figure 2.23: Age hardening curves for AZ91 in the temperature range of 70°C-300°C (a) [Cellotto 2000] and for Mg-5 wt% Zn in the temperature range of 70°C-260°C (b) [Clark 1965].

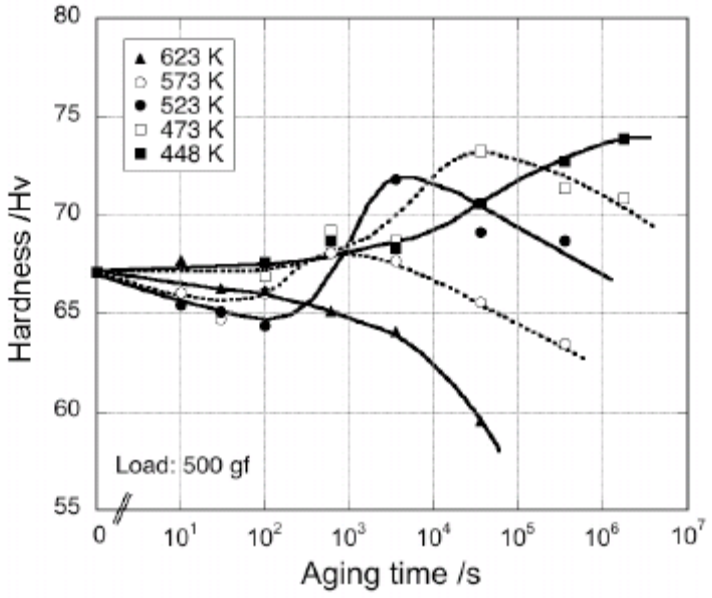


Figure 2.24: Hardness evolution during isothermal aging treatments of the AXJ530 alloy over the 448-623K [Suzuki *et al*. 2007].

#### 2.6.4.2 Precipitation Hardening in Dilute Mg-Ca-Zn Alloys

The first systematic attempt to characterize hardening behaviour in Mg-Ca-Zn alloys goes back to the work by Nie and Muddle [1997]. These researchers investigated the binary Mg-1 wt% Ca alloy, as well as the ternary Mg-1 wt% Ca-1 wt% Zn alloy. The age hardening responses of these alloys are shown in, Fig 2.25a. As this figure illustrates, the age hardening response of the binary alloy is not very significant. However, by adding zinc the aging response is significantly enhanced and the time to the peak hardness is shortened. The beneficial effect of zinc in enhancement of the aging response of the binary Mg-Ca alloy is also recently confirmed by Gao *et al.* [2005], as shown in Fig 2.25.b.

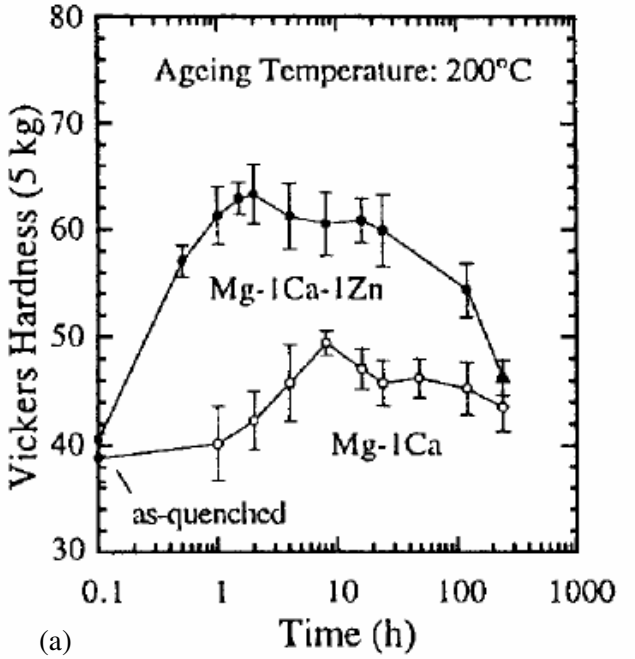


(a)

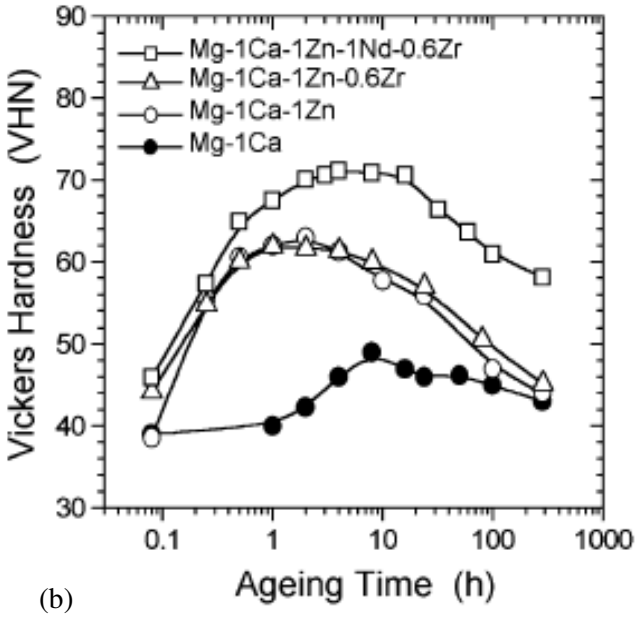


(b)

Figure 2.25: Age-hardening response of the Mg-1 wt% Ca and Mg-1 wt% Ca-1 wt% Zn at isothermal aging temperature of 200°C [Nie and Muddle 1997] in (a), and that of the alloys of Mg-1Ca with Zn, Zr and Nd additions (in wt.%) aged at 200°C [Gao *et al.* 2005] (b).

In addition to the report on the formation of $Mg_2Ca$ in the binary alloy, Nie and Muddle [1997] have reported a ternary intermetallic phase, containing approximately 69 at% Mg, 27 at% Ca and 3.6 at% Zn and a hexagonal crystal structure, in the as-cast Mg-1Ca-1Zn alloy. They have also found two solid state precipitate phases, both thin plate-shaped and with hexagonal crystal structure, in the ternary alloy. The crystallographic data on the intermetallic phases in Mg-Ca-Zn system, as cited by Nie and Muddle [1997], has been included Table 2-5. Nie and Muddle [1997] have not identified any specific phase as the main hardening phase in the ternary alloy of their investigation. They have, however, indicated that the high hardness of the ternary alloy is associated with a very fine and uniform distribution of precipitates. It should be noted that to the best knowledge of the author, there is no literature review on the nature of precipitate-dislocation interactions, and whether the precipitates are sheared or by-passed (i.e. Orowan mechanism), in this alloy system.

Larionova *et al.* [2001] have identified the precipitation of $Ca_2Mg_6Zn_3$ phase, using the XRD analysis, in rapidly solidified Mg-Ca-Zn alloys. It has been reported that the hardness of this phase is similar to that of $Mg_2Ca$ phase [Larionova *et al.* 2001]. Precipitation of $Ca_2Mg_6Zn_3$ phase in aged Mg-1.6 wt% Ca-3.2 wt %Zn alloy and its effect on hardening of the alloy during aging treatment have been reported by Levi *et al.* [2006]. The TEM studies on dilute ternary Mg-Ca-Zn alloys, i.e. alloys with 1.5 wt% Ca and 3-6 wt% Zn, have led to the identification of the crystal structure of the $Ca_2Mg_6Zn_3$ [Jardim *et al.* 2002]. This phase has trigonal structure with lattice parameters of a= 0.97 nm and c=1.0 nm and appear at both

grain boundaries and within the matrix, the latter as spherical and cuboid precipitates [Jardim *et al.* 2002]. Jardim *et al.* [2004] have reported modest age hardening response when the alloys were aged for 1 hour at 200°C. These researchers also conducted hardness measurements after isochronal aging, as well as DSC tests on their alloys of investigation. The results of these tests are shown in Fig 2.26. It should be noted that the large endothermic events in Fig 2.26.b are reported as the melting events for these alloys.

Oh *et al.* [2005] have characterized precipitation process and nano-scale precipitates in Mg-0.3Ca-0.3Zn (at%) alloys by the means of HRTEM and 3-DAP analysis. Formation of monolayer GP zones on the basal planes are shown in the early stages of age hardening. In the over-aged condition $Mg_2Ca$(-Zn) precipitates are formed. The age hardening response of this alloy is reported to be higher than that of Mg-0.3Ca-1.8Zn (at%) alloy.

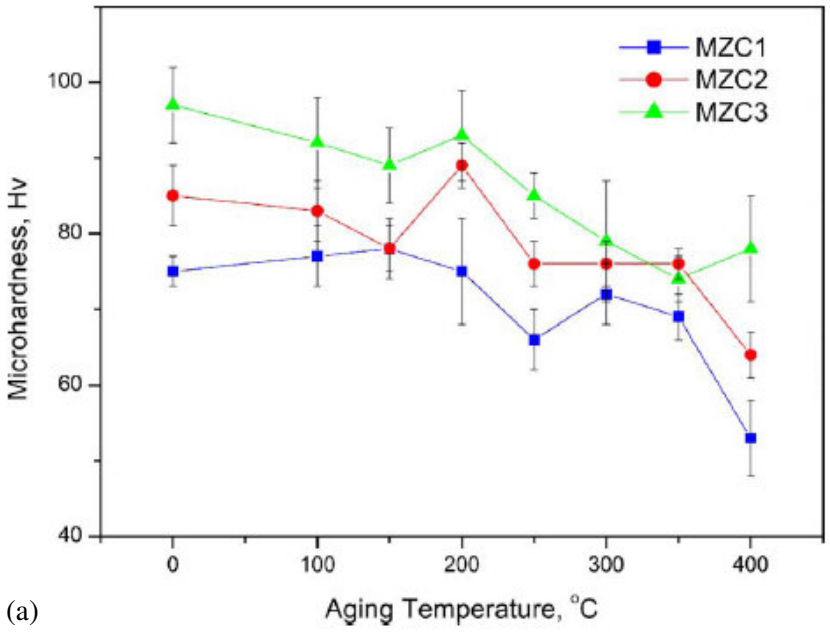


(a)

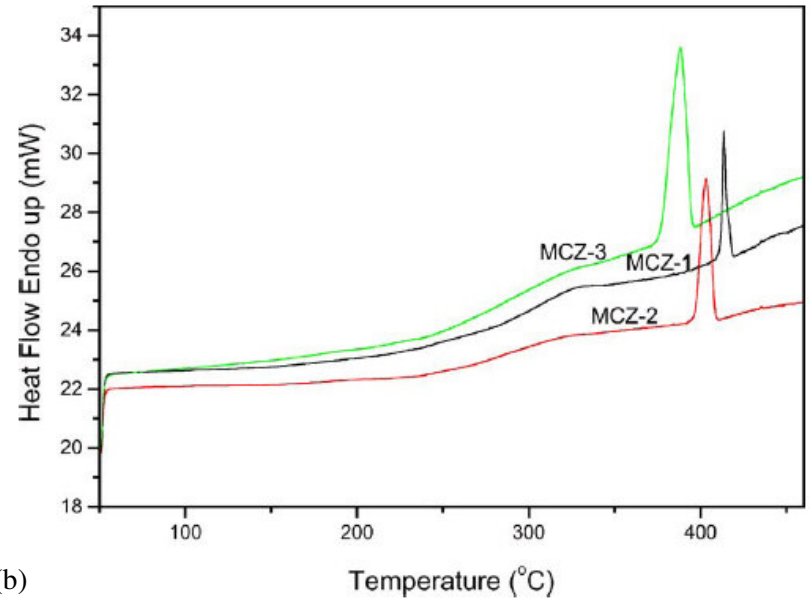


(b)

Figure 2.26: Microardness evolution of the MZC1, MZC2 and MZC3 alloys representing Mg-1.5Ca-(3, 6 and 10) Zn (all in wt.%) alloys after isochronal aging for 1 hour at various temperatures in (a) and DSC traces of the alloys from 50°C-450°C, heating rate 10°C/min in (b) [Jardim *et al*. 2004].

Table 2.5: Lattice parameters of Mg and intermetallic phases in Mg-Ca-Zn system [Villars and Calvert 1985].

| Phase | Mg | $Mg_2Ca$ | Ternary Mg-Ca-Zn | $MgZn_2$ |
|---|---|---|---|---|
| Lattice parameters (a and c in nm) | a=0.321 | a=0.623 | a=0.591 | a=0.522 |
| | c=0.521 | c=1.012 | c=0.965 | c=0.857 |
| Lattice missfit on the habit planes | | 12.10% | 6.30% | -6.10% |

# Chapter 3
# Scope and Objectives

The aim of the present research is to study the homogenization and precipitation hardening behaviour of a binary Mg- 2.5Ca and two Mg-2Ca-1Zn and Mg-2Ca-2Zn alloys.

To study the microstructural characteristics of the binary Mg-2.5Ca and the ternary Mg-2Ca-1Zn and Mg-2Ca-2Zn alloys in as-cast, homogenized and artificial aged conditions techniques which include optical microscopy, scanning electron microscopy (SEM), and X-ray diffraction (XRD) are utilized. To assess the precipitation hardening response of all three alloys, microhardness measurements of homogenized and artificially aged conditions (heated for various times at 175°C, 200°C and 220°C) are performed. Also performed are microhardness measurements on as-cast alloys for comparison purposes. In addition, differential scanning calorimetry (DSC) and isothermal calorimetry (IC) are performed on the homogenized condition of all three alloys to investigate the precipitation behavior of the alloys.

The present work offers an in depth discussion on the development of microstructure, as well as the mechanisms, kinetics of precipitation hardening in the Mg-Ca-Zn alloy system for which there is little literature available. It should be stressed the use of thermal analysis in studying precipitation hardening in magnesium alloys is utilized to a very limited extent in literature and the present research brings new insight into the benefits of thermal analysis in Mg-Ca-Zn alloys.

The ensuing chapter will describe the materials, heat treatment and the equipment employed in the testing, as well as the testing procedures utilized in the present investigation. The results of experimental characterization of microstructural evolution and precipitation hardening response will be brought in Chapter 5. This will be followed by a discussion of the results and a comparison of the microstructure and hardening response between the three alloys. Subsequently conclusions will be deduced and recommendations for future work will be given.

# Chapter 4
# Experimental Methodology

## 4.1 Introduction

This chapter on experimental methodology includes three main categories: materials, thermal processing and material characterization methods. First a brief description of the materials utilized is given. This is followed by the procedure for thermal processing of the binary and ternary alloys. Subsequently the material characterization procedures, including optical microscopy, electron microscopy, microhardness testing, differential scanning calorimetry (DSC), isothermal calorimetry (IC) and X-ray diffractometry (XRD) will be described individually.

## 4.2 As-Cast Materials

As-cast Mg-2.5Ca, Mg-2Ca-1Zn and Mg-2Ca-2Zn (all in wt%), cast in permanent molds were received from CANMET MTL as bars with a diameter of 25 mm and a length of 140 mm. Spectrographic analysis of the bars is given in table 4.1. As Table 4.1 shows Ce, La and Cu are present as impurities in the cast alloys.

Table 4.1: Chemical analysis of as-cast alloys, all numbers are in wt% [Data obtained from CANMET-MTL].

| Alloy | Si | Cu | Zn | Fe | Mn | Al | Ca | Ce | La |
|---|---|---|---|---|---|---|---|---|---|
| Mg-3Ca | 0.006 | <0.005 | <0.05 | <0.005 | <0.005 | <0.01 | 2.5 | 0.015 | 0.026 |
| Mg-2Ca-1Zn | 0.007 | 0.031 | 0.87 | <0.005 | <0.005 | <0.01 | 2.1 | 0.013 | 0.021 |
| Mg-2Ca-2Zn | 0.006 | 0.028 | 1.7 | <0.005 | <0.005 | <0.01 | 2 | 0.01 | 0.022 |

### 4.3 Heat Treatment

This section describes the basis for choosing heat treatment routes for the binary and ternary alloys. Heat treatment for precipitation hardening is comprised of three stages: homogenization, quenching and isothermal or non-isothermal aging. It should be noted that homogenization of as-cast structures and solutionizing for the purpose of precipitation hardening are two different terms. In the present research, however, solutionizing also takes place during the homogenization step and hence solely the term homogenization will be utilized when referring to both concepts. Homogenization time and temperature play important roles in response of the alloys to aging for distributing alloying elements in the solid solution matrix [Reed-Hill and Abbaschian 1991]. Homogenization heat treatment followed by rapid quenching may also increase the concentration of vacancies which assists diffusion of alloying elements during aging increases [Porter and Easterling 1992].

For homogenization and aging treatments of all the alloys two electric air furnaces are used. It should be noted that all samples are wrapped in aluminum foil for protection against extensive oxidation during the heat treatment. After homogenization, samples are quenched immediately in a water bath at room temperature. Samples for aging are put in a thin boat shaped aluminum foil. This boat then is put in the furnace set at the aging temperature. Isothermal aging treatments are performed at 175°C, 200°C and 220°C for times ranging from 15 min up to 72 hours. For non-isothermal aging treatments, homogenized samples are put in the furnace set at 25°C and then aged up to 250°C with heating rate of 1°C/min. Each sample is then taken out after reaching the selected temperature. The possible temperature perturbation due to the opening and closing of the aging furnace is not measured in this work.

It must be stressed that the time interval when the furnace door is open is short. However, cold air can be introduced into the furnace and there can be a time lag between the temperature profile and the actual temperature of the samples. Considering approximately long period of time between two points and monitoring temperature during the non-isothermal aging tests, opening furnace for a short period of time is unlikely to significantly affect the aging response of the samples.

### 4.3.1 Heat Treatment Route for the Binary Alloy

Binary Mg-2.5Ca alloy is heat treated according to the route shown in Fig 4.1.b. The homogenization temperature is chosen based on the solidus temperature of Mg- 2.5 wt% Ca to avoid melting. However, to maximize the aging response of an alloy, the homogenization temperature must be selected as high as possible below the solidus line [Porter and Easterling 1992]. Based on a previous study on the homogenization of Mg-Ca alloys [Langelier and Esmaeili 2006] and considering the Mg-Ca binary phase diagram (Fig. 4.1.a), the homogenization temperature and time are chosen as 505°C and 120 h, respectively.

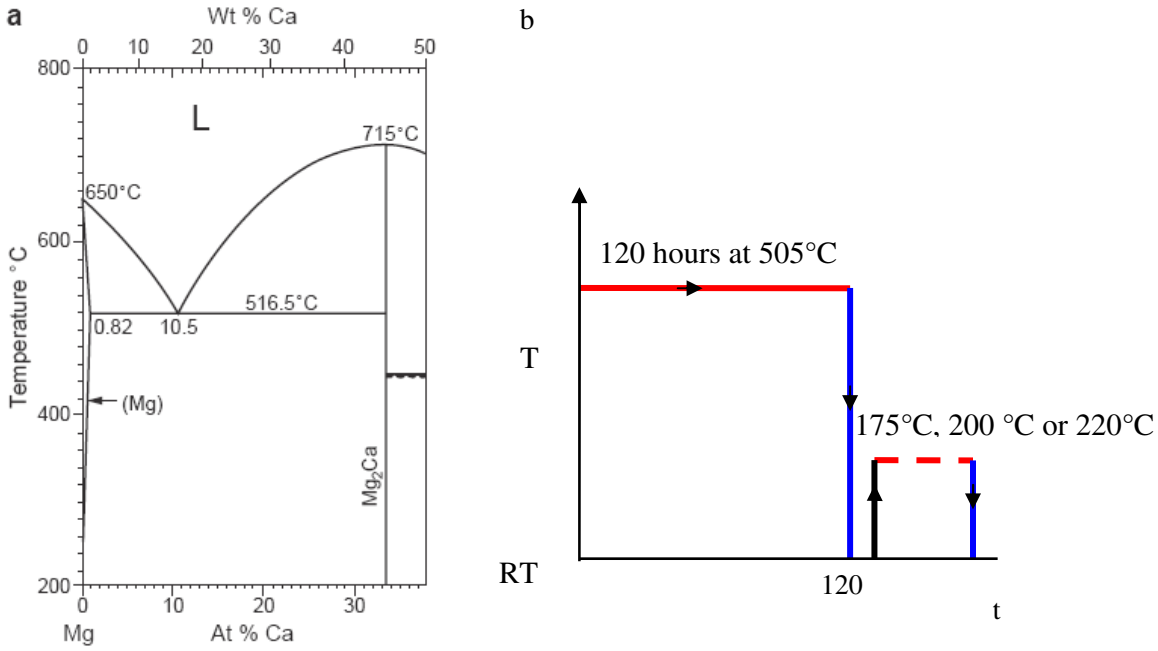


Figure 4.1: Mg rich part of the Mg-Ca binary phase diagram (a) and schematic presentation of homogenization and aging treatment of binary Mg-3Ca alloy (b).

### 4.3.2 Heat Treatment Route for the Ternary Alloy

In the ternary Mg-2Ca-xZn alloys, the homogenization temperature is selected based on calculations by the Thermocalc software for the solidus temperatures of Mg-3 wt% Ca-1 wt% Zn and Mg-3 wt% Ca- 2 wt% Zn alloys which are found to be 498°C and 479°C, respectively. Also following Levi *et al.* [2006], since there is a high possibility of melting eutectic phases in the interdendritic regions, the ternary alloys are first homogenized for 48 hours at 300°C, followed by a 96 hour homogenization treatment at 455°C and 450°C (for alloys containing one and two weight percent zinc, respectively) [Levi *et al.* 2006]. Fig 4.2 shows the heat treatment route for the ternary alloys schematically.

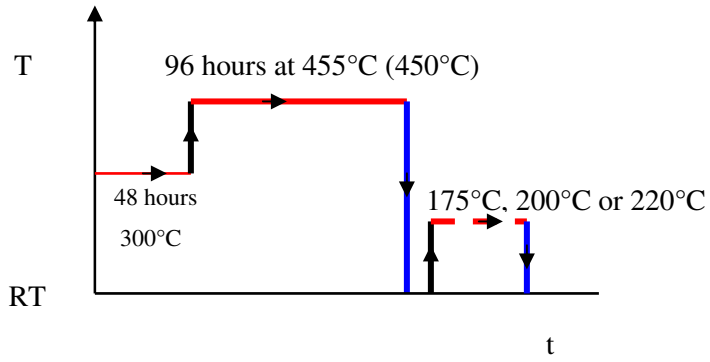


Figure 4.2: Schematic presentation of homogenization and aging treatment of ternary alloys.

## 4.4 Characterization Methodology

In this section, the methods used for material characterization will be introduced. The microstructure of as-cast and heat treated alloys is studied with the aid of optical and electron microscopy. Vickers microhardness and thermal analysis are used to monitor the precipitation hardening response of the alloys, while XRD is used to identify various phases in the as-cast and heat treated samples of the alloys.

### 4.4.1 Metallographic Preparation Procedure

All samples, binary and ternary, are prepared according to the metallographic procedure shown in Fig 4.3.

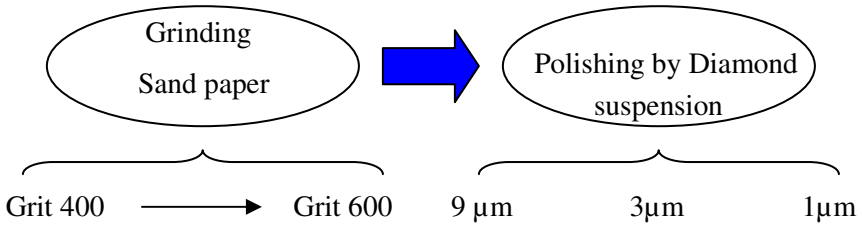


Figure 4.3: Metallographic procedure for sample preparation.

For high quality microscopy images, some samples are more finely polished using a 0.25 µm diamond suspension. After each polishing step the samples are cleaned with water and alcohol, these are followed by drying with compressed air. In order to get the desired microstructural results, different etchants such as HCL, ethylene glycol, HF, and acetic glycol are prepared according to the ASM metals handbook [Padfield 2004] and tested on the as-polished alloys. One etchant however, acetic glycol (1 ml $HNO_3$, 20 ml acetic acid, 60 ml ethylene glycol and 20 ml water) reveals grain boundaries and is suitable for revealing more microstructural details. Dilute $HNO_3$ is also used [Levi *et al.* 2006]. Although two etchants do not differ much in terms of revealing microstructural characteristics, $HNO_3$ reveals needle-shaped features not exposed by acetic glycol etchant.

### 4.4.2 Optical Microscopy Analysis

Optical microscopy is implemented by Olympus optical microscope to study microstructure of the as-cast and heat treated samples. Optical images with magnification of 50x to 1000x are studied.

### 4.4.3 Electron Microscopy Analysis

Scanning electron microscopy is performed using a JEOL-JSM6460 scanning electron microscope to investigate (a) microstructural features and (b) elemental distribution in the as-cast and heat treated samples. Images are collected in the secondary electron imaging mode with 20 kV working voltage and beam diameter of 40 µm. The composition analysis is performed with an energy dispersive spectroscopy (EDS) with Oxford Instruments Inca X-ray setup. To study elemental distribution, line scans are also performed.

Transmission electron microscopy analysis is performed by V.Y. Gertsman at CANMET-MTL on the samples heat treated at the University of Waterloo and using a Philips CM20FEG TEM operating at 197kv. Heat treatment history of the samples is presented in Table 4.2 Bright filed imaging mode and STEM-EDS with a probe diameter of 1 nm are used to investigate microstructural features such as distribution, morphology and chemical composition of precipitates.

Table 4.2: Heat treatment history of the samples used for TEM analysis.

| Alloy | Heat treatment | | |
|---|---|---|---|
| Mg-2Ca-1Zn | Homogenized and aged 30 min at 175°C | Homogenized and aged 6 hours at 175°C | Homogenized and aged 10 hours at 175°C |

### 4.4.4 Microhardness Test

To investigate the precipitation hardening response of the alloys, the evolution of hardness is monitored at various times during isothermal aging. Homogenized samples in the as-quenched state are aged at 175°C, 200°C and 220°C and hardness evolution is measured by

Vickers microhardness test with force of 300gf. In addition, to study hardness evolution associated with DSC traces, homogenized samples are ramp heated with the same heating rate as the DSC runs, i.e.1°C/min, and microhardness measurements on non-isothermally aged samples are performed. It is worth mentioning the microhardness tester is calibrated by the standard block prior to measurements. Five indentations are made on each sample, and the average of readings are taken and multiplied by the calibration factor of the machine, i.e. 0.2414, to obtain average of diagonals of an indentation. Vickers microhardness is then calculated by:

$$VHN = \frac{1854.4 \times F}{d^2} \tag{4.1}$$

where $F$ is load in gf and d is the average of diagonals of the indentation.

To monitor hardness evolution within α-Mg grains in all samples, indentations are made on the grains. A typical microhardness indentation is shown in Fig 4.4.

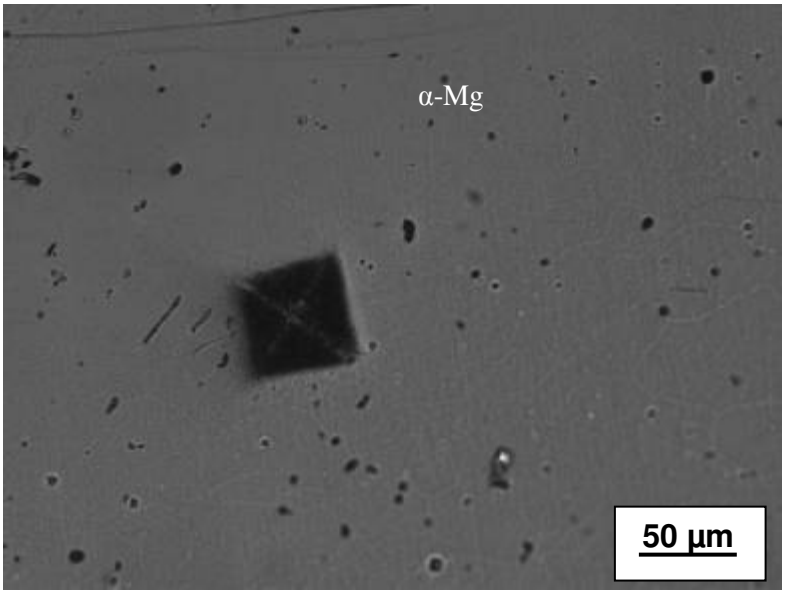


Figure 4.4: Microhardness indentation on Mg-2Ca-1Zn alloy aged for 6 hours at 175°C.

In microhardness data analysis, an indentation with more than 10 percent difference in diagonals ($d_1$ and $d_2$) is omitted according to the ASTM [2007]. Error analysis is based on the assumption that the errors arising in microhardness readings are consistent in all measurements and that the microhardness data has normal distribution. Therefore for each aging curve, i.e. any alloy at one of the isothermal aging temperatures, pooled standard deviation is calculated and error bars are based on this pooled standard deviation. Pooled standard deviation for an aging curve comprised of n points, e.g. n different aging times, and m number of measurements for each of the n points is [Wall 1986]:

$$\sigma = \frac{\sum_{i=1}^{n}\sum_{j=1}^{m}\left(x_{ij} - \bar{x}_i\right)^2}{N-n} \tag{4.2}$$

where σ is the pooled standard deviation, N is the total number of accepted microhardness data of an aging curve. Upon calculation of the σ, error bars on the microhardness data are introduced as the standard error of the mean [Montgomery *et al.* 1997]:

$$e = \frac{\sigma}{\sqrt{N}} \tag{4.3}$$

### 4.4.5 Thermal Analysis

The procedure for thermal analysis, utilizing both differential scanning calorimetry (DSC) and isothermal calorimetry (IC) will be presented in this section. The procedure for obtaining baselines, analysis and correction of raw data will be discussed in detail in this section.

Thermal analysis is performed with a C80 Setaram calorimeter. In all DSC and IC experiments, samples are dropped into the sample vessel while the reference vessel is kept empty. It should be mentioned that DSC and IC runs, have been repeated at least two times for each condition to assure the repeatability of the results. Both DSC and IC tests have been conducted in an air atmosphere.

#### 4.4.5.1 Procedure for Obtaining Baseline

For both DSC and IC runs, the first step is to obtain a repeatable reference test run under the same thermal profile as the alloy sample test runs. For this purpose, pure magnesium samples with mass of 1100 ± 5 mg are dropped in the sample vessel; subsequently DSC run is performed from 30°C -300°C with heating rate of 1°C/min. Since all DSC and IC runs are done under atmospheric conditions and pure magnesium is chosen for the baseline, the possibility that an exothermic peak due to the oxidation of pure magnesium could result in a

false interpretation of the data, is investigated. Thus results of pure magnesium runs are compared with pure aluminum runs. A comparison of a pure aluminum and a pure magnesium DSC trace can be seen in Fig 4.5. It is found that similar slopes for both magnesium and aluminum in DSC and IC traces are observed. This suggests that pure magnesium can be used over this temperature range without extensive oxidation. It should also be added that visual inspection on pure magnesium after baseline runs shows no sign of oxidation.

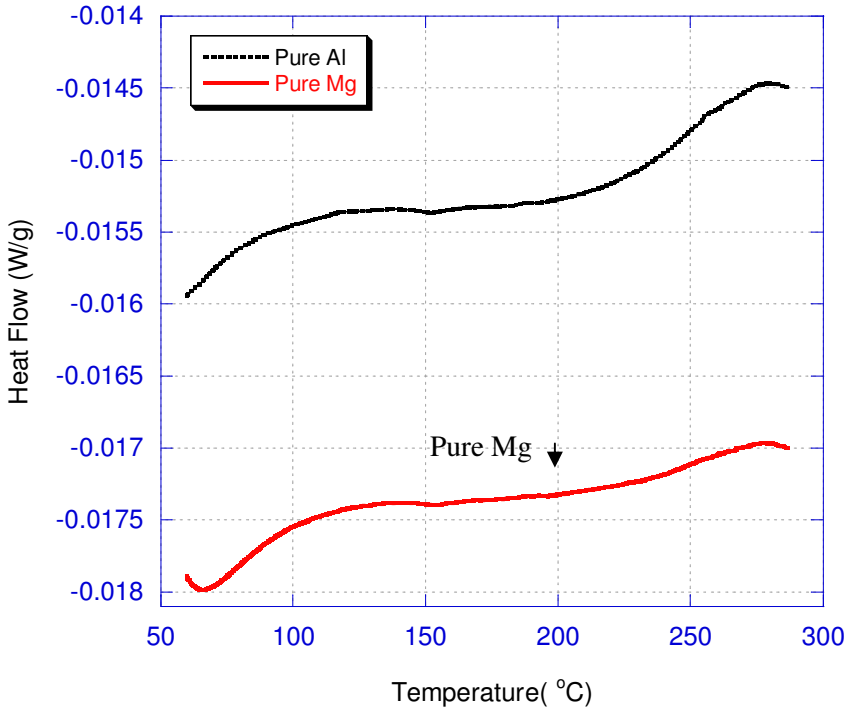


Figure 4.5: Comparison of pure magnesium and pure aluminum run.

#### 4.4.5.2 Differential Scanning Calorimetry Analysis

Differential scanning calorimetry is implemented to study the microstructural evolution in homogenized (as-quenched) samples of the binary and ternary alloys. In this investigation DSC experiments employ a heating rate of 1°C/min from 30°C to 300°C. The mass of the samples are 1090±5mg. After correction for the mass difference, baseline of pure magnesium is then subtracted from the DSC traces of homogenized samples of Mg- 2.5Ca, Mg-2Ca-1Zn and Mg-2Ca-2 Zn and the net heat flows are obtained. To find the zero heat flow line in the DSC traces, the overaged sample of Mg-2Ca-1Zn which was aged for 96 hours at 300°C, Fig 4.6, was chosen as the zero heat flow line. Following choosing this zero heat flow line, DSC traces of the homogenized alloys are shifted vertically according to this zero heat flow line. Initial disturbance effects in heat flow as a result of introducing sample to the test vessel is detected up to 60°C and removed from the test results.

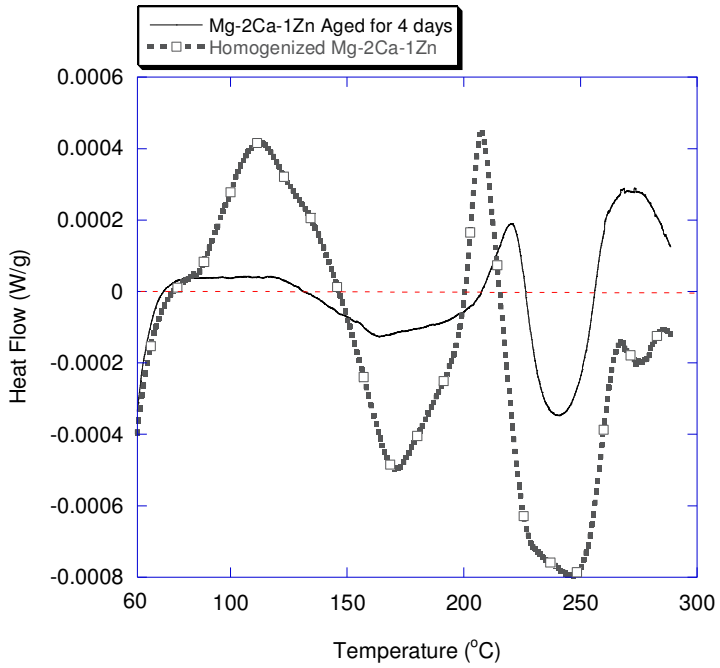


Figure 4.6: Schematics of choosing zero heat flow line to interpret DSC traces of the alloys.

#### 4.4.5.3 Isothermal Caloremetry Analysis

Isothermal calorimetry is conducted on homogenized, as-quenched, samples at aging temperatures of 175°C, 200°C and 220°C. Prior to a desired isothermal run, the calorimeter is stabilized for 3 hours. The drop test method as described by Esmaeili and Lloyd [2005 a] is applied. Baselines are obtained at each temperature and subtracted from the trace of the homogenized alloy to obtain a final trace for the alloy. As a result of opening the vessel and dropping the sample in there is a large endothermic effect in the trace that should be corrected [Esmaeili and Lloyd 2005 a] . This time lag for the present IC experiments in this work is around 400 seconds. Each trace is then corrected, by subtracting this initial time shift ($\Delta t_0$) from the time axis of the trace, i.e. $t_{finaltrace} = t - \Delta t_0$ . Schematic procedure for obtaining the final trace in isothermal calorimetry is shown in Fig 4.6. Two quantitative values from each isothermal calorimetry trace are obtained, total heat flow and $t_f$, (i.e. the characteristic time that heat evolution becomes so small to be measured) [Esmaeili and Lloyd 2005 a]. Total heat flow, the area under the trace, is expressed as: $\int_0^{t_f} \left( \frac{dQ}{dt} \right) dt$ .

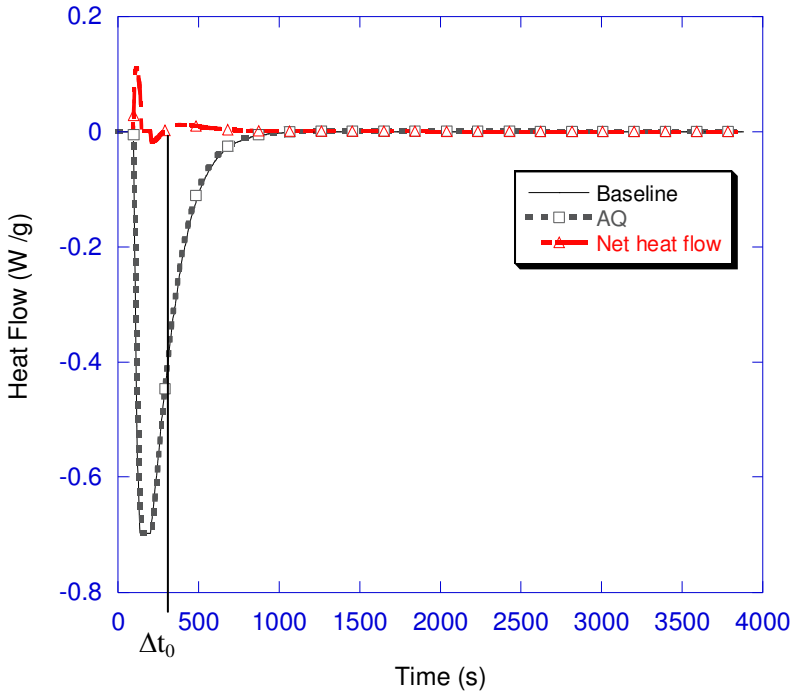


Figure 4.7: Schematic procedure for obtaining the final trace of a homogenized alloy; $\Delta t_0$ is shown by an on the final trace.

#### 4.4.5.4 XRD analysis

The phase identification of the alloys is performed using X-ray diffraction. For this a Philips machine SA-HF3 with a tungsten filament operating at 50 kV and 40 mA producing Cu-Kα radiation with a wavelength of 0.1542 nm is used. X-ray spot diameter is chosen as 300 µm with a step size of 0.02° scanning 2θ degrees between 10° to 90°. XRD is implemented on as-polished alloys in the as-cast condition for all three alloys and on the ternary alloys which are aged for six hours at 175°C. The XRD results are analyzed by the Areamax software for phase identification. For each of the identified phases, relative intensity of three major peaks, i.e. $\frac{I}{I_0}$ where I is the intensity in the spectrum and $I_0$ is the

highest intensity of the corresponding phase, are calculated and compared to the standard X-ray lines of each phase to verify identification process. Table 4.3 gives standard lines of the main phases studied in the present investigation.

Table 4.3: Standard X-ray diffraction lines of the phases used for the analysis in the present investigation.

Mg

| 2θ | $I/I_0$ |
|---|---|
| 36.619 | 100 |
| 34.398 | 36 |
| 32.193 | 25 |
| 47.828 | 15 |
| 63.056 | 16 |
| 68.631 | 13 |

$Mg_2Ca$

| 2θ | $I/I_0$ |
|---|---|
| 33.796 | 100 |
| 31.137 | 75 |
| 28.401 | 45 |
| 52.228 | 30 |
| 53.886 | 25 |
| 56.781 | 20 |

$Ca_2Mg_6Zn_3$

| 2θ | $I/I_0$ |
|---|---|
| 36.962 | 100 |
| 33.152 | 65 |
| 21.136 | 40 |
| 41.583 | 30 |
| 52.164 | 18 |
| 69.581 | 10 |

$CaCu_{0.8}Zn_{0.2}$

| 2θ | $I/I_0$ |
|---|---|
| 38.681 | 100 |
| 30.938 | 53 |
| 18.77 | 41.8 |
| 32.296 | 36.9 |
| 34.523 | 36.5 |
| 17.204 | 24.9 |

# Chapter 5
# Experimental Results

## 5.1 Introduction

This chapter presents the experimental results produced from the characterization methods described in the previous chapter and is categorized according to alloy composition. The results will include microscopy analysis, hardness evolution as a function of time and temperature during aging of the alloys, DSC and IC traces, and non-isothermal aging curves. Phase identification based on XRD results will wrap up each section. Summary of different microstructural features observed in the present investigation will bring the end to this chapter.

## 5.2 Evolution of the Microstructure Characteristics and Hardness during Homogenization and Aging - Mg-2.5Ca

Microstructural evolution as a result of homogenization and aging heat treatment of the Mg-2.5Ca alloy is studied in this section. Microstructural characteristics of the as-cast and heat treated binary alloy, e.g. morphology of phases and distribution of the alloying element will be presented. Aging response of the alloy will be presented by the evolution of hardness during aging at isothermal aging temperatures of 175°C, 200°C and 220°C. The results of DSC and IC testes on homogenized Mg-2.5Ca will then be presented. XRD spectrum of the as-cast alloy will wrap up experimental results of the binary alloy.

### 5.2.1 Microstructural Evolution of the Mg-2.5Ca Alloy during Homogenization

Figure 5.1.a shows the general microstructural characteristics of the as-cast Mg-2.5Ca alloy. Dendrites of primary α-Mg and eutectic mixture in the interdendritic areas are shown in higher magnification in Fig 5.1.b. SEM micrographs in Figs 5.2 (a and b) show that the eutectic structure in the interdendritic regions is lamellar.

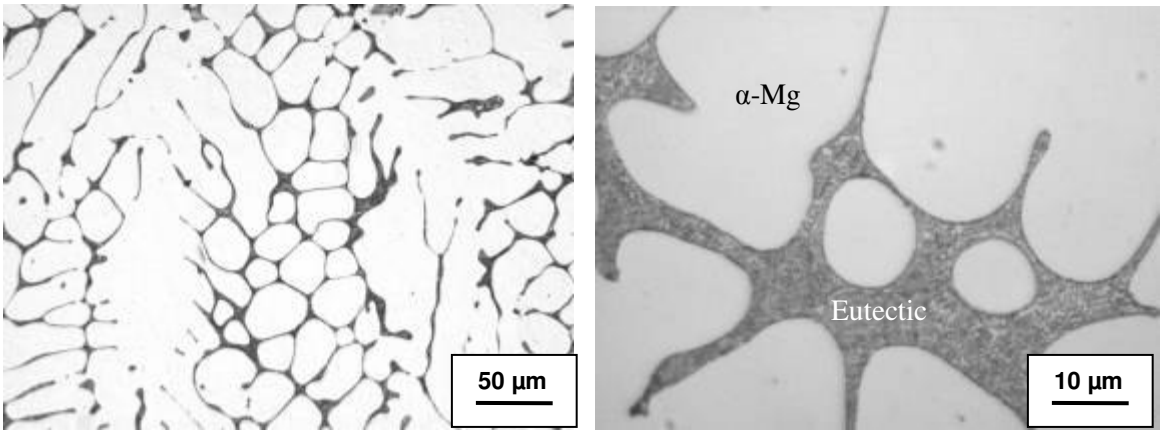


(a) (b)

Figure 5.1: Optical micrographs of the as-cast Mg-2.5Ca (a) showing general view of the as-cast microstructure and (b) higher magnification of the eutectic phase within interdendritic areas.

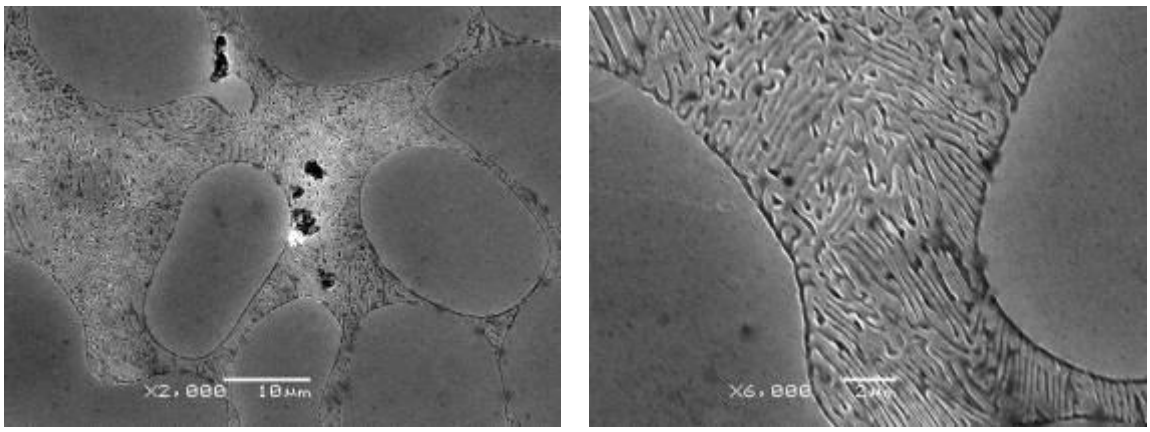

(a) (b)

Figure 5.2: SEM micrographs of the as-cast Mg-3Ca (a) and layered eutectic structure in (b).

Fig 5.3 illustrates the microstructural evolution as a result of homogenization of Mg-2.5Ca alloy. Microstructural changes can be seen by comparing the dendritic microstructure of the as-cast sample in Fig 5.3.a with Figs 5.3 (b and c) which show the microstructure of the homogenized sample. The images reveal that the dendritic microstructure has disappeared in the homogenized sample and the eutectic within the interdendritic regions has transformed to partially spherodized particles within a uniform matrix.

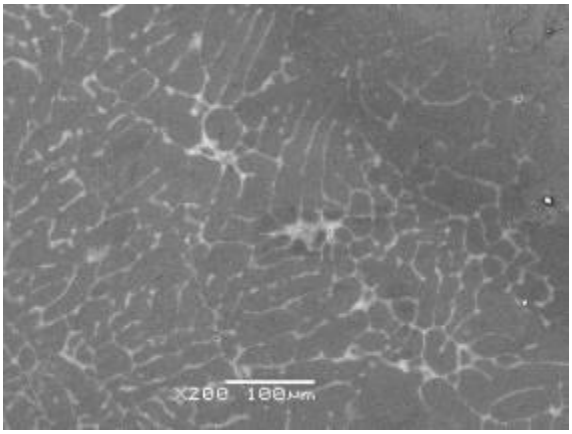


(a)

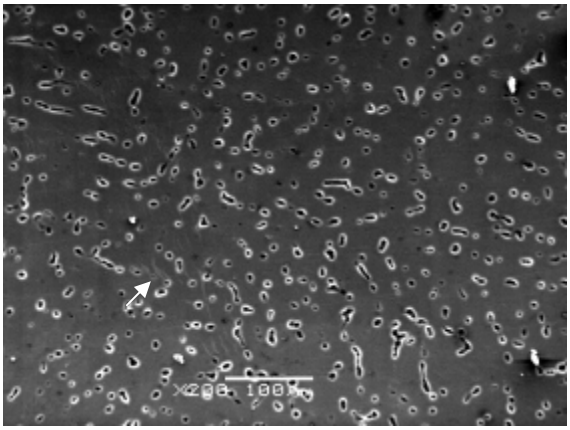

(b)

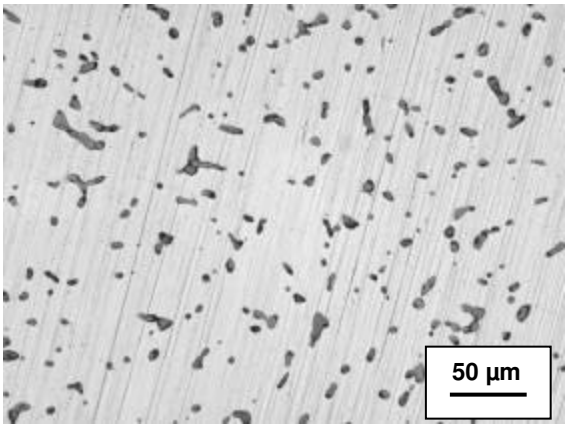


(c)

Figure 5.3 : SEM micrographs of as-polished as-cast Mg-2.5Ca alloy (a), and homogenized sample etched in nitric acid (b). Optical micrograph of a homogenized Mg-2.5Ca alloy, as-polished (200x) (c).

The results of the EDS analysis on the binary alloy in the as-cast and homogenized conditions are shown in Figs 5.4 (a and b), respectively. Fig 5.4.a shows little solubility of calcium in primary α-Mg and a large amount of calcium in the eutectic structure. As Fig 5.4.b illustrates, homogenization has produced relatively large calcium rich particles with an

average calcium content of 35 wt%. A white shadow around the particles in Fig 5.4.b is noticeable; also there are smaller calcium rich particles located in region 3 in Fig 5.4.b.

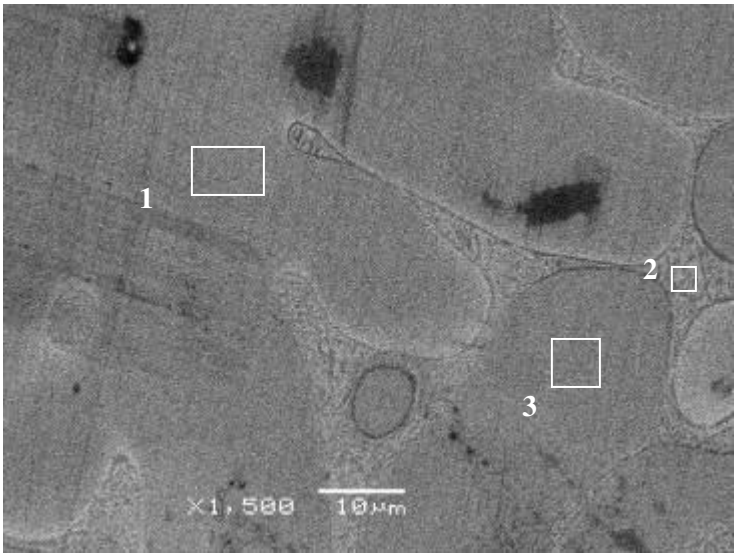


| Spectrum | Mg | Ca |
|---|---|---|
| 1 | 99.15 | 0.85 |
| 2 | 83.26 | 16.74 |
| 3 | 99.45 | 0.55 |

(a)

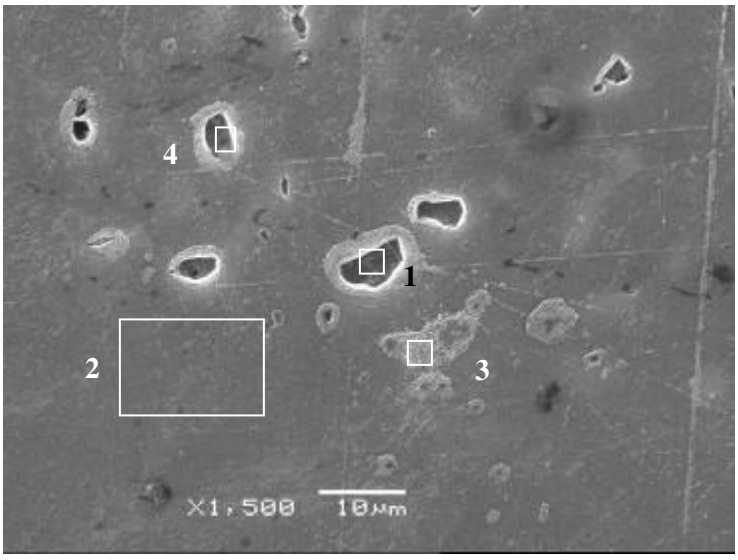


| Spectrum | Mg | Ca |
|---|---|---|
| 1 | 62.61 | 37.39 |
| 2 | 99.43 | 0.57 |
| 3 | 86.69 | 13.31 |
| 4 | 66.87 | 33.31 |

(b)

Figure 5.4: EDS analysis of as-cast Mg-2.5Ca (a) and homogenized Mg-2.5Ca (b); both in the as-polished condition; all results are in wt%.

### 5.2.2 Microstructural Evolution of the Mg-2.5Ca Alloy during Aging

The sample aged for 6 hours at 175°C is selected for the presentation of microscopy studies on aged samples. An optical micrograph of the aged sample, Fig 5.5.a shows similar features to the homogenized alloy, Fig 5.3.c. Similar to the case of homogenized sample, second phase particles which are partly spherodized are dispersed in the matrix. SEM analysis on the aged Mg-2.5Ca, Fig 5.5.b, shows large second phase particles dispersed along the grain boundaries of α-Mg matrix. There is also a large population of tiny particles on α-Mg grain boundaries, shown by the oval in Fig 5.5.b, and around large particles. EDS analysis shows only small calcium content for these particles compared to the content of large particles on the grain boundaries, i.e. 20 wt%. EDS analysis of the sample confirmed the calcium content of α-Mg grains to be as low as 0.6 wt%. As a result of applying etchant, oxygen is detected in the EDS spectrum.

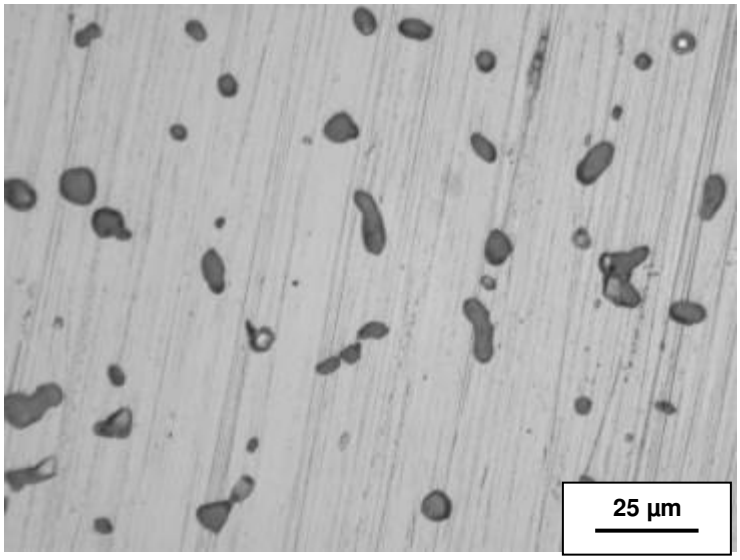


(a)

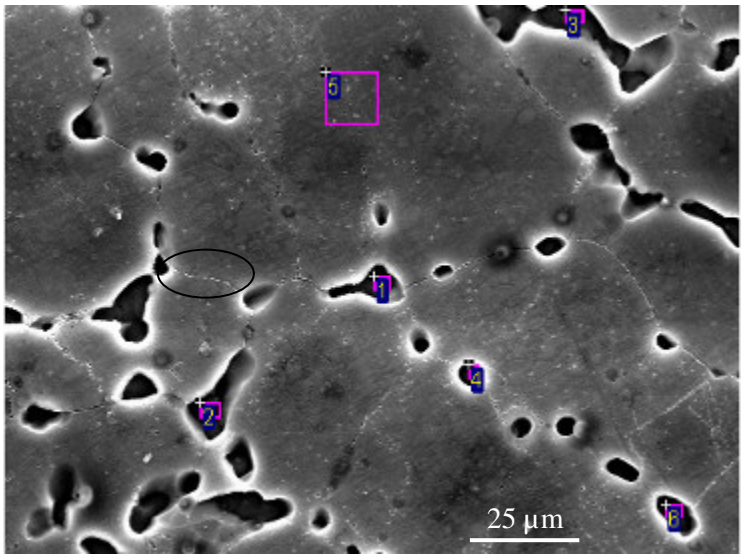


(b)

| Spectrum | O | Mg | Ca |
|---|---|---|---|
| 1 | 4.67 | 75.77 | 19.56 |
| 2 | 6.97 | 80.63 | 12.4 |
| 3 | 7.65 | 77.06 | 15.29 |
| 4 | 4.85 | 66.41 | 28.74 |
| 5 | 1.27 | 98.3 | 0.44 |
| 6 | 4.45 | 78.03 | 17.52 |

Figure 5.5: An optical micrograph of Mg-2.5Ca aged for 6 hours at 175°C, as-polished (a) and EDS analysis of the same sample; etched in acetic glycol (b); all results are in the wt%.

### 5.2.3 Hardness Evolution of the Mg-2.5Ca Alloy during Isothermal Aging

Aging response of Mg-2.5Ca at 175°C, 200°C and 220°C is presented in this section. Fig 5.6 shows that as a result of the homogenization heat treatment, the hardness of the as-cast alloy declines from 55 VHN to 50 VHN. At 175°C and 200°C, hardness increases from 50 VHN to 54 VHN after four hours of aging. At longer aging times, hardness decreases and seems to fluctuate around 52 VHN. On the other hand, at 220°C the peak hardness, e.g. 52 VHN, is obtained at shorter aging times after only 1 hour, and is more readily distinguished from the whole aging curve. The significant scatter in the entire aging data prevents to create smooth aging curves with clear under-aged, peak-aged and over-aged regimes. This does not allow the aging responses at the 3 different temperatures and for the 3 alloys to be clearly compared. In order to solve this problem, representative hardness points of each data series are selected for each temperature. This allows that approximate aging curves are created. The resultant aging curves are shown in Fig 5.7. As this figure shows, aging curves at 175°C and 200°C show very similar regimes while at 220°C the maximum hardness is smaller and the rate of decrease in hardness after the peak-aged condition is faster.

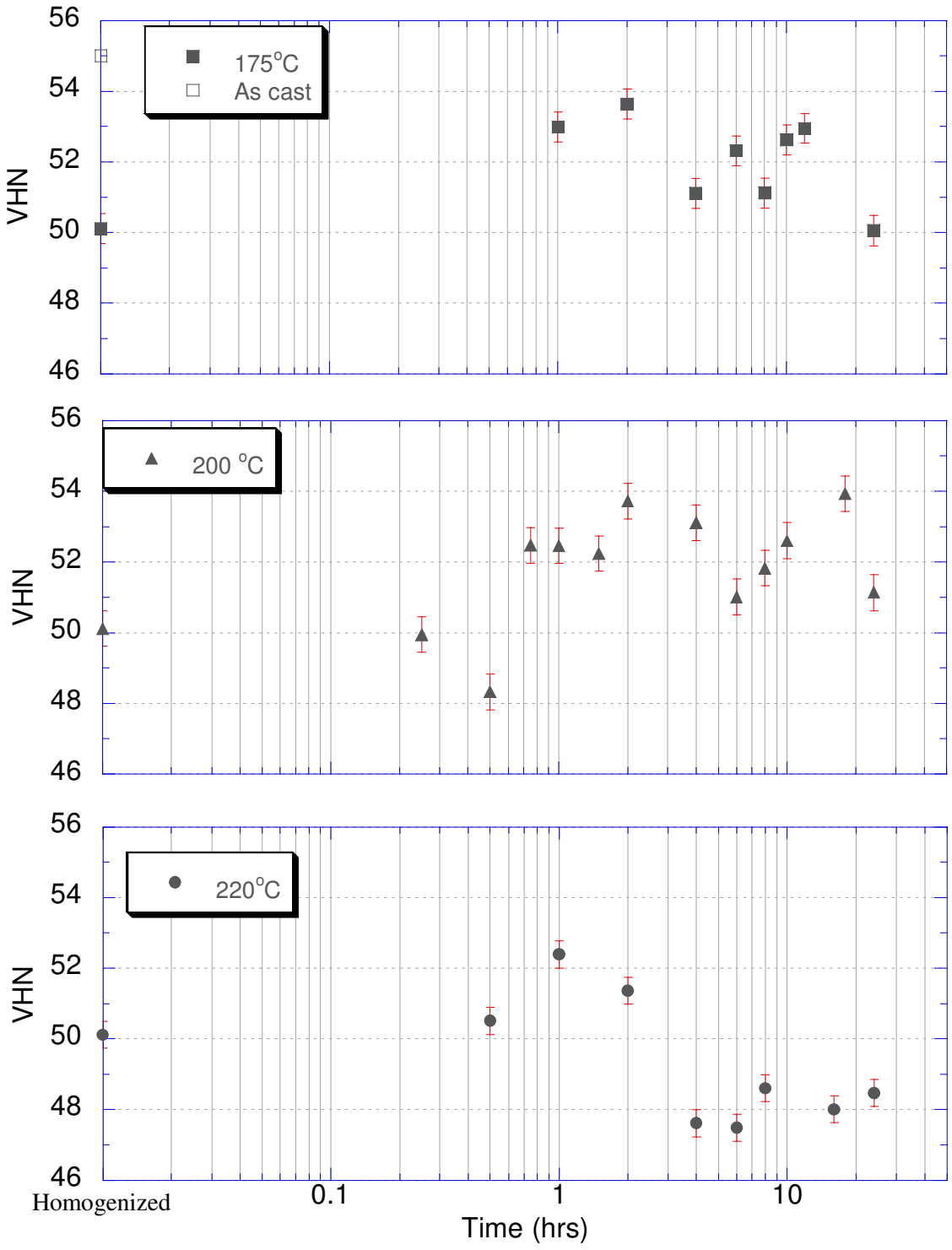


Figure 5.6: Microhardness evolution of homogenized Mg-2.5Ca during isothermal aging at 175°C, 200 °C and 220°C.

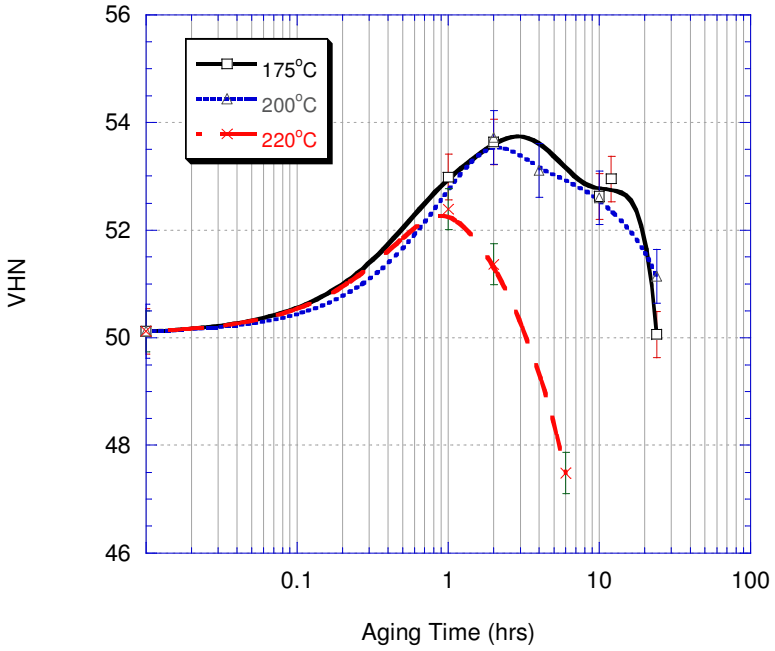


Figure 5.7: Isothermal aging curves of the homogenized Mg-2.5Ca at 175°C, 200°C and 220°C.

### 5.2.4 IC Results

IC traces of homogenized Mg-2.5Ca alloy are shown in Fig 5.8. There is no measurable heat evolution at 175°C and the heat flow during the run shows the same pattern as the baseline. At 200°C, the rate of heat release ($\frac{dQ}{dt}$) reaches a maximum after 6 minutes of aging and then decays to a very-low constant value at $t_f$ = 8.5h. The trace for aging at 220°C, however, shows a significantly higher peak of heat release which is achieved in the aging time range of 10 minutes to 150 minutes. The time to reach $t_f$ is very similar to the case of aging at 200°C. Characteristic information obtained from IC traces including, $t_f$ and total heat

evolution, i.e. $\int_0^{t_f}\left(\frac{dQ}{dt}\right)dt$ , are presented in the Table 5.1. It should be noted that the total heat release at 220°C is much higher than the one at 175°C and 200°C.

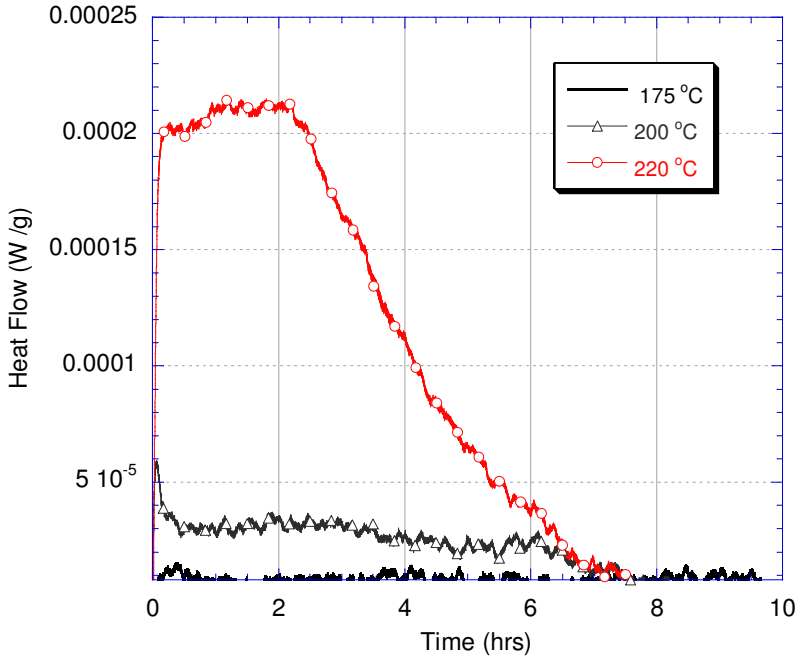


Figure 5.8: The isothermal calorimetry traces for homogenized Mg-3Ca samples during aging at 175°C to 220°C.

Table 5.1: The values obtained for $t_f$ and the total heat evolved during the isothermal calorimetry of the homogenized Mg-2.5Ca at various temperatures.

| Aging Temperature (°C) | tf (hr) | Total Heat (J/g) |
|---|---|---|
| 175 | NA | NA |
| 200 | 8.5 | 0.72 |
| 220 | 8 | 3.247 |

### 5.2.5 DSC Results

A DSC trace of homogenized Mg-2.5Ca alloy is presented in Fig 5.9. It is observed that there is no change in heat flow from 80°C to approximately 150°C. Further increase in the temperature results in a slow increase in the heat flow between 150°C to approximately 200°C. This increase is followed by a major exothermic peak in the temperature range of 200°C to 280°C. The maximum heat flow occurs at 260°C. It is evident that the DSC trace does not show any endothermic effect.

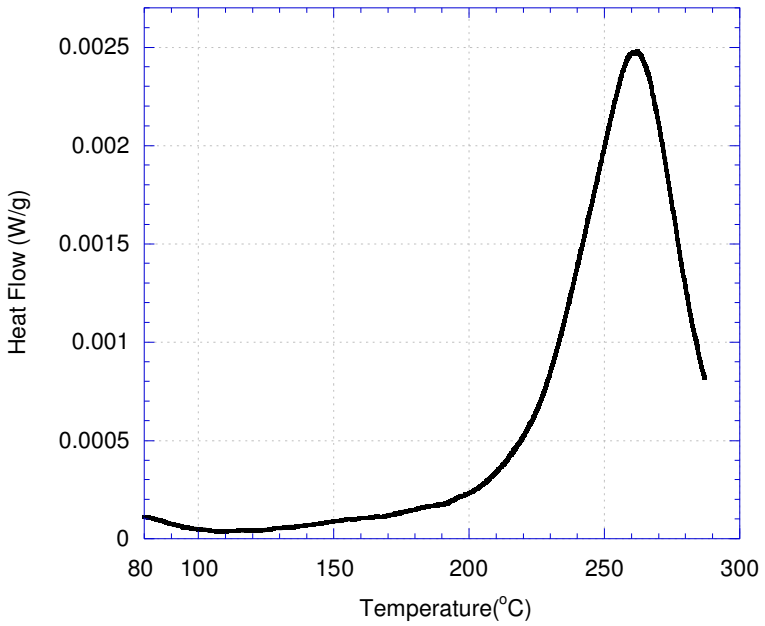


Figure 5.9: DSC trace of homogenized Mg-2.5Ca from 80-300°C; heating rate of 1°C/min.

### 5.2.6 Hardness Evolution during Non-Isothermal Aging

Fig 5.10 shows hardness evolution as a result of the non-isothermal aging of the homogenized Mg-2.5Ca alloy with heating rate of 1°C/min, which is the same heating rate of the DSC tests and up to 250°C. As this figure illustrates hardness increases from 50 VHN in

the as-quenched state, i.e. 25°C, to slightly more than 52 VHN at 250°C. Hardness increment is marginal, only 4%.

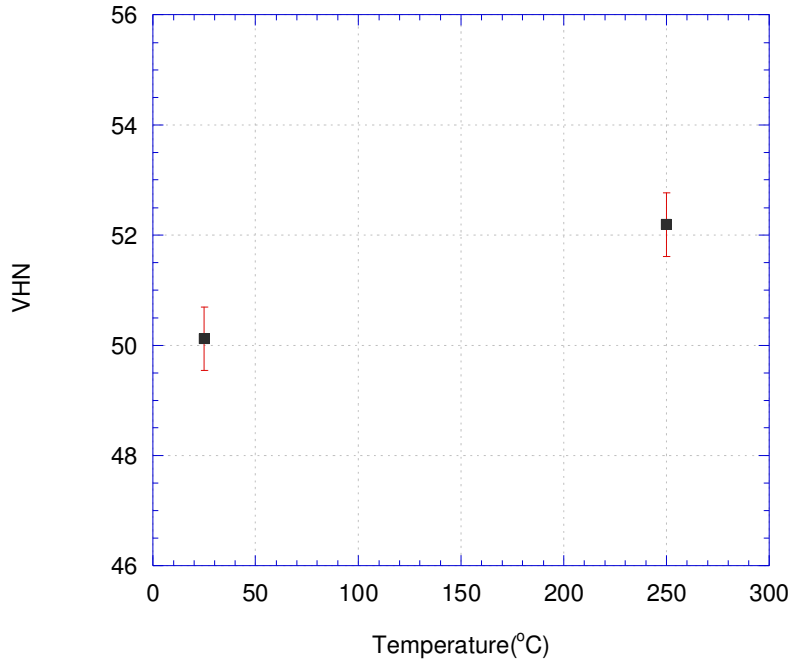


Figure 5.10: Hardness evolution in the homogenized Mg-2.5Ca heated with heating rate of 1°C/min to 250 °C.

### 5.2.7 XRD Analysis of Mg-2.5Ca

XRD spectrum of the as-cast Mg-2.5Ca is shown in the Fig 5.11. α-Mg and $Mg_2Ca$ are the phases identified by XRD.

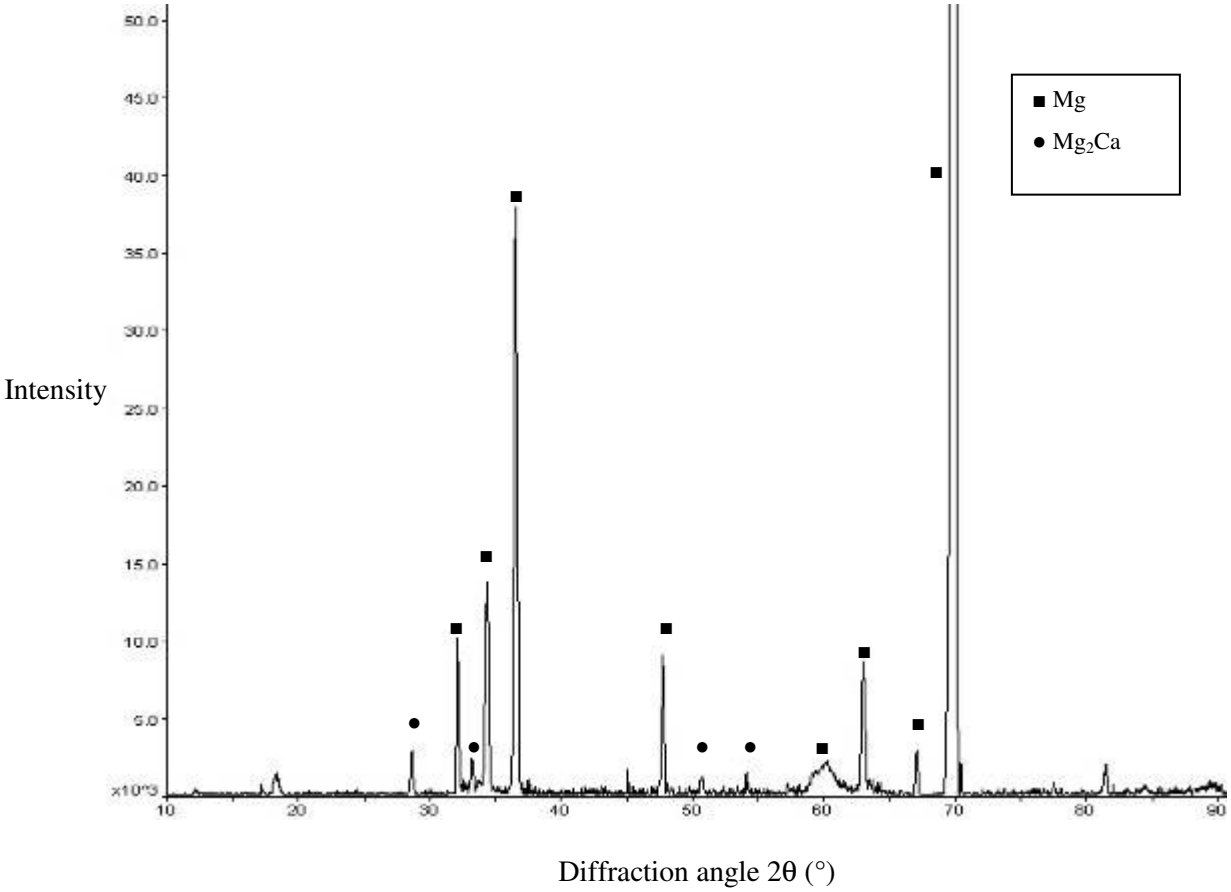


Figure 5.11: XRD spectrum of the as-cast Mg-2.5Ca.

## 5.3 Evolution of the Microstructural Characteristics and Hardness during Homogenization and Aging- Mg-2Ca-1Zn Alloy

Experimental results on microstructural evolution and precipitation hardening response of the Mg-2Ca-1Zn alloy are presented in this section. Results will be presented as the same fashion for the binary alloy.

### 5.3.1 Microstructural Evolution of the Mg-2Ca-1Zn Alloy during Homogenization

General microstructural characteristics of the as-cast Mg-2Ca-1Zn alloy are shown in the Fig 5.12. The as-cast structure is comprised of primary α-Mg dendrites surrounded by the interdendritic phases. Higher magnification of the interdendritic regions is presented in Fig 5.12.b showing two distinct phases and the formation of the phases next to each other.

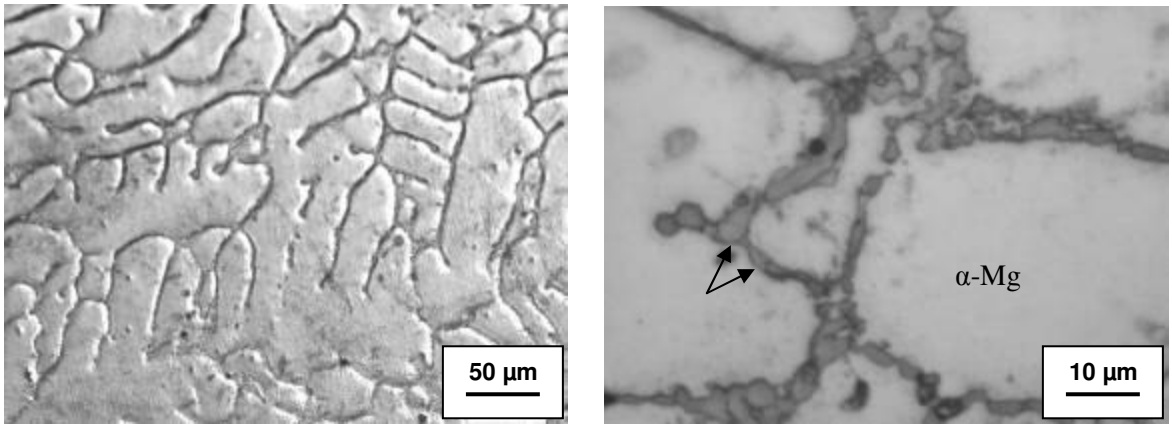


(a) (b)

Figure 5.12: Optical micrographs of the as-cast Mg-2Ca-1Zn alloy showing general view of the as-cast microstructure (a) and higher magnification of the interdendritic regions, (as-polished), (b).

SEM imaging of the as-cast structure provides better contrast of the phases in the microstructure. Fig 5.13.a shows the dendritic microstructure of α-Mg (dark) and interdendritic phases (bright). Fig 5.13.b shows the presence of white ribbons in the interdendritic regions. EDS analysis on the area indicated by the balck box in Fig 5.13.b showed calcium content of primary α-Mg dendrites as 0.65 wt.%. No reading is obtained for the zinc content.

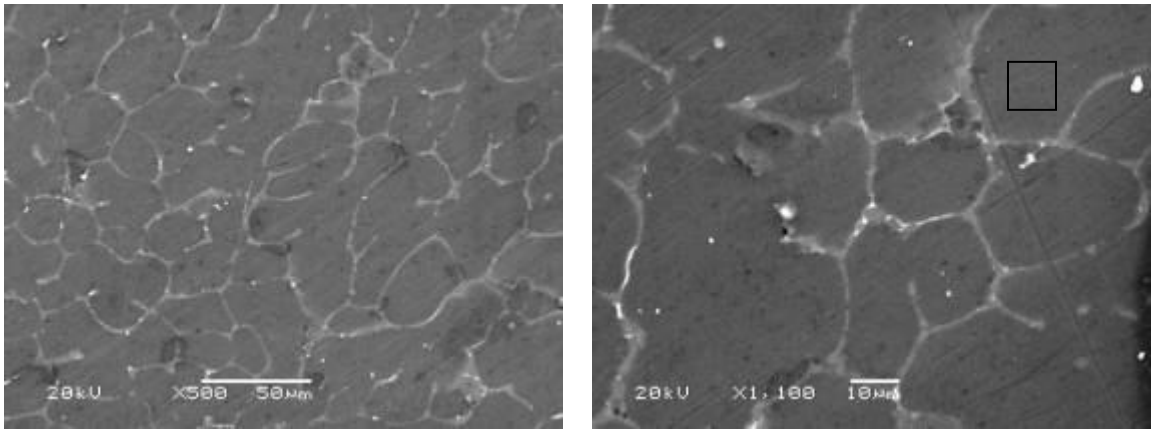


(a) (b)

Figure 5.13: SEM micrographs of the as-cast Mg-2Ca-1Zn alloy (a), and higher magnification of the interdendritic regions, (as-polished), (b).

The EDS analysis on the distinct particles within the grayish interdendritic phase is given in Fig 5.14. The calcium content of the grayish interdendritic phase, i.e. spectrum1, is close to 18 wt% while the white phase, i.e. spectrum 3, is mainly composed of zinc and magnesium with much less calcium content, i.e. 4.7 wt%.

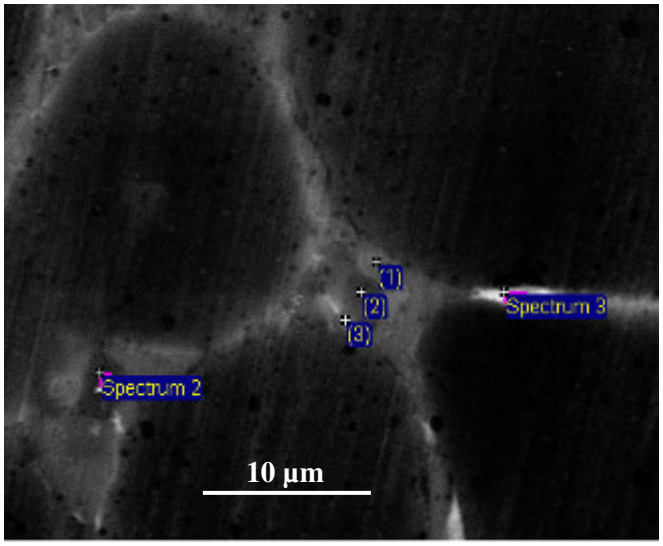


| Spectrum | Mg | Ca | Zn |
|---|---|---|---|
| 1 | 75.96 | 17.79 | 6.25 |
| 2 | 80.67 | 15.52 | 3.82 |
| 3 | 72.16 | 21.36 | 6.48 |
| Spectrum 2 | 79.26 | 16.22 | 4.52 |
| Spectrum 3 | 73.09 | 4.71 | 20.64 |

Figure 5.14: The results of the EDS analysis of the interdendritic regions of the as-cast Mg-2Ca-1Zn alloy, as-polished; all EDS results are in wt%.

Fig 5.15 (a and b) show the differences in the morphology of the phases in the homogenized alloy compared to the as-cast condition. As a result of homogenization the dendritic structure of α-Mg disappears and second phase particles, which are partly spherodized, are dispersed throughout the matrix. Optical images of the homogenized alloy in the as-polished state (c and d) also show the morphology of the phases as a result of homogenization.

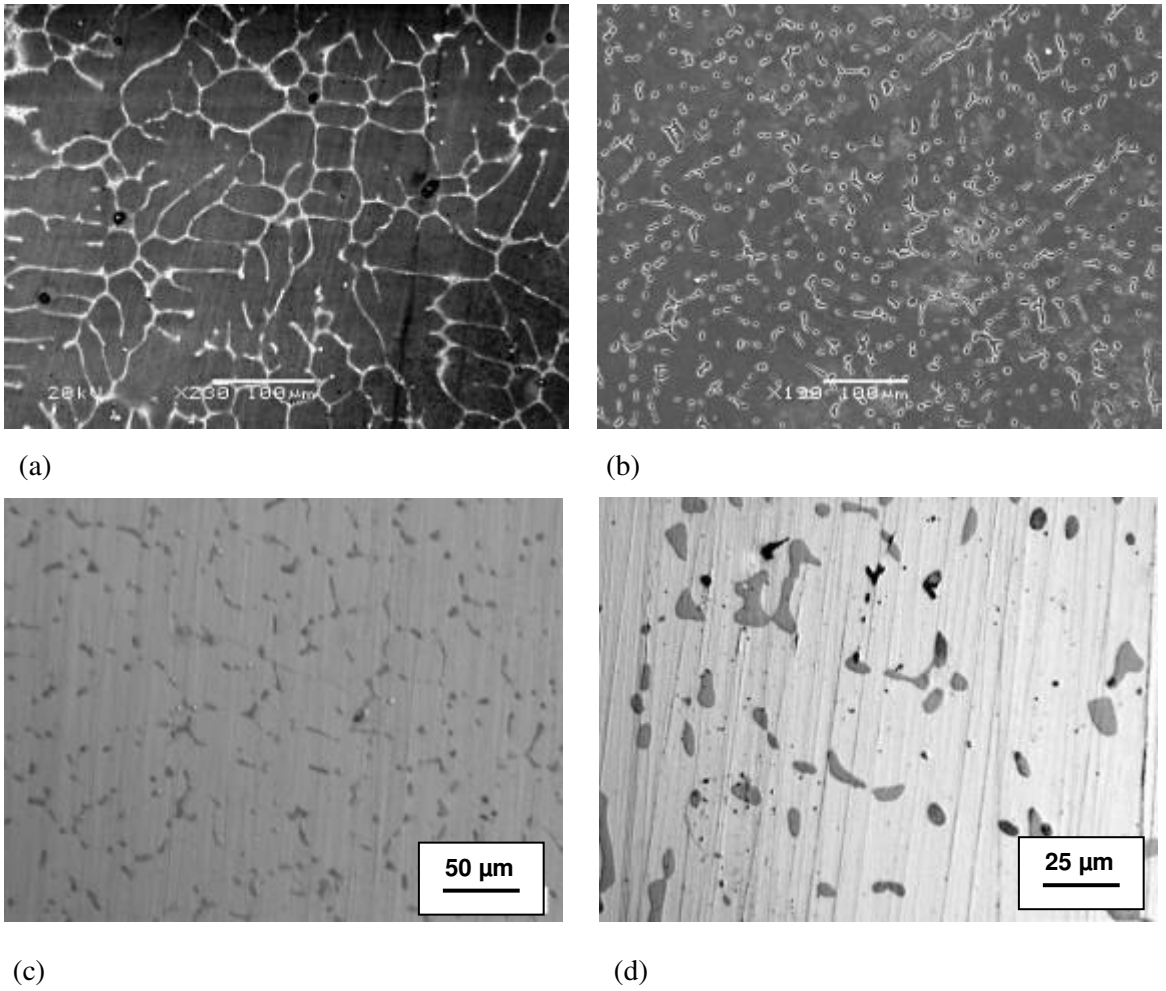


Figure 5.15: The comparison of the as-cast microstructure (a) with the homogenized microstructure (b, c, d). Sample etched in acetic glycol (b), and as-polished (a, c and d).

EDS analysis of the homogenized alloy, Fig 5.16, provides the concentration of calcium and zinc in the α-Mg grains and the presence of elliptical particles at the grain boundaries which are mainly rich in calcium, i.e. up to 28 wt%. The use of Nitric acid as etchant has revealed grain boundaries.

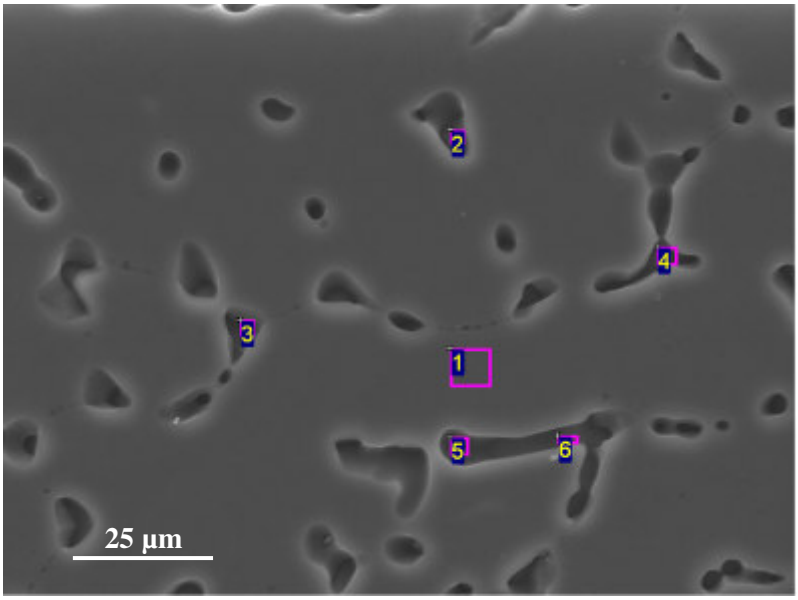


| Spectrum | Mg | Ca | Zn |
|---|---|---|---|
| 1 | 97.81 | 0.44 | 1.75 |
| 2 | 74.92 | 21.92 | 3.15 |
| 3 | 90.41 | 6.88 | 2.71 |
| 4 | 68.27 | 28.33 | 3.4 |
| 5 | 97.45 | 0.29 | 2.25 |
| 6 | 80.96 | 16.84 | 2.2 |

Figure 5.16: The result of the EDS analysis of homogenized Mg-2Ca-1Zn alloy etched with nitric acid (all results are in wt%).

### 5.3.2 Microstructural Evolution of the Mg-2Ca-1Zn Alloy during Aging

The microstructure of Mg-2Ca-1Zn aged for 6 hours at 175°C is shown in Fig 5.17. This micrograph shows second phase particles on triple junctions, marked by a black box, and on grain boundaries, similar in appearance to those found in the homogenized alloy. Presence of

smaller precipitate-like particles within α-Mg is also shown by an arrow. The EDS analysis yields results similar to the EDS results shown in Fig 5.16.

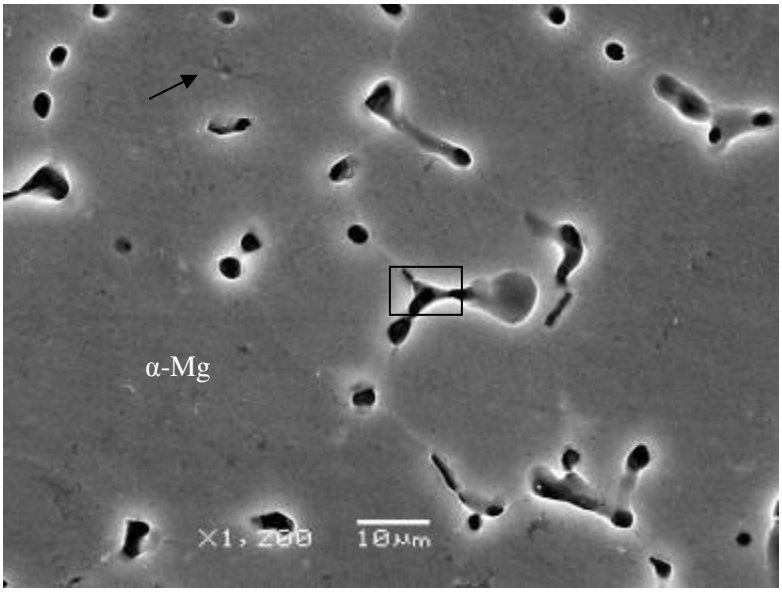


Figure 5.17: SEM micrograph of the Mg-2Ca-1Zn aged for 6 hours at 175°C, etched in acetic glycol.

### 5.3.3 Hardness Evolution of the Mg- 2Ca-1Zn Alloy during Isothermal Aging

Aging response of the Mg-2Ca-1Zn at 175°C, 200°C and 220°C is presented in this section. As Fig 5.18 shows, the as-cast hardness drops after homogenization. At 175°C and 200°C microhardness shows an increasing trend reaching a peak of approximately 70 VHN after 6 and 8 hours, respectively. Considering the hardness of the homogenized sample, i.e. 55 VHN, the hardness increase due to aging at the above temperatures is 26%. After reaching the peak hardness, the hardness drops steadily falling to 62 and 52 VHN after 72 hours of aging at 175°C and 200°C, respectively. At 220°C, the time required to reach peak hardness is shortened to 0.5 hour compared to the 6 or 8 hours at 175°C and 200°C, while the peak

hardness value remains almost the same, i.e. 70 VHN. Although there is a decreasing trend in hardness after the peak hardness, there is a possible rise in hardness after 2 hours of aging. However, this might be due to the significant scatter in the data. Hardness then reaches the lower value of 62 VHN after 28 hours of aging.

As in the case of the binary alloy, the significant scatter in the entire aging data prevents to create smooth aging curves with clear under-aged, peak-aged and over-aged regimes. In order to solve this problem, representative hardness points of each data series are selected for each temperature. This allows that approximate aging curves are created. The resultant aging curves are shown in Fig 5.19. Aging curves at 175°C and 200°C show a similar trend in the increase of hardness up to the first hour of aging. The hardness curve for 200°C shows a steeper slope up to the maximum hardness, i.e. peak- aged condition. Peak-aged condition at 175°C and 200°C is likely 6 and 10 hours, respectively. The decrease in hardness after peak-aged condition, i.e. overaging, is seen in all three isothermal aging temperatures. Decrease in hardness in the over-aged regime at 200°C is faster compared to the one in the 175°C. At 220°C, time to the peak-aged condition is drastically shortened to 0.5 hour.

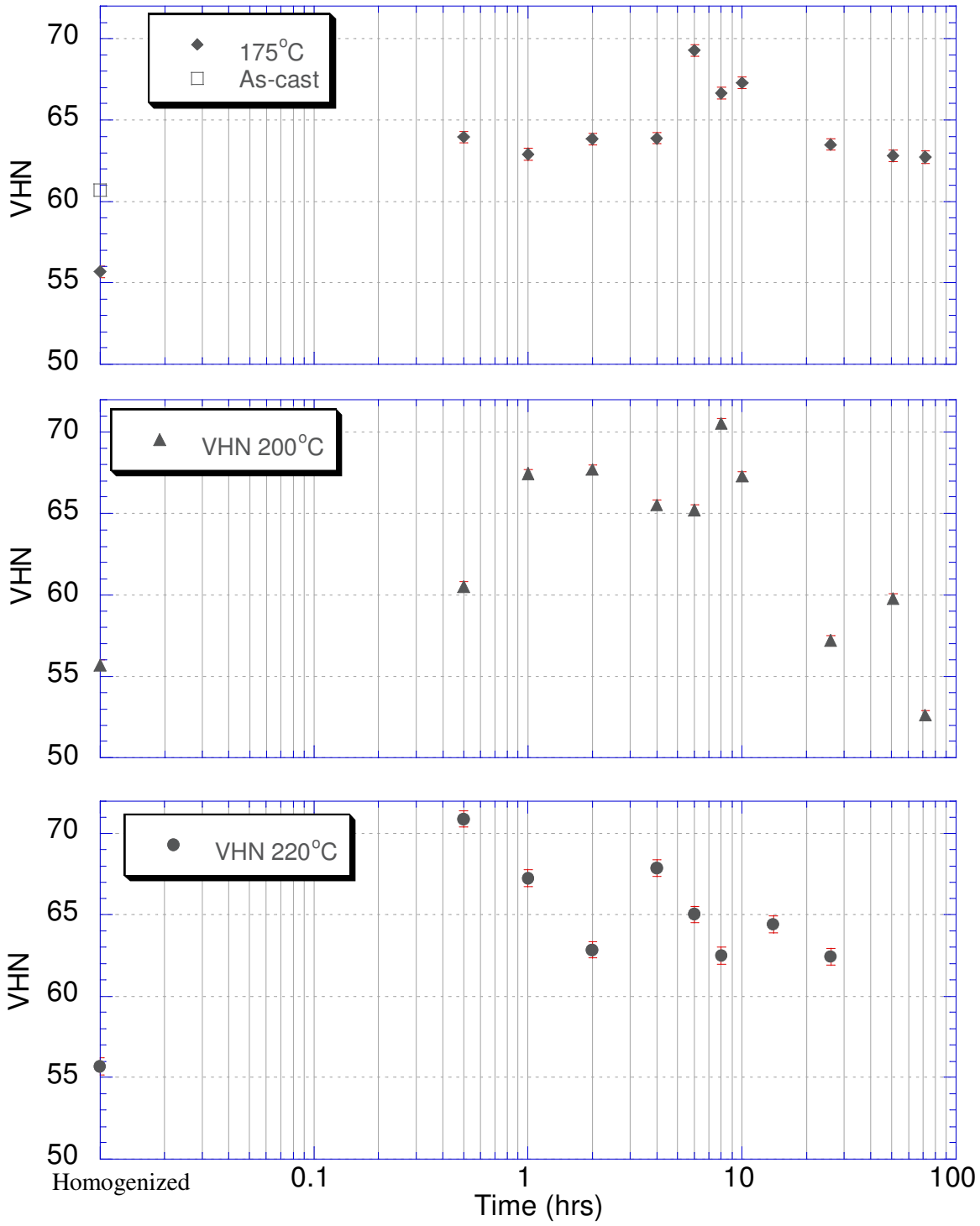


Figure 5.18: Microhardness evolution of the as-cast and homogenized Mg-2Ca-1Zn during isothermal aging at 175°C, 200°C and 220°C.

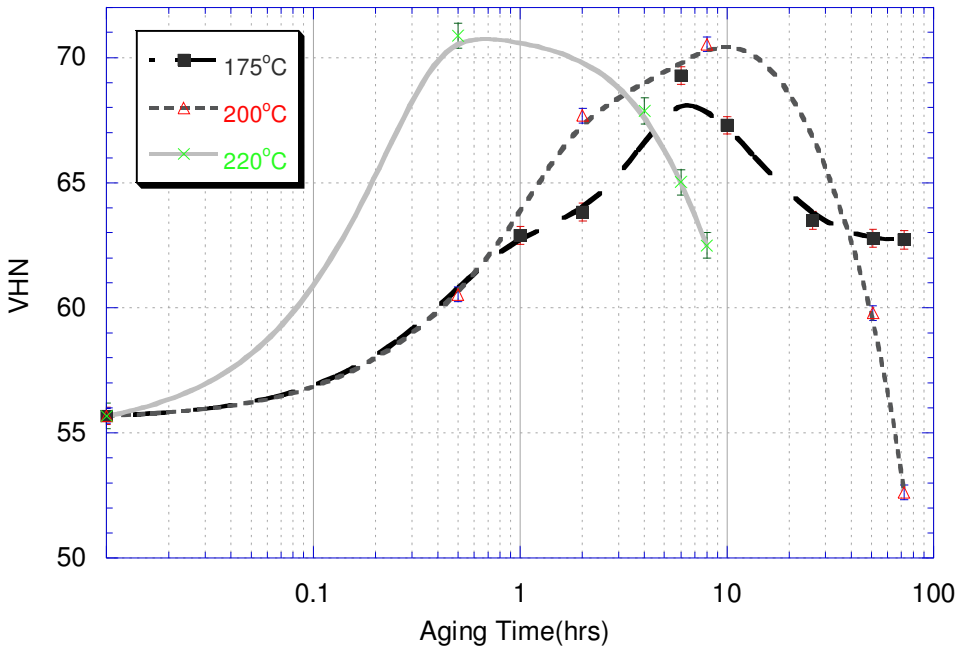


Figure 5.19: Isothermal aging curves of the homogenized Mg-2Ca-1Zn at 175°C, 200°C and 220°C.

### 5.3.4 IC Results

IC traces of homogenized Mg-2Ca-1Zn are shown in Fig 5.20. In order to show the important details of the IC traces only first two hours are presented. As shown in Fig 5.20, the IC trace of 220°C shows the highest peak of heat release at 0.021 W/g with the steepest decaying slope after reaching the peak. IC trace of 200°C shows the maximum heat flow as 0.011 W/g which is followed by decrease in heat flow to 0.001 W/g. At this point, heat flow flattens and finally starts approaching to the zero heat flow line. Details of IC traces for the first 0.5 hour are shown in Fig 5.21.a. Considering small heat effects in the trace of 175°C, details of this trace traces is depicted in Fig 5.21.b.

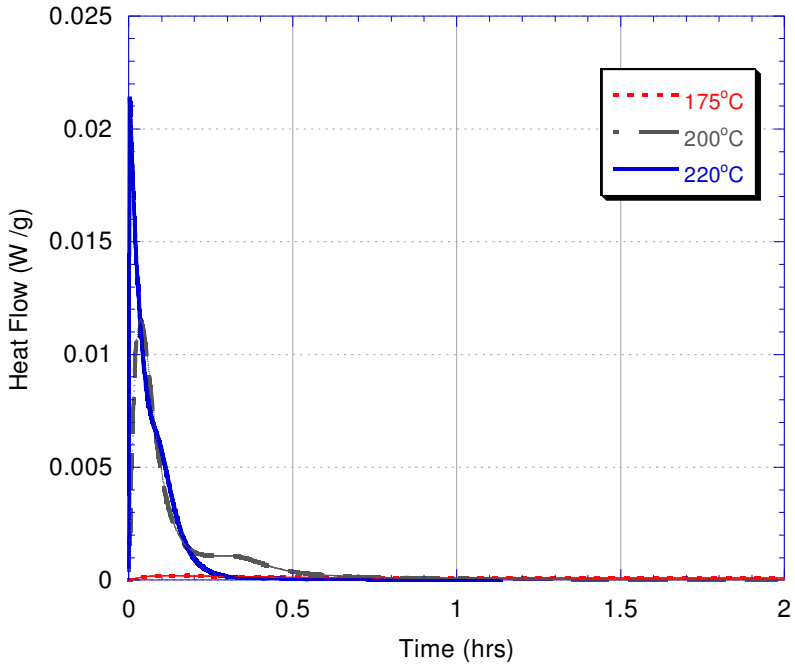


Figure 5.20: The isothermal calorimetry traces for homogenized Mg-2Ca-1Zn samples during aging at 175°C to 220°C.

As Fig 5.21.a shows at 220°C the maximum heat flow is reached in a shorter time compared to the one at 200°C. After the initial increase of heat flow to the maximum value, the heat flow drops. In addition, presence of a shoulder shown by an arrow in the trace of 220°C is noticeable. At 200°C after 0.2 hours, flattening in heat flow is noticeable. As shown in Fig 5.21.b, the IC trace of 175°C shows the initial increase in heat flow to the maximum 0.0002 W/g. Heat flow then drops and a pronounced flattening in the trace after 40 minutes is observed. The trace then finally starts approaching to the zero heat flow line.

a)

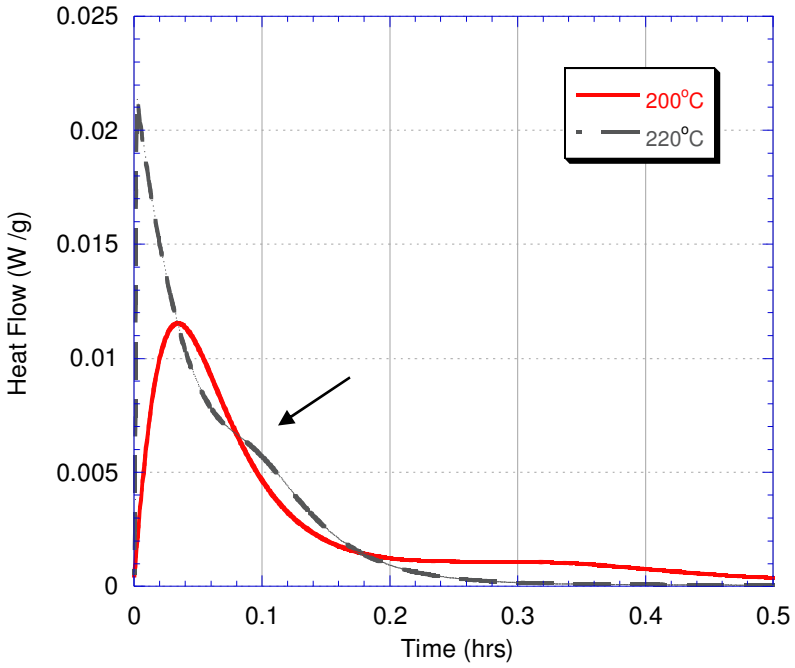


b)

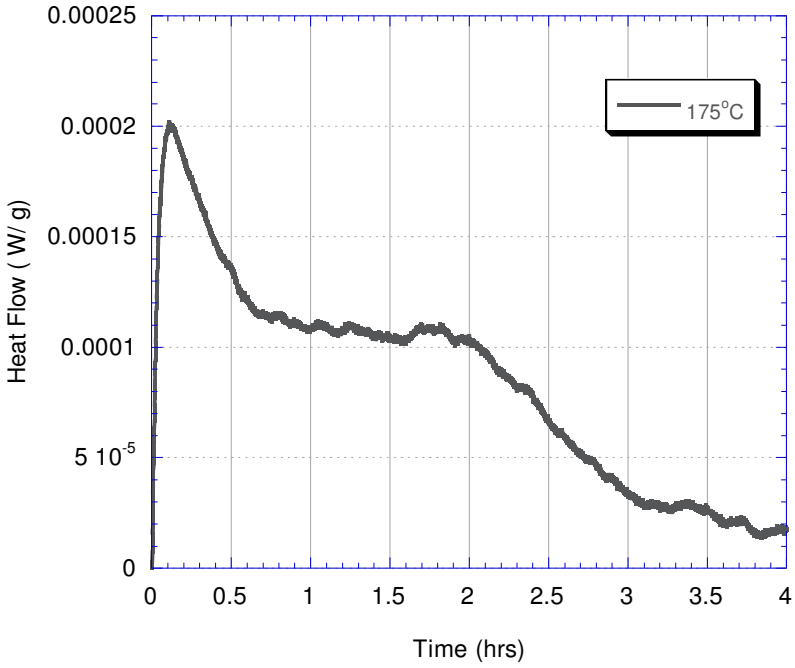


Figure 5.21: Details of isothermal calorimetry traces of homogenized Mg-2Ca-1Zn at 200°C and 220°C (a) and 175°C (b).

Total heat flow, i.e. total area under the IC trace, and $t_f$ are given in Table 5.2. As this table shows increasing aging temperature from 175°C to 200°C increases the amount of heat evolved but decreases $t_f$. However, by increasing aging temperature from 200°C to 220°C amount of the evolved heat drops though $t_f$ is significantly shortened compared to the both traces at 175°C and 200°C. It should be stressed that there may be an error associated with determining $t_f$ as the upper limit of the $\int_0^{t_f}\left(\frac{dQ}{dt}\right)dt$ which gives the total area under the IC trace as the total evolved heat. This might result in underestimation of the total heat evolved at IC trace of 220°C.

Table 5.2: The values obtained for $t_f$ and the total heat evolved during isothermal calorimetry of the homogenized Mg-2Ca-1Zn alloy at various temperatures.

| Aging Temperature (℃) | tf (hr) | Total Heat (J/g) |
|---|---|---|
| 175 | 8 | 1.29 |
| 200 | 6.59 | 5.26 |
| 220 | 1.11 | 5.04 |

### 5.3.5 DSC Results

The DSC trace of the homogenized alloy is shown in Fig 5.22. Two major exothermic peaks, I and II, at 113°C and 207°C, respectively, and two troughs at 168°C and 284°C, i.e. III and IV, are identified. Peak II is a narrower event compared to peak I. Considering the zero heat flow line shown by the arrow in Fig 5.22, troughs III and IV are endothermic events.

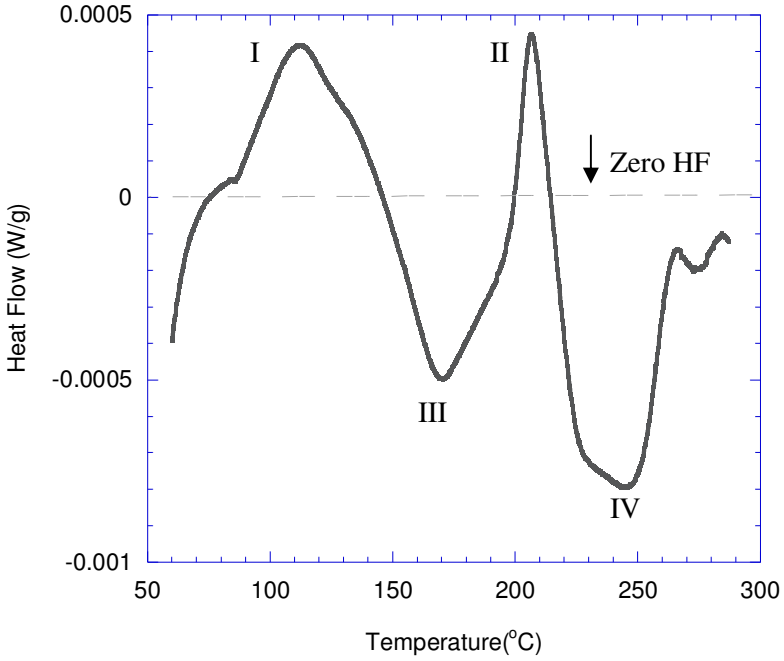


Figure 5.22: DSC trace of homogenized Mg-2Ca-1Zn from 30-300°C; heating rate 1°C/min.

### 5.3.6 Hardness Evolution during non-isothermal Aging

Fig 5.23 shows the evolution of hardness with aging temperature. Aging of a homogenized sample with heating rate of 1°C/min from 60°C up to 230°C results in a steady increase in hardness from 53 to 68 VHN. After reaching peak hardness at 230°C, further aging up to 250°C results in drop in hardness to value of 65 VHN.

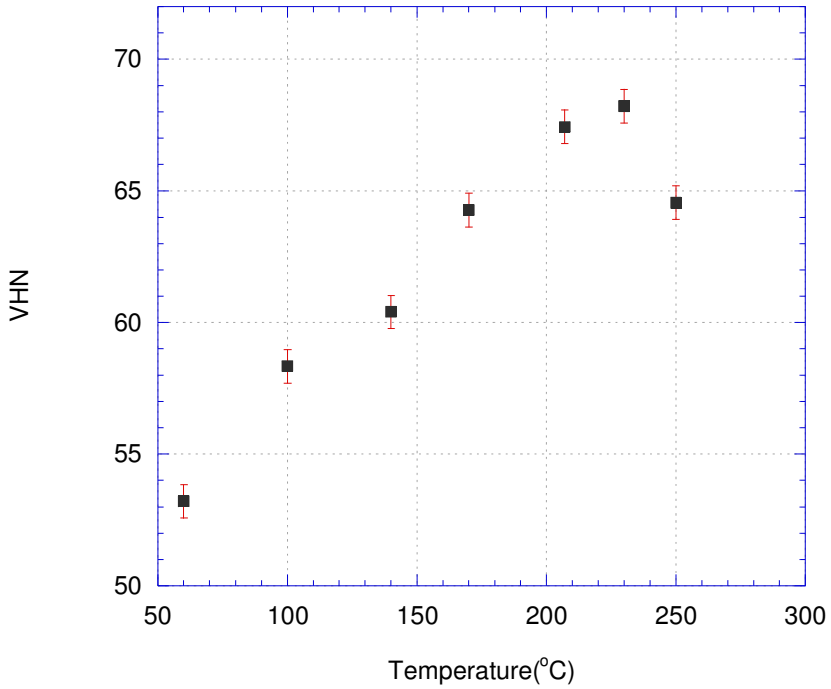


Figure 5.23: Hardness evolution in homogenized samples heated with heating rate of 1°C/min to 250°C.

### 5.3.7 XRD Analysis of Mg-2Ca-1Zn Alloy

XRD analysis on the as-cast alloy, Fig 5.24, shows presence of α-Mg, $Mg_2Ca$, and the ternary phases $Ca_2Mg_6Zn_3$ and $CaCu_{0.8}Zn_{0.2}$. Some peaks are contributions of more than one phase. The most intense peaks belong to magnesium.

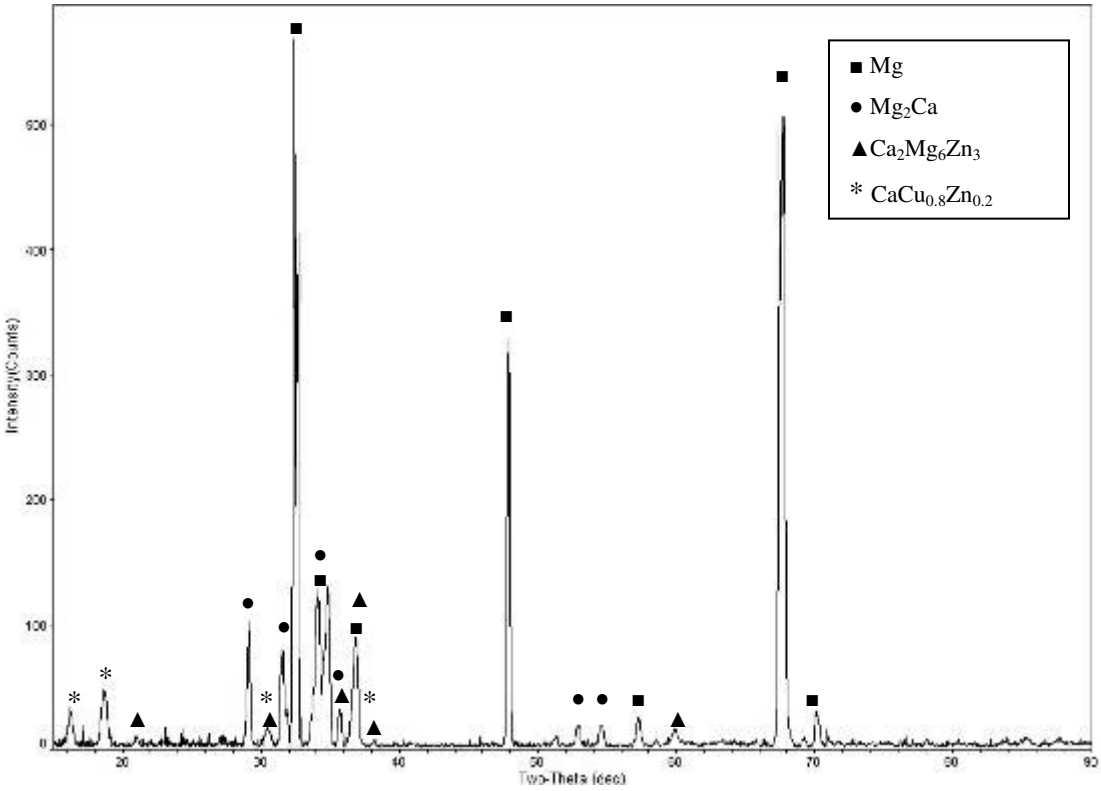


Figure 5.24: XRD spectrum of the as-cast Mg-2Ca-1Zn.

## 5.4 Evolution of the Microstructural Characteristics and Hardness during Homogenization and Aging- Mg-2Ca-2Zn Alloy

Experimental results on microstructural evolution during homogenization and precipitation hardening response of the Mg-2Ca-2Zn alloy will be presented in this section.

### 5.4.1 Microstructural Evolution of the Mg-2Ca-2Zn Alloy during Homogenization

Fig 5.25 shows optical micrographs of Mg-2Ca-2Zn alloy in the as-cast condition. Dendritic solidification of the alloy can be seen in the Fig 5.25 (a and c) while Fig 5.25.b shows a high magnification optical micrograph of the interdendritic regions. It appears that

the interdendritic region consists of more than one phase, as shown by the arrows on Fig. 5.25.b. The presence of triple junctions (shown by the black box) is noticeable in the interdendritic regions.

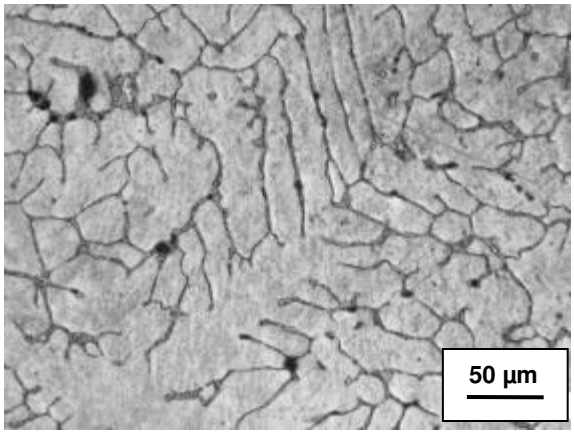


(a)

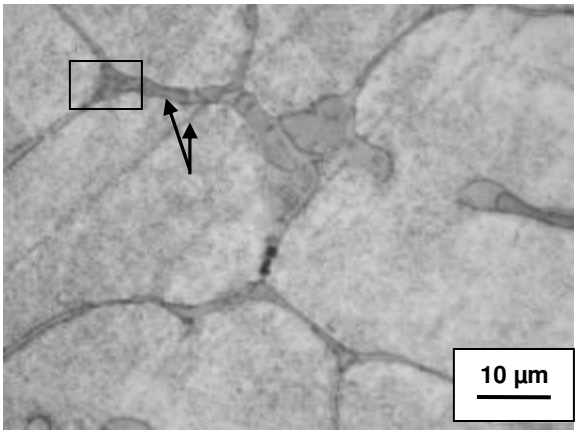


(b)

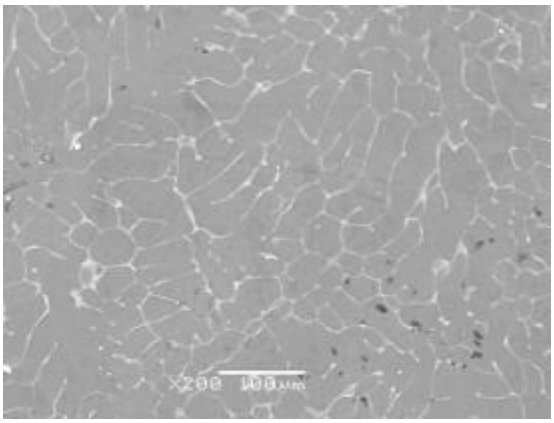

(c)

Figure 5.25: Optical micrographs of the as-cast Mg-2Ca-2Zn alloy (a and b) and SEM micrograph of the as-cast alloy, (c), all as-polished.

Microstructural evolution as a result of homogenization heat treatment is shown in the optical micrographs of the as-cast, Fig 5.26.a and homogenized alloy Fig 5.26.b. The dendritic microstructure disappears and mostly spherodized second phase particles form within the α-Mg matrix. The formation of a different phase on the larger grayish phase is also a noticeable feature of Fig 5.26.b.

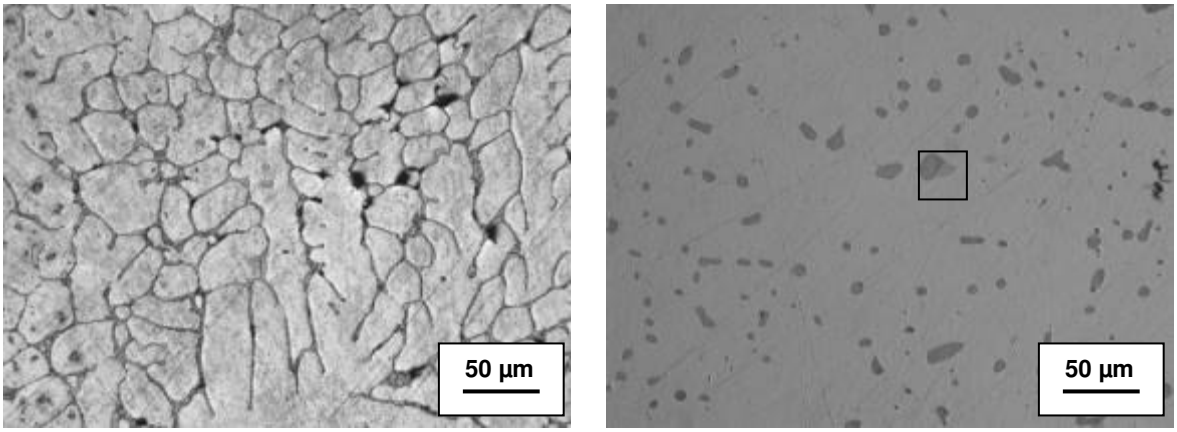


Figure 5.26: Microstructure of as-cast Mg-2Ca- 2Zn alloy (a) and homogenized microstructure (b). Both images from as-polished samples.

The EDS analysis results from the as-cast and homogenized Mg-2Ca-2Zn are shown in Fig 5.27.a and Fig 5.27.b, respectively. Figure 5.27.a shows the chemical composition of the interdendritic phases as well as that of the α-Mg matrix. It appears that the interdendritic region is rich in calcium and zinc, while the α-Mg matrix contains above 1 wt% zinc, i.e. significant compared to the calcium level. Fig 5.27.b provides the elemental concentrations in the homogenized alloy. The spherodized second phase particles are rich in calcium and contain zinc. The grain boundary/triple junction area is highly rich in zinc, while it also

contains significant amount of calcium. Spectrum 2 in Fig 5.27.b shows evidence for the presence of zinc, approximately 3 wt%, in the homogenized α-Mg matrix, as well.

(a)

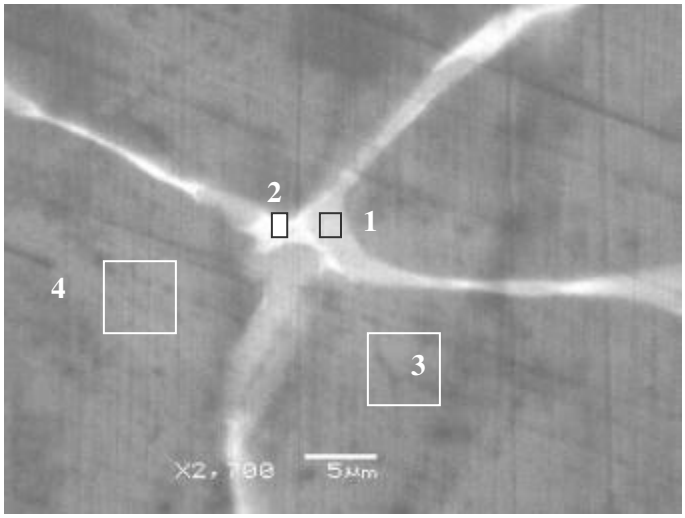


| Spectrum | Mg | Ca | Zn |
|---|---|---|---|
| 1 | 60.36 | 20.69 | 18.95 |
| 2 | 62.07 | 11.74 | 26.19 |
| 3 | 98.03 | 0.42 | 1.55 |
| 4 | 97.1 | 0.25 | 2.65 |

(b)

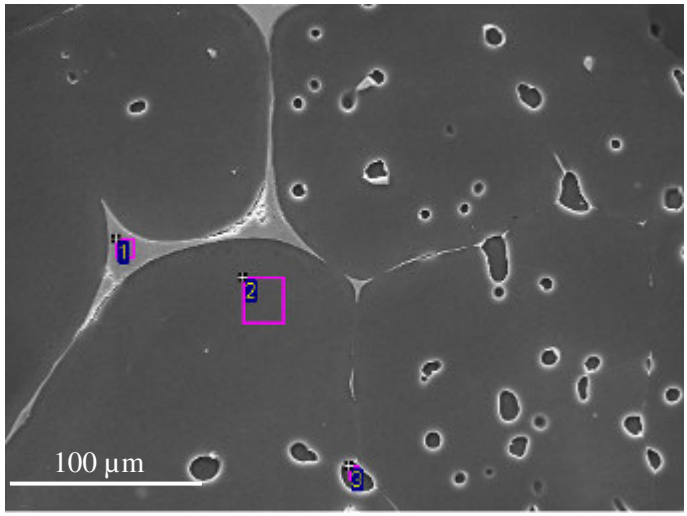


| Spectrum | O | Mg | Ca | Cu | Zn |
|---|---|---|---|---|---|
| 1 | 2.07 | 52.59 | 12.18 | 1.00 | 32.16 |
| 2 | 0.90 | 96.21 | | | 2.89 |
| 3 | 3.50 | 54.33 | 35.50 | | 6.68 |

Figure 5.27: EDS analysis of as-cast Mg-2Ca-2Zn in as polished condition (a) and homogenized alloy etched in acetic glycol (b); all results are in wt%.

### 5.4.2 Microstructural Evolution of the Mg- 2Ca- 2Zn Alloy during Aging

Microstructural characteristics of the aged Mg-2Ca-2Zn are shown in Fig 5.28. An optical image of the aged sample shows microstructural features similar to the homogenized sample, i.e. Fig 5.26.b, with mostly spherodized second phase particles within the α-Mg matrix. The EDS analysis on the second phase particles included in the white box in Fig 5.28.b shows that these small particles contain zinc (over 3 wt%). Spectrum 3 of Fig 5.28.c reveals that the white area adjacent to the spherodized particles is rich in zinc, while it may also contain the impurity element copper. This zinc-rich phase also contains significant calcium, e.g. ~ 7 wt%, for the phase examined in Fig 5.28.c.

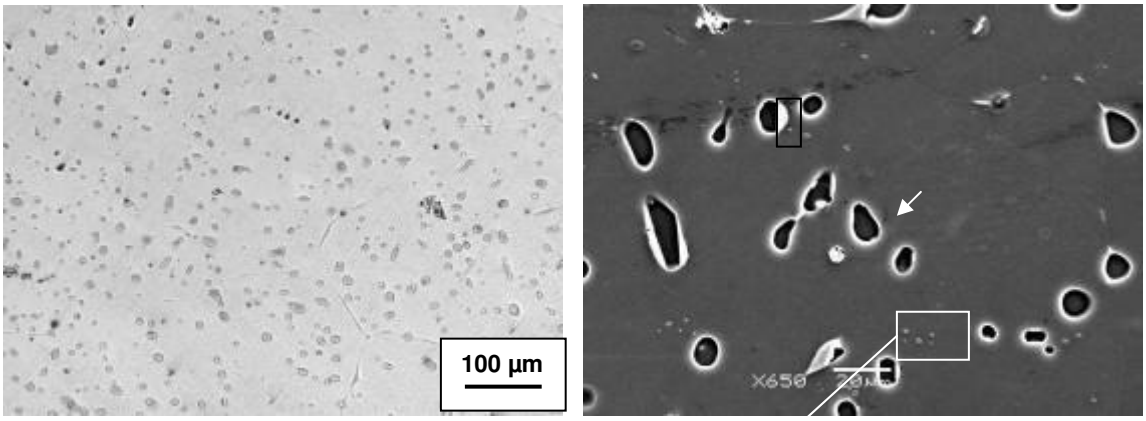


(a) (b)

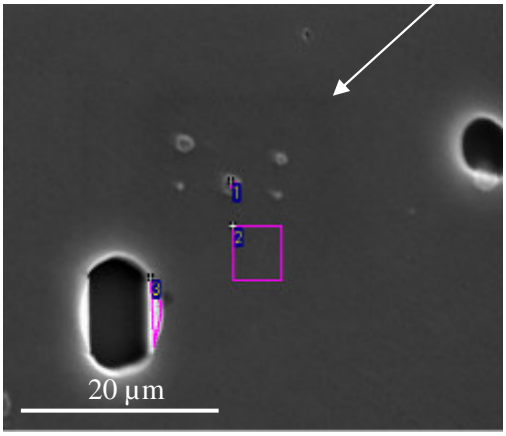


| Spectrum | Mg | Ca | Cu | Zn |
|---|---|---|---|---|
| 1 | 96 | 0.39 | | 3.61 |
| 2 | 96.19 | 0.27 | | 3.54 |
| 3 | 66.44 | 6.92 | 1.4 | 25.24 |

(c)

Figure 5.28: Optical micrograph of Mg-2Ca-2Zn alloy aged for 6 hours at 175°C (a), SEM micrographs of the alloy with the same heat treatment history etched with acetic glycol (b and c), all results are in wt%.

### 5.4.3 Hardness Evolution of the Mg- 2Ca- 2Zn Alloy during Isothermal Aging

The aging response of Mg-2Ca-2Zn at 175°C, 200°C and 220°C is presented in this section. As Fig 5.29 shows, after homogenization, the as-cast hardness of 60 VHN drops to 57 VHN. At 175°C, hardness increases with aging time reaching a peak of approximately 69 VHN after ten hours which is then followed by a declining trend in hardness up to 50 hours. At 200°C, the hardness increases from 57 VHN for the homogenized condition to 67 VHN after two hours of aging. This hardness level does not show any significant decrease when aging time is increased up to 8 hours. The hardness finally declines to approximately 62 VHN after 18 hours of aging at 200°C. At 220°C, the hardness shows a sharp increase in the first hour of aging, reaching the peak value of 70 VHN after 1 hour. Subsequently, the hardness decreases to a 60 VHN after ten hours of aging. The hardness values for aging at 220°C show significant scatter in the over-aged regime. Due to this scatter and as in the case of the previous two alloys, representative hardness points of each aging curve are selected to create approximate aging curves for better comparison purposes. These curves are demonstrated in Fig 5.30. These aging curves can be used to determine the approximate peak-aged condition for each temperature. Fig 5.30 demonstrates the effect of aging temperature on the time to reach the peak-aged condition and the evidence for the significant decrease in this time when the temperature is increased from 175°C to 220°C.

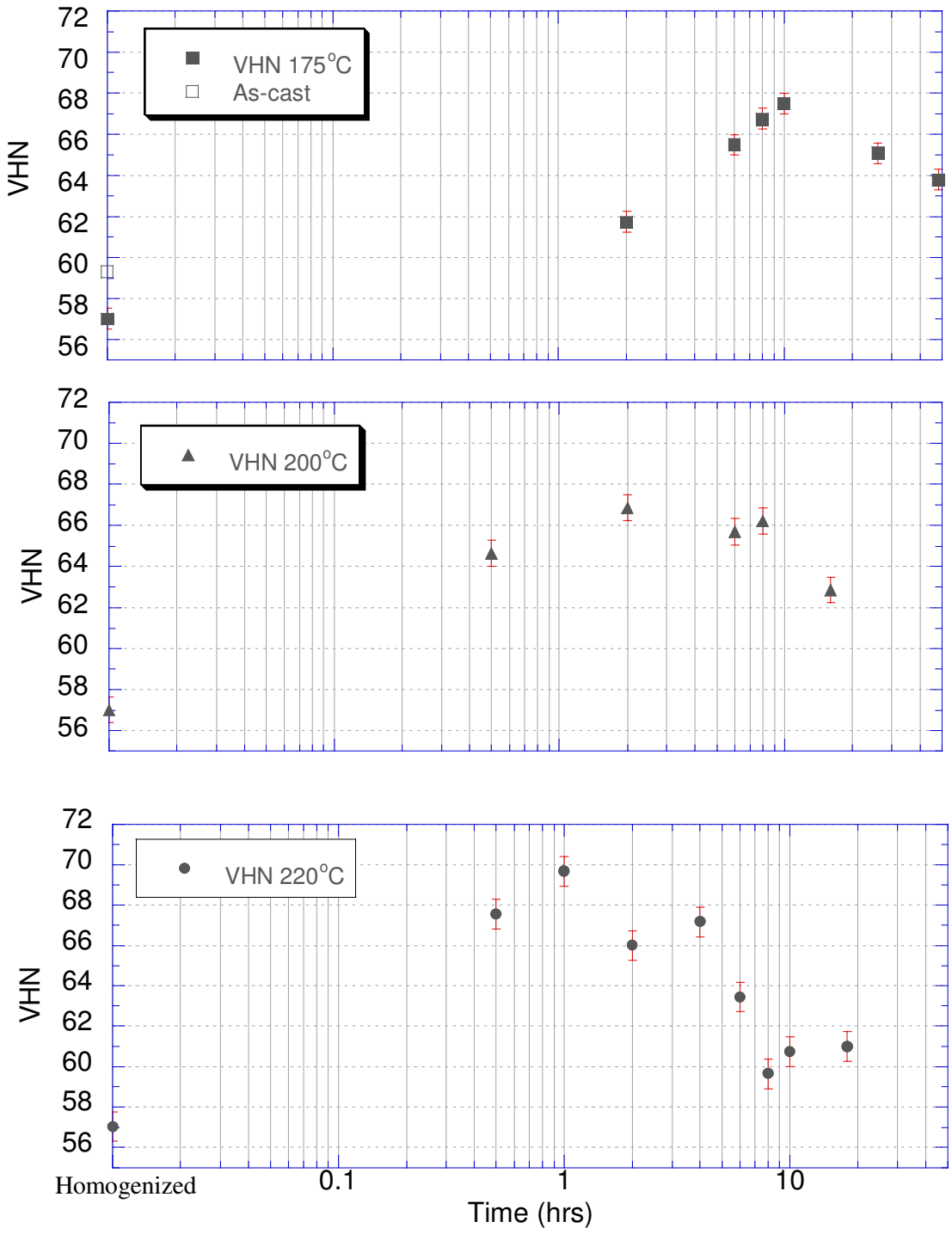


Figure 5.29: Microhardness evolution of homogenized Mg-2Ca- 2Zn during isothermal aging at 175°C, 200 °C and 220 °C.

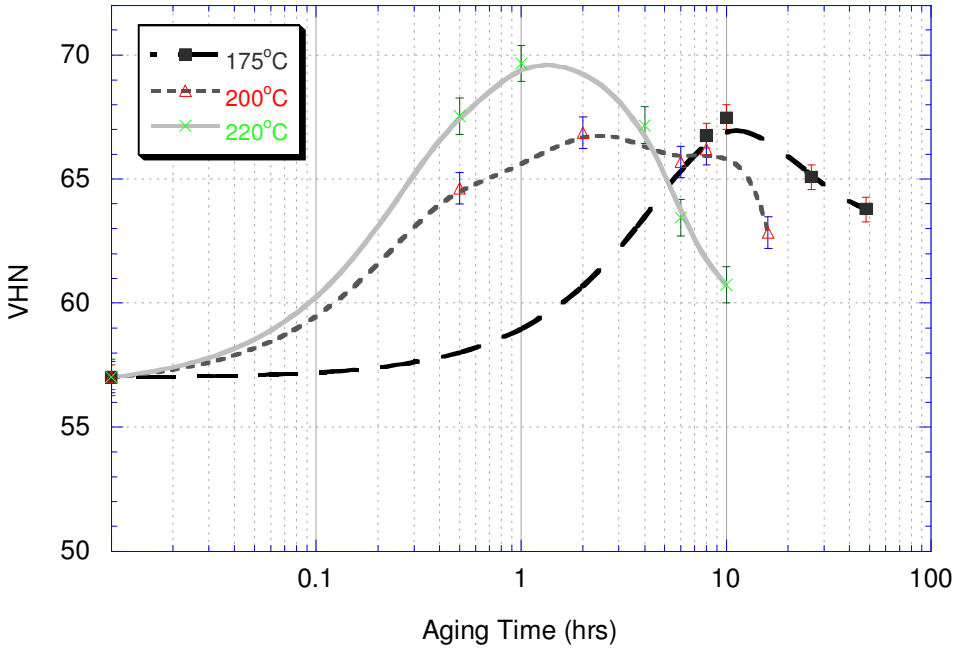


Figure 5.30: Isothermal aging curves of the homogenized Mg-2Ca-2Zn at 175°C, 200°C and 220°C.

### 5.4.4 IC Results

The IC traces of homogenized Mg-2Ca-2Zn alloy are shown in Fig 5.31. For better clarity, the IC traces up to the first two hours of aging are presented. As shown in the Fig 5.31, the IC trace of 220°C shows the highest peak of a heat release as 0.033 (W/g) with the steepest decaying slope after reaching the peak. A small change in decaying slope of the 220°C trace at 0.005 (W/g) heat flow is also noticeable. The trace for aging at 200°C shows peak of 0.012 (W/g) which then drops to 0.001 (W/g) where it flattens and finally starts approaching the zero heat flow as time increases. The traces of aging processes at 200°C, 220°C and 175°C are shown in the Figs 5.33.a and b for further illustration of the details.

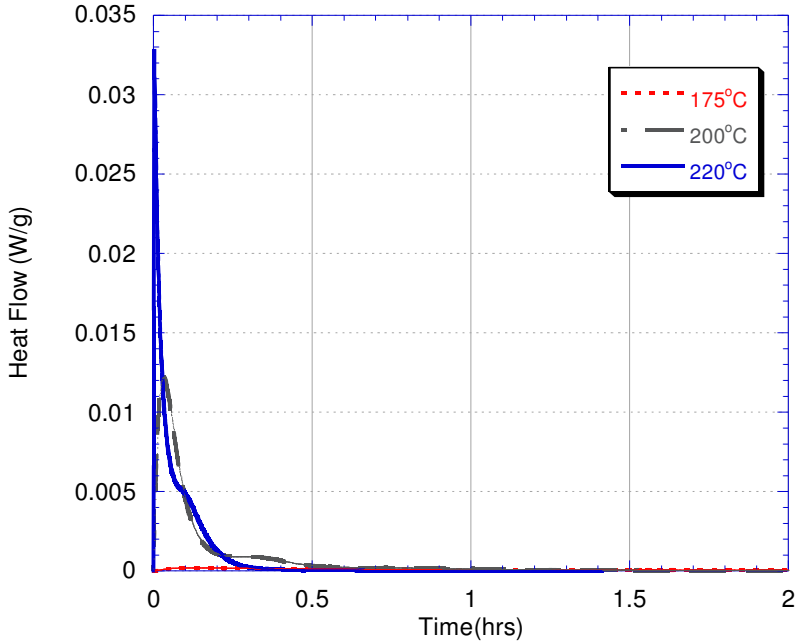


Figure 5.31: The isothermal calorimetry traces for homogenized Mg-2Ca-2Zn samples during aging at 175 °C to 220 °C.

Fig 5.32.a shows IC traces at 200°C and 220°C in the first 30 minutes while (b) is intended to give details of the 175°C IC trace for the first four hours. As Fig 5.32.a shows the flattening in the trace of 200°C starts at 0.001 (W/g) and it continues for about 0.2 hrs, i.e. 12 min, and then starts falling to the zero heat flow. For the trace of 220°C, a sharp declining slope after the peak of 0.033 (W/g) to 0.006 (W/g) is seen. The trace demonstrates the presence of a shoulder similar to the case of the Mg-2Ca-1Zn alloy aged at 220°C. As in Fig 5.32.b, trace of 175°C, shows the peak of 0.0002 (W/g) followed by a steady decline in the heat flow. This trace illustrates a plateau region at the approximate heat flow of 0.00007 (W/g) and in the time range of 1.5 to 2.5 hours. The heat flow declines to 0.000003 (W/g) after approximately 4 hours of aging.

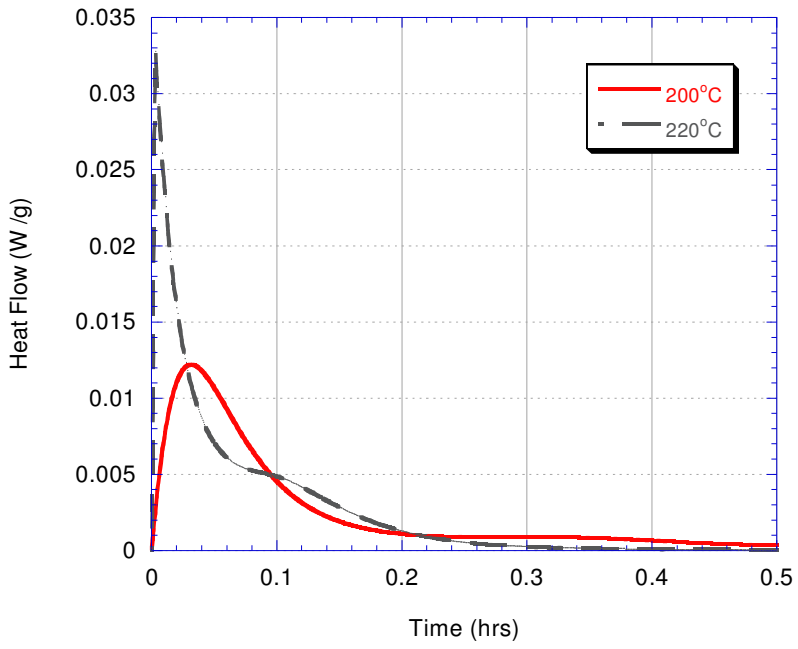


(a)

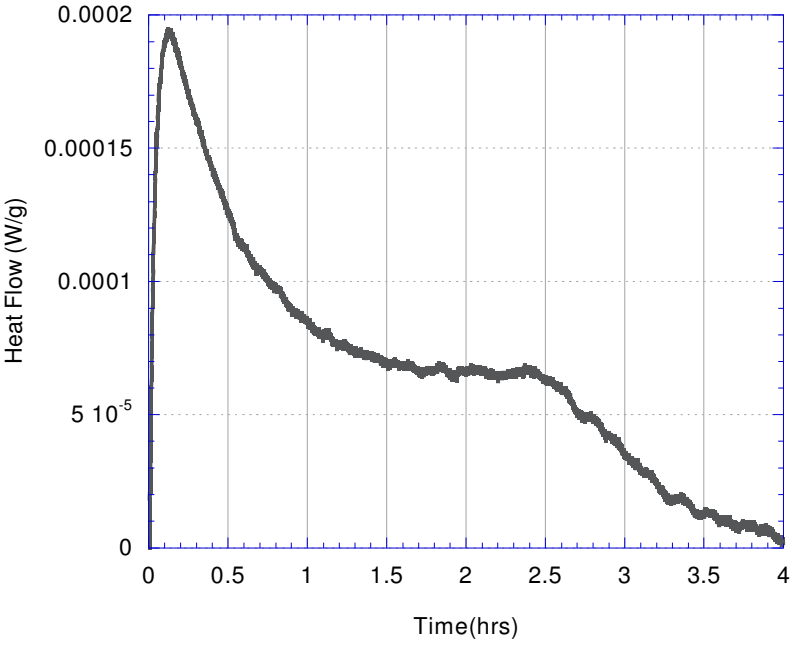


(b)

Figure 5.32: Isothermal calorimetry traces of homogenized Mg-2Ca-2Zn after 30 minutes at 200°C and 220°C (a) and 4 hours at 175°C (b).

The total heat flow and $t_f$ values are given in Table 5.3. As this table shows increasing aging temperature from 175°C to 200°C increases the amount of heat evolved but decreases $t_f$. However, by increasing aging temperature from 200°C to 220°C amount of the evolved heat drops, though $t_f$ is significantly shortened compared to both traces at 175°C and 200°C. It should be stressed that there may be an error associated with determining $t_f$ as the upper limit of the $\int_0^{t_f}\left(\frac{dQ}{dt}\right)dt$ which gives the total area under the IC trace as the total evolved heat. This might result in underestimation of the total heat evolved at IC trace of 220°C.

Table 5.3: The values obtained for $t_f$ and the total heat evolved during the isothermal calorimetry of the homogenized Mg-2Ca-2Zn at various temperatures.

| Aging Temperature (°C) | tf (hrs) | Total Heat (J/g) |
|---|---|---|
| 175 | 9.7 | 0.95 |
| 200 | 6.8 | 5.42 |
| 220 | 1.41 | 5.17 |

### 5.4.5 DSC Results

The DSC trace for the homogenized Mg-2Ca-2Zn alloy sample is shown in the Fig 5.33. Four exothermic peaks can be seen in the trace, i.e. I at 110°C, II at 210°C, III at 220°C and a large exothermic event at 285°C. In a general trend, height of exothermic events increases from I to IV, i.e. from 0.0004 (W/g) at the peak I to 0.001 (W/g) at the peak IV, while peak III is overlapped by peak II. Peak II seems to have another overlapping exothermic effect in the range of 180°C to 200°C. Two troughs, i.e. V and VI centered at 165°C and 260°C, respectively, are located below the zero heat flow line, indicating endothermic events.

Trough VI corresponds to the more negative value compared to the trough V, i.e. -0.0003 (W/g) at the trough VI compared to -0.00025 at the trough V (W/g).

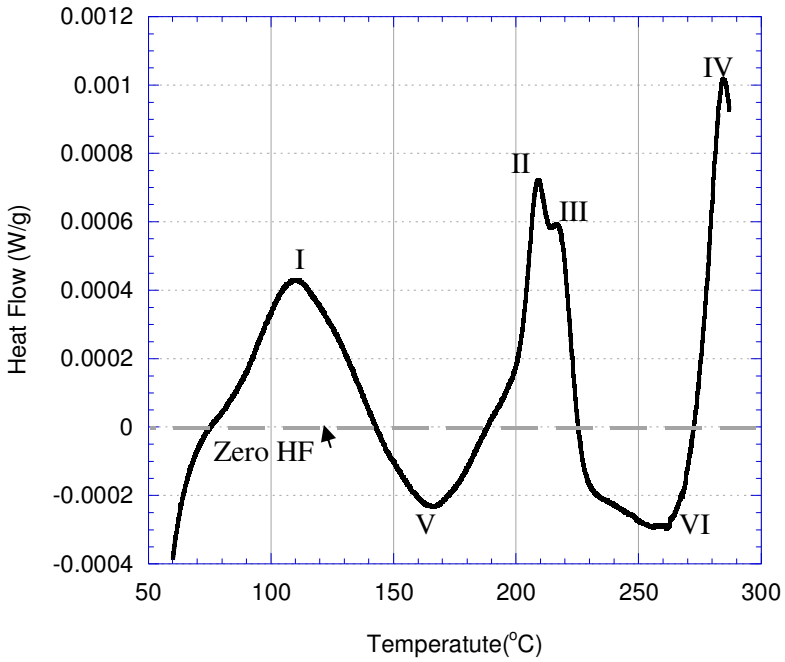


Figure 5.33: DSC trace of the homogenized Mg-2Ca-2Zn alloy from 30°C -300°C; heating rate of 1°C/min.

### 5.4.6 Hardness Evolution during non-isothermal Aging

The evolution of microhardness for homogenized samples of the ternary alloy with a heating rate of 1°C/min is plotted in Fig 5.34. The microhardness does not show a major increase in hardness in the temperature range of 60-140°C. As the temperature increases up to 190°C, the hardness demonstrates a slight increase reaching a value of 60 VHN. At 200°C, however, the hardness shows a steep rise to a value 67 VHN. Although hardness drops at 207°C to 61 VHN, hardness rises with increasing temperature, reaching a peak of 70 VHN at 250°C, i.e. corresponding to 23% increase in hardness from the homogenized condition.

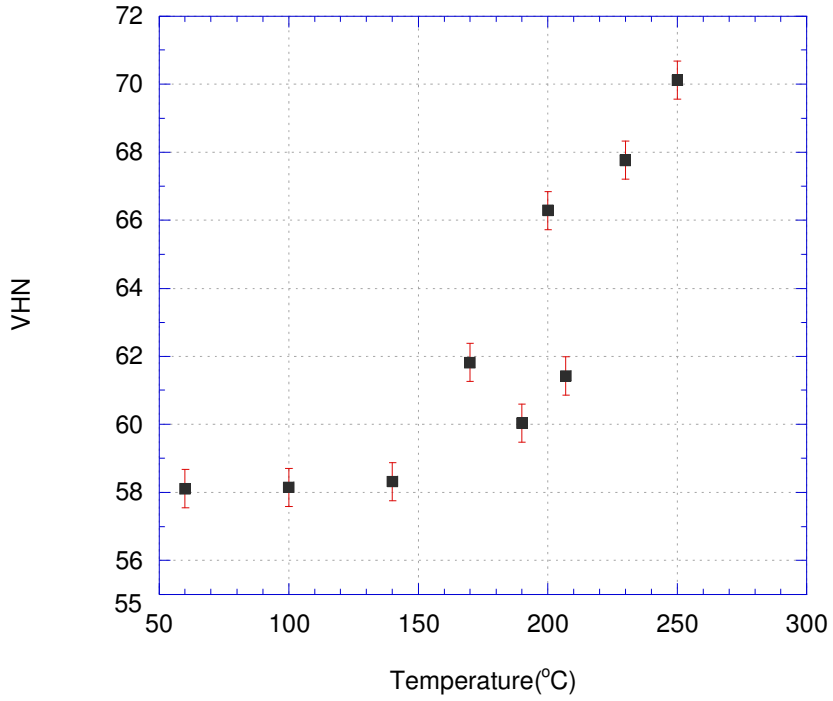


Figure 5.34: DSC trace of Mg-2Ca- 2Zn and corresponding hardness evolution in homogenized samples heated with heating rate of 1°C/min from 60°C to 250°C.

### 5.4.7 XRD Analysis of Mg-2Ca-2Zn

The XRD spectra of the as-cast and aged alloy for 6 hours at 175°C are shown in the Fig 5.35. The results show the presence of α-Mg, $Mg_2Ca$ and $Ca_2Mg_6Zn_3$ in the both conditions. The CaCu0.8Zn0.2 phase is also found in the as-cast condition. There is no report on this phase in the literature. However, EDS analysis has confirmed a presence of eutectic regions rich in copper, calcium and zinc, Fig 5.27.

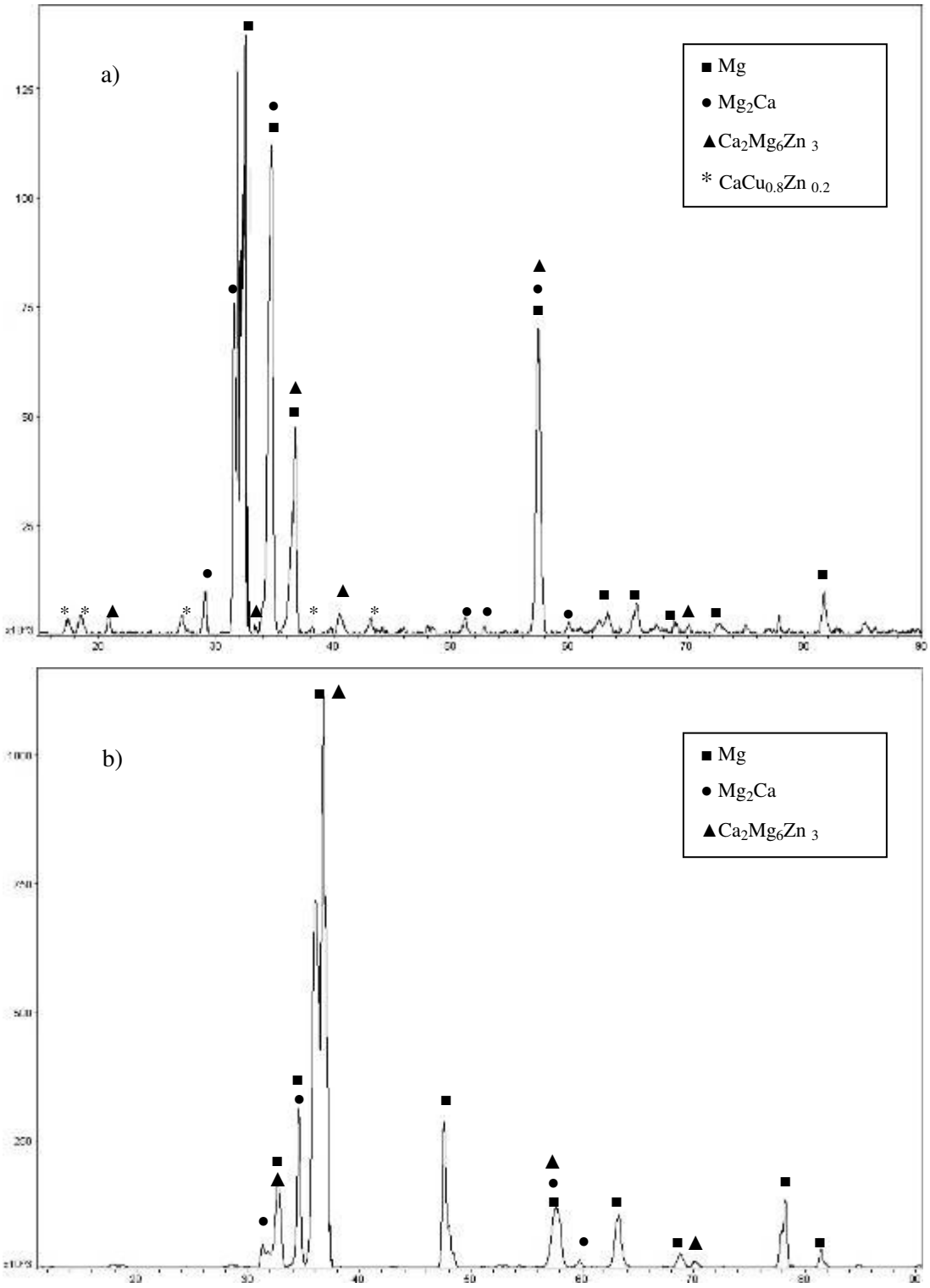


Figure 5.35: XRD spectra of Mg-2Ca- 2Zn, as-cast (a) and aged for 6 hours at 175°C (b).

### 5.4.8 Additional Information on the Effects of Etchants in Revealing Microstructrual Features of the Heat-Treated Samples

To wrap up experimental results chapter, a summary on the effects of two different etchants on revealing the microstructural features in Mg-2.5Ca and Mg-2Ca-2Zn as representative of the alloys of the present investigation will be presented. In the binary alloy, a duplex structure of α-Mg and large second phase particles of $Mg_2Ca$ are observed in the heat treated samples, both in the as-polished and etched conditions. Band-type features, however, are revealed by the nitric acid etching of the homogenized sample, Fig 5.36.

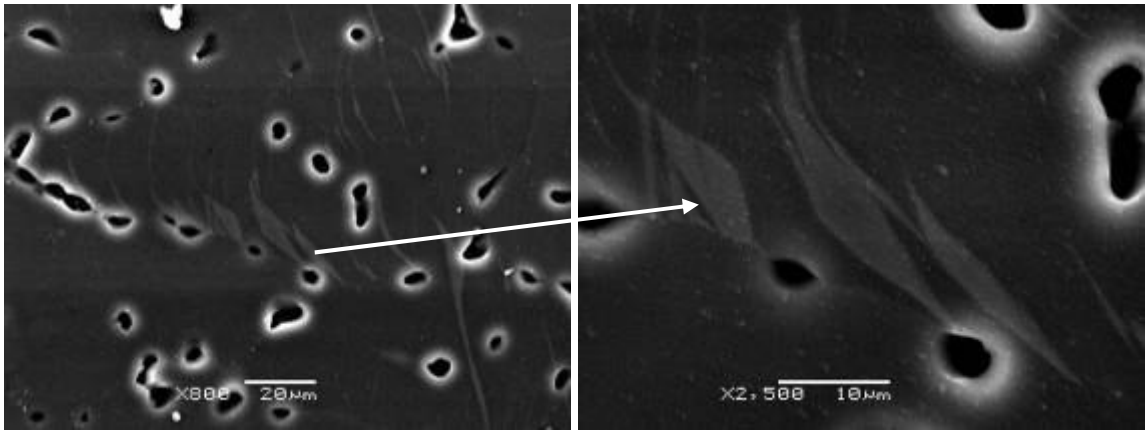


(a) (b)

Figure 5.36: SEM micrographs of band-type features in the homogenized Mg-2.5Ca (a and b) etched in nitric acid.

In the case of Mg-2Ca-2Zn alloy, in the as-polished condition, the presence of relatively large particles with a white phase formed on these particles, indicated by the arrow in (b), is noticeable. There are also smaller grayish particles. In micrographs of the sample etched in nitric acid, band-type structures within α-Mg grains are distinct microstructural features as a result of the etching condition. These band type structures are seen in all alloys etched by the

nitric acid. In the third series of microstructural results, etching with acetic glycol has resulted in revealing precipitates within α-Mg grains. Precipitate free zones (PFZ), in micrograph (f) are also revealed as a result of etching the sample with acetic glycol.

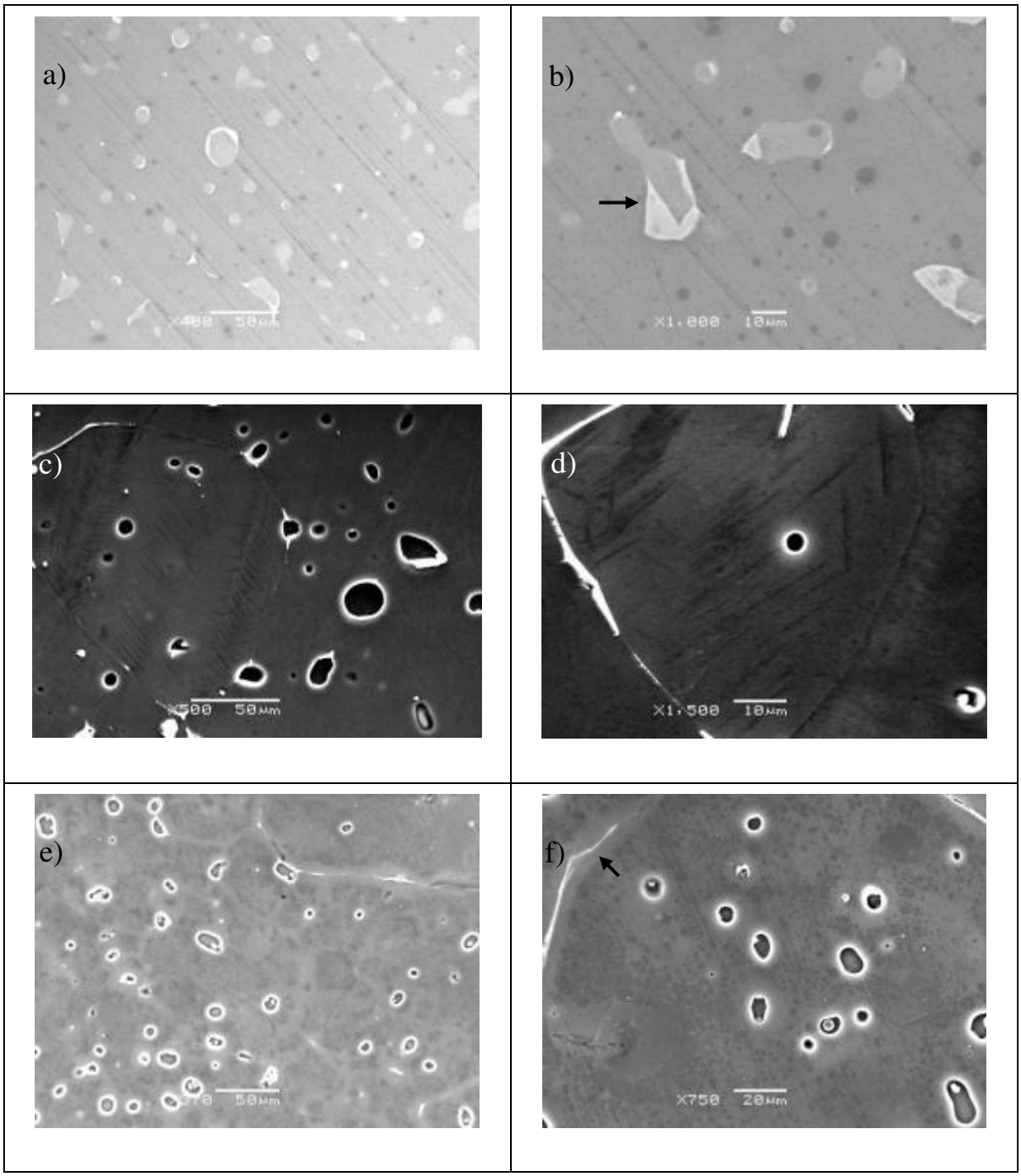


Figure 5.37: SEM micrographs of Mg-2Ca-2Zn aged for six hours at 175°C as-polished (a,b), etched in nitric acid (c,d) and etched in acetic glycol (e,f).

# Chapter 6
# Discussion

## 6.1 Introduction

Evolution of the microstructural features during homogenization and aging as well as precipitation hardening response of the alloys will be discussed in this chapter. Observed microstructures in the as-cast condition will be discussed based on the composition of the alloys and phase diagrams. Effects of alloy composition, time and temperature on the aging response of the alloys will also be discussed. Discussion on the applicability of the JMAK model to the isothermal calorimerty results and precipitation kinetics will wrap up this chapter.

## 6.2 As-Cast Microstructure

### 6.2.1 Binary Alloy

As Fig. 5.1 shows, the as-cast binary Mg-2.5Ca shows dendritic solidification of α-Mg and lamellar eutectic mixture within dendrites. The binary phase diagram for Mg-Ca, shown in Fig 6.1.a is the basis of the solidification route for the alloy. As temperature decreases, dendrites of primary magnesium, i.e. α-Mg, form and calcium is rejected to the melt. Upon enrichment of melt of calcium, at 516°C liquid containing 16.2 wt% Ca undergoes an invariant eutectic reaction:

$$L_{16.2wt\%Ca} \rightarrow \alpha(Mg)_{1.34wt\%Ca} + Mg_2Ca_{45wt\%Ca} \quad (6.1)$$

The EDS analysis confirms the average content of calcium within the eutectic mixture as 16 wt%. This is shown in Fig 5.4.a. The solidification process of this hypoeutectic alloy is schematically shown in Fig 6.2.b. Solidification, however, does not completely follow the phase diagram due to non-equilibrium solidification. The concentration of calcium in the α-Mg dendrites will be less than what is expected from the phase diagram. EDS data from Fig 5.4.a can be used as a rough estimate for the calcium content of the magnesium matrix in the as-cast condition. Thus the calcium content can be assumed to be as low as 0.5 wt% in the as-cast condition.

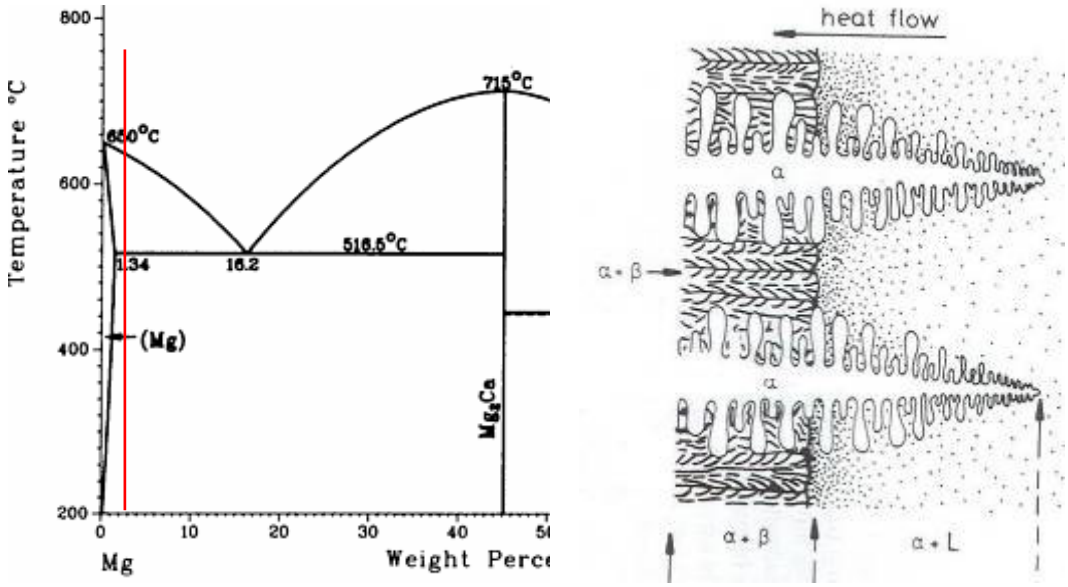


(a) (b)

Figure 6.1: Mg-Ca binary phase diagram (a) and schematics of hypoeutectic alloy solidification (b) [a from Clark and Hashemi 1988, b from Porter and Easterling 1992].

### 6.2.2 Ternary Alloys

Similar to the binary alloy, solidification of the ternary system starts with primary α-Mg formation. As solidification proceeds, alloying elements are rejected to the melt and Ca and Zinc-rich phases form in the interdendritic regions. The XRD results provide evidence for the formation of both $Mg_2Ca$ and $Ca_2Mg_6Zn_3$ phases in the as-cast material, while the EDS results demonstrate the presence of the Ca-rich and Zn-rich phases in the interdendritic regions. The possible eutectic solidification is [Zhong 2005]:

$$L \rightarrow hcpMg + Mg_2Ca + Ca_2Mg_6Zn_3 \tag{6.2}$$

The solidification route of the ternary alloys can be followed by isotherms superimposed on the liquidus projection of the Mg-Ca-Zn system, Fig 6.2 [Brubaker and Liu 2004].

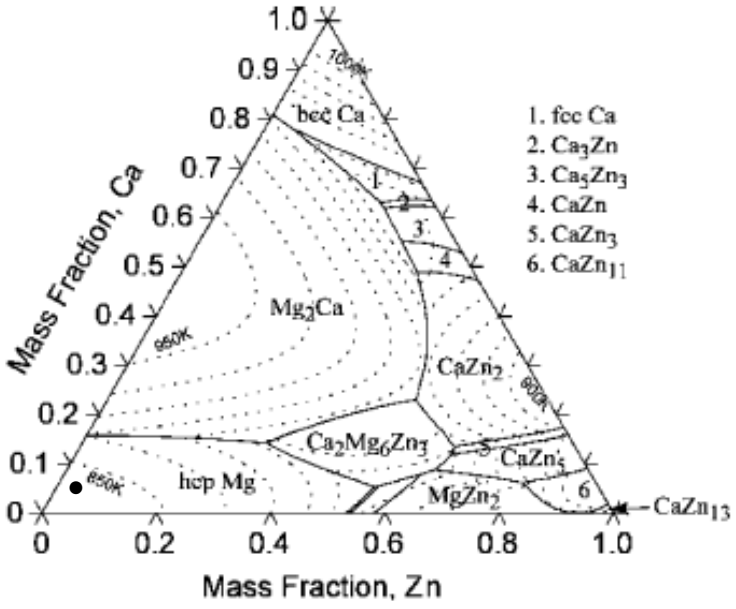


Figure 6.2: The calculated liquidus projection of the Mg-Ca-Zn with the calculated isotherms superimposed. The temperature difference between the isotherms is 50 K [Brubaker and Liu 2004]. Approximate composition of the ternary alloys of the present investigation are shown by the black dot.

It is worth mentioning that as a result of a high concentration of zinc, which has a higher atomic number and thus an increased back scattering effect [Goldstein 1982], regions rich in zinc look bright under the SEM. As there is no peak due to the $MgZn_2$ phase in the XRD spectrums of the ternary alloys, the observed zinc-rich white ribbons are ternary $Ca_2Mg_6Zn_3$ phase. Fenkel *et al.* [2006] have also reported the formation of this phase in eutectic regions of as-cast alloys with compositions close to those of the ternary alloys studied in the present investigation. Although the EDS result does not provide the exact atomic ratio of $Ca_2Mg_6Zn_3$, the difference between the nominal composition of this phase and the EDS results is due to the contribution from the adjacent α-Mg grains, see Fig 6.3.

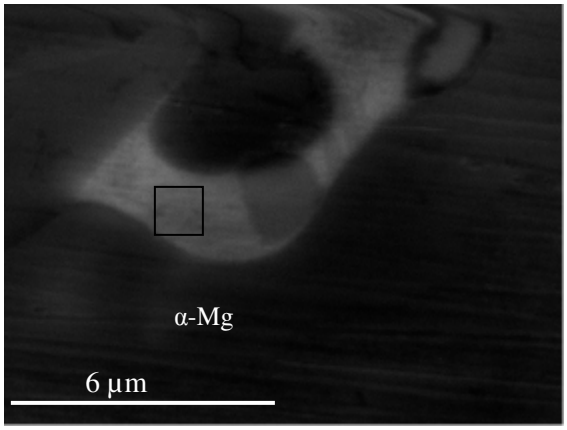


| $Ca_2Mg_6Zn_3$ | Mg | Ca | Zn |
|---|---|---|---|
| Experimental | 56.25 | 15.4 | 27.01 |
| Nominal | 34.57 | 18.97 | 46.45 |

Figure 6.3: Comparison between nominal composition of $Ca_2Mg_6Zn_3$ and EDS analysis of an area shown by the box in zinc rich regions of the as-cast Mg-3Ca- 1 wt% Zn, all values are in wt%.

## 6.3 Microstructural Evolution and Kinetics of Homogenization

### 6.3.1 Binary Alloy

Homogenization heat treatment yields a spheroidized eutectic structure in the binary Mg-2.5Ca alloy, Figs 5.3.b and 5.3.c. Lamellar eutectic structures have high surface energy and are prone to becoming spherodized even at low temperatures [Gupta *et al.* 1999]. Diffusion has been identified as an underlying process for the spherodization of the lamellar structure [Reed-Hill and Abbaschian 1991, Gupta *et al.* 1999].

Generally the temperature dependence of the diffusion coefficient D can be expressed by the following Arrhenius relationship [Porter and Easterling 1992]:

$$D = D_0 \exp\left(\frac{-Q}{RT}\right) \tag{6.3}$$

where Q is the activation energy in (J/mol), $D_0$ is a pre-exponential factor ($m^2/s$), R is the universal gas constant and T is the absolute temperature. For the self diffusion of magnesium $D_0$ and Q are $15\times10^{-5}$ ($m^2/s$) and -136 kJ/mol, respectively [Porter and Easterling 1992].

From Eq. (6.3), the diffusion coefficient of calcium at the homogenization temperature utilized in this study can be approximated from the following equation:

$$\frac{D_{T_2}}{D_{T_1}} = \exp\left[\frac{-Q}{R}\left[\frac{1}{T_2} - \frac{1}{T_1}\right]\right] \tag{6.4}$$

where Q is approximated as 166 kJ/mol [Porter and Easterling 1992], $T_2$ is the homogenization temperature, $T_1$ is chosen as the melting point of calcium (1111K) [Hosford 2007] and $D_{T1}$ is estimated to be $10^{-12}$ ($m^2/s$) [Porter and Easterling 1992, Brown and Ashby 1980]. At 505°C, this gives $D_{T2}=4.62\times10^{-16}$ ($m^2/s$) for the diffusion of calcium in magnesium.

Considering the homogenization temperature of 505°C (778K), and the treatment of random walk for diffusion [Porter and Easterling 1992], i.e. $x = \sqrt{(Dt)}$ where t is time in

seconds, the average distance of diffusion of the elements during the homogenization time of 120 hours can be approximated. The approximate diffusion coefficients and average distance of diffusion of magnesium and calcium atoms after five days of homogenization are given in Table 6.1.

Table 6.1: Diffusion coefficients and average diffusion distances of Mg and Ca at homogenizing temperature of 505°C (778K) and for homogenization time of 120 hours.

| Diffusion | Diffusion Coefficient ($m^2s^{-1}$) | Average Diffusion Distance, $x = \sqrt{D\,t}$, μm |
|---|---|---|
| Mg in Mg | $1.1085\times10^{-13}$ | 218.8 |
| Ca | $4.62\times10^{-16}$ | 14.12 |

As expected, diffusion of calcium in the magnesium matrix is found to be slower. This is due to a larger atomic radius and a higher melting point, which require a higher activation energy for the diffusion of calcium [Brown and Ashby 1980, Schwandt *et al.* 1996]. Using the above results, relaxation time for homogenization, i.e. $\tau = \frac{l^2}{\pi^2 D}$, where $l$ is the primary dendrite spacing, can also be calculated [Reed-Hill and Abbaschian 1991, Porter and Easterling 1992]. Considering a primary dendrite spacing of 15μm (from Fig 5.1.a), relaxation time needed for homogenization can be approximated as 62 hrs. This is consistent with the experimental results demonstrating that the dendritic structure is effectively eliminated by the present homogenization heat treatment.

During homogenization surface energy of the lamellar α-Mg+ $Mg_2Ca$ structure can be reduced by first diffusion of magnesium from the α-Mg of the eutectic lamella. It can be proposed that $Mg_2Ca$ structure coarsens while the grain boundaries provide fast routes for diffusion of calcium. $Mg_2Ca$ particles at grain boundaries will act as sinks for extra calcium

atoms [Finkel *et al.* 2006]. The EDS analysis results from the large calcium particles within Mg grains, Fig 5.4.b, and the presence of $Mg_2Ca$ particles on the grain boundaries in Fig. 6.4 support this hypothesis.

The band like structures observed in Fig 5.36., apparently initiated from the grain boundaries, can be attributed to twinning in the magnesium matrix as a result of quenching from the homogenizing temperature. Tensile stresses developed during quenching from the homogenization temperature, i.e. $\sigma = \alpha E \Delta T$ where α is a coefficient of linear expansion, E is the Young modulus and ΔT is a temperature gradient [Dowing 2007], can likely initiate twin nucleation in the magnesium matrix, as reported by [Padfield 2004].

### 6.3.2 Ternary Alloys

The microstructural evolution from the as-cast to the homogenized structure in the ternary alloys shows characteristics similar to the binary alloy. In ternary alloys, however, the effect of zinc must also be considered. As the EDS results of the as-cast and homogenized samples show, the calcium content of α-Mg shows no significant change due to homogenization. It is also interesting to note that the zinc contents of the α-Mg grains are not significantly different from those of the as-cast dendritic arms in both ternary alloys. The observed zinc level of α-Mg matrix is consistent with the solubility of zinc in magnesium according to the binary Mg-Zn, Fig 2.9. Levi *et al*. [2006] have suggested that for an Mg-Ca-Zn alloy containing 1.6 wt% Ca and 3.2 wt% Zn, the homogenization microstructure contains mainly α-Mg and $Mg_2Ca$ phases, Fig 6.4. This seems to be the case for the present ternary alloys, as well.

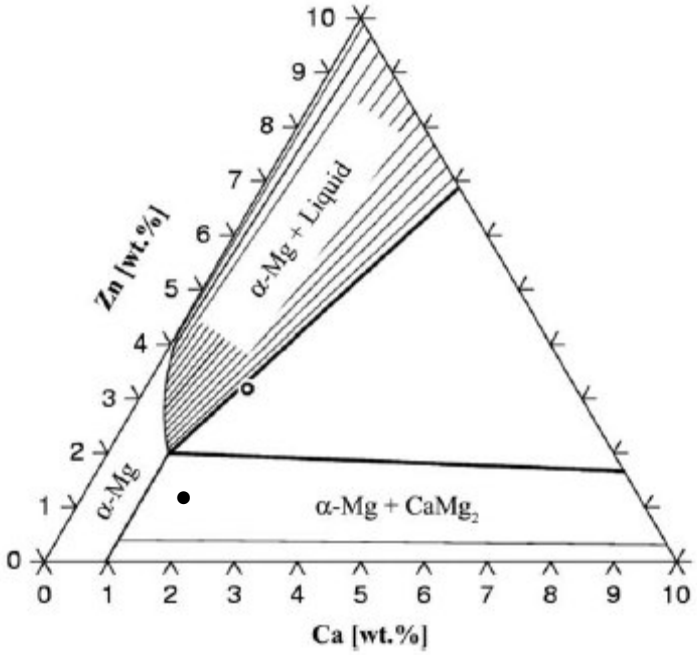


Figure 6.4: Calculated isothermal cross section at 465°C in the Mg-Ca-Zn system, the black dot corresponds to the Mg-2Ca-1Zn alloy of the present investigation [Levi *et al.* 2006].

Although XRD tests have not been done on as-homogenized samples, the EDS results associated with the interdendritic and triple junction/ grain boundary regions in Fig 5.27.(a and b) support the presence of the Zn-rich $Ca_2Mg_6Zn_3$ phase in the homogenized alloys, as well.

It should be noted that the TEM investigation on the Mg-2Ca-1Zn alloy has suggested that $Mg_2Ca$ particles may contain zinc, as well, Fig 6.5. Further work is needed to study the exact nature of this phase in ternary alloys.

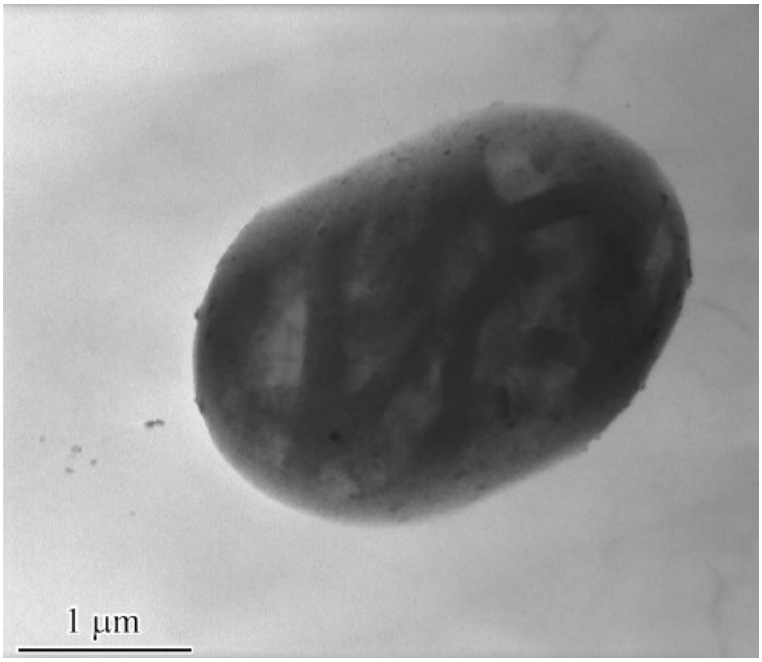


| | Mg | Ca | Zn |
|---|---|---|---|
| Particles | 69.56 | 29.18 | 1.27 |
| Matrix | 99.48 | 0.2 | 0.32 |

Figure 6.4: Bright filed TEM micrograph and EDS analysis of a potentially Mg2Ca particle formed during homogenization of the Mg-2Ca-1Zn, all results are in at%. TEM work by V.Y. Gertsman.

The diffusion coefficient of zinc in magnesium can be calculated by using equation 6-3 and considering that Q=119.7 kJ/mol and $D_0 = 0.41\times10^{-4}\,(\mathrm{m^2/s})$ [Cohen *et al.* 2006]. Accordingly, the diffusion coefficient of zinc in magnesium is found to be $0.91\times10^{-13}$ $(\mathrm{m^2/s})$ at the homogenization temperature of 450°C. This value, along with the values calculated for diffusion of calcium, and the self diffusion of magnesium at 450°C are tabulated in Table 6.2. It is evident that zinc has the highest diffusion coefficient among the three diffusing elements. The average diffusion distance for Mg, Ca and Zn for the homogenization process

of the ternary alloys are also calculated and included in Table 6.2. The results suggest that the diffusion of Zn in Mg plays an important role in the evolution of the microstructure during homogenization.

Table 6.2: Diffusion coefficients and average diffusion distances of Mg, Ca and Zn calculated for homogenizing for 96 hours at 450°C (723K).

| Diffusion | Diffusion Coefficient ($m^2s^{-1}$) | Average Diffusion Distance, $x = \sqrt{D\,t}$, μm |
|---|---|---|
| Mg in Mg | $22.35\times10^{-15}$ | 87.89 |
| Ca | $6.91\times10^{-17}$ | 4.88 |
| Zn in Mg | $0.92\times10^{-13}$ | 178.3 |

## 6.4 Precipitation Hardening Behavior of the Alloys

### 6.4.1 Introduction

In this section, the precipitation hardening behavior of the alloys investigated are analyzed; effects of alloy composition, aging time and temperature on the aging response of the alloys will be discussed in depth. Combined information from various characterization methods used in the present investigation will be used to give an insight to the precipitation behavior of the alloys. The summary of the aging behavior of the alloys is presented in Table 6.3.

Table 6.3: Isothermal aging behavior of the binary and ternary alloys,

(ΔH=max hardness − hardness of as- homogenized condition.)

| Aging T (°C) | Mg-2.5Ca | | | | Mg-2Ca-1Zn | | | | Mg-2Ca-2Zn | | | |
|---|---|---|---|---|---|---|---|---|---|---|---|---|
| | Time to the peak-aged condition (hrs) | | Aging response | | Time to the peak-aged condition (hrs) | | Aging response | | Time to the peak-aged condition (hrs) | | Aging response | |
| | Hardness data | IC data | ΔH (VHN) | Heat Flow (J/g) | Hardness data | IC data | ΔH (VHN) | Heat Flow (J/g) | Hardness data | IC data | ΔH (VHN) | Heat Flow (J/g) |
| 175 | 1.0 | NA | 4.0 | NA | 6.0 | 8.0 | 13.0 | 1.29 | 10.0 | 9.7 | 10.0 | 0.95 |
| 200 | 2-10 | 8.5 | 4.0 | 0.72 | 8.0 | 7.0 | 14.0 | 5.26 | 2-8 | 6.8 | 10.0 | 5.42 |
| 220 | 2-12 | 8.0 | 2.0 | 3.247 | 0.5 | 1.0 | 15.0 | 5.04 | 1.0 | 1.4 | 14.0 | 5.17 |

### 6.4.2 Aging Behavior of Mg-2.5Ca Alloy

The alloy is a binary alloy with calcium content in excess of the solid solubility. Therefore, the alloy in the supersaturated solid solution condition, i.e. as-homogenized, have significant volume fraction of large $Mg_2Ca$ particles. Table 6-3 summarizes the aging response of the alloy using both hardness and IC data. The time to the peak-aged condition is also included in the table. The information verifies the small age hardening response expected from this alloy. The results are consistent with the results by Nie and Muddle [1997] on the binary Mg-Ca alloy of their study.

The small increase in hardness of the binary alloy can stem from:

1 - Binary Mg-Ca phase diagram shows small solubility of calcium in the magnesium matrix, i.e. only 1.34 wt% at the eutectic temperature of 516°C. This limited solubility does not provide the large amount of solutes required for a homogeneous precipitation within α-Mg. Low solubility of calcium in magnesium at homogenization temperatures also provide a low driving force for the nucleation of precipitates. The driving force for nucleation of precipitates in dilute alloys can be written as [Starink *et al.* 2005]:

$$\Delta G_v = \frac{RT}{V_m} \ln\left(\frac{c_0}{c_e}\right) \tag{6.5}$$

where $V_m$ is the molar volume of a precipitate, R the gas constant, $c_0$ the alloy composition, and $c_e$ is an equilibrium solute concentration in the matrix at the aging temperature of T.

2 – Since the basic mechanism of hardening may be assumed to be an Orowan mechanism, (this will be discussed further in precipitation hardening mechanism in the binary alloy) $Mg_2Ca$ shape, orientation and number density will affect the hardening response of the alloy. Slip in magnesium occurs predominantly on the close packed basal planes (0001) and if $Mg_2Ca$ precipitates lie parallel to the basal plane, dislocations will easily pass between them and thus the hardening increment will be small [Celotto 2000]. Determining shape, orientation and number density of possible $Mg_2Ca$ precipitates requires extensive TEM studies and is not in the scope of the current research. Further investigation is required to determine if this is a major cause of small hardening. It is noteworthy that in the binary Mg-Sn system, in spite of the high density of precipitates, hardening increment as a result of isothermal aging is small which is attributed to the orientation relationship between the precipitates and matrix [Mendis *et al.* 2006].

3 - The composition of the binary alloy in the present investigation, i.e. ~2.5 wt% Ca, lies in the binary α-Mg+$Mg_2Ca$ part of the Mg-Ca phase diagram. In other words, a significant fraction of the $Mg_2Ca$ phase present in the as-cast microstructure will not dissolve during homogenization. Therefore, as Fig 5.4.b shows, there are already available nucleation sites for the potential $Mg_2Ca$ precipitates. Comparing lattice parameters of $Mg_2Ca$ (a=0.623 nm) and the magnesium matrix (0.321 nm) shows a large misfit between crystal structures. It is highly likely that most nucleation happens heterogeneously on the already available $Mg_2Ca$ particle.

Further discussion on the poor aging response of the binary Mg-2.5Ca will be presented with the aid of IC and DSC results which will bring more insight to the precipitation behavior of the alloy. IC results further show that the aging response is almost zero when temperature is 175°C. IC results also show that the aging response can be improved by increasing the aging temperature to 220°C, while the aging kinetics is not much different when temperature is increased from 200°C to 220°C. The higher aging response at 220°C, however, has not translated to a higher age hardening response. This is possibly due to the formation of incoherent equilibrium phases rather than coherent phases. Incoherent particles are non-shearable and therefore as mentioned hardening mechanisms can be described by the Orowan mechanism.

The suggestion of equilibrium phase is consistent with the DSC result, Fig 6.5, showing a single exothermic peak in the temperature range of 200°C-300°C. No initial heat release corresponding to clustering or formation of transitional phases is detected. It is also consistent with the small hardness increase with ramp heating up to 240°C, i.e. when a good portion of the exothermic heat has been released meaning formation of large volume fraction of precipitates.

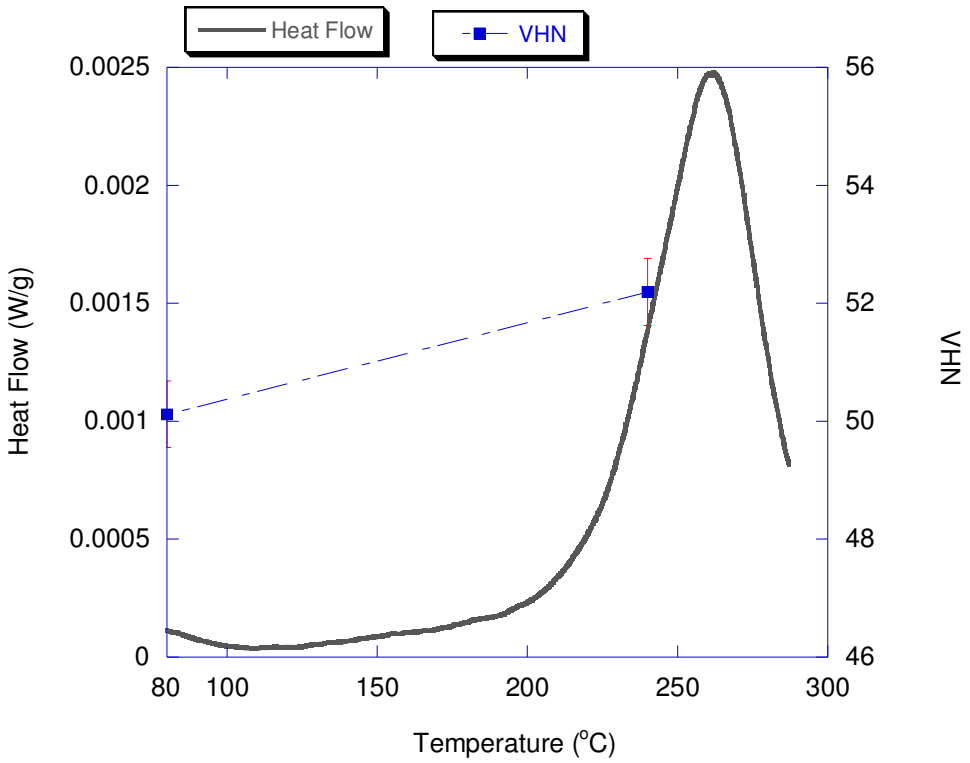


Figure 6.5: Non-isothermal hardness evolution superimposed on the DSC trace of the Mg-2.5Ca.

Comparing the isothermal hardness and IC data, Fig 6.6, shows that the exothermic heat release up to about 0.8 hours in the case of 200°C has not resulted in any increase in hardness. Similarly, no direct correlation between hardness and heat flow data. This behavior again provides evidence for the lack of formation of coherent hardening phases during aging of this alloy.

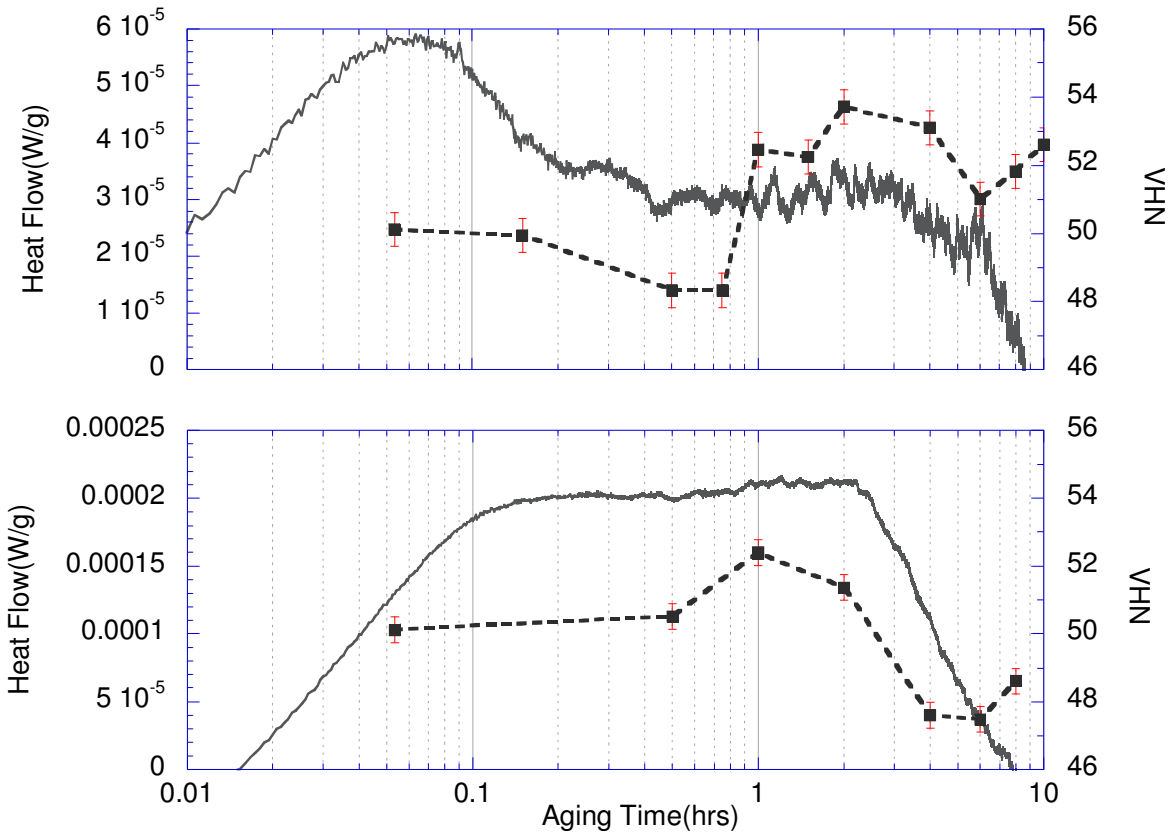


Figure 6.6: Isothermal hardness evolution superimposed on the isothermal calorimetry traces of the Mg-2.5Ca alloy.

It is worth mentioning that Esmaeili [2002] has shown that the exothermic heat flow due to the precipitation of coherent phases in the aluminum alloy AA6111 results in substantial increase in yield strength, Fig 6.7, and tf coincides with the time to reach the maximum yield strength on the aging curve. This is not the case for the current Mg-2.5Ca alloy.

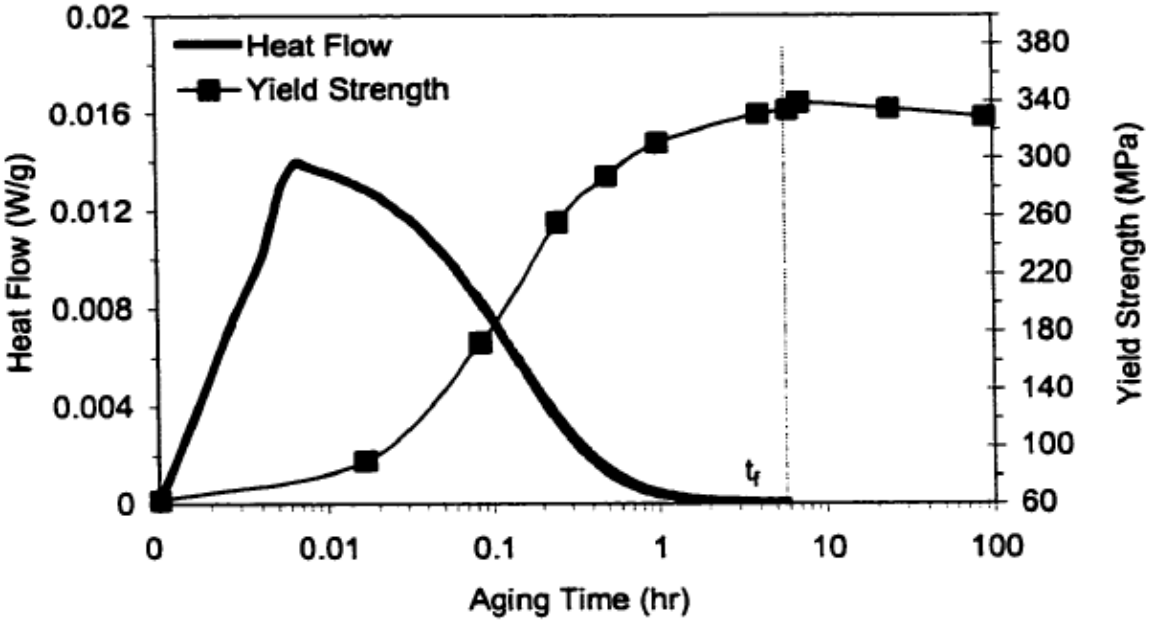


Figure 6.7: The heat evolution and yield strength of the alloy AA6111 during isothermal aging at 180°C [Esmaeili 2002].

Due to lack of measurable IC data for 175°C no precipitation kinetics analysis is done for this alloy. More TEM investigation in the future can help verify the lack of the coherent phases and the formation of non-deformable precipitates from the beginning of aging.

### 6.4.3 Aging behavior of Mg-2Ca-1Zn Alloy

As a result of adding zinc, hardness in homogenized and aged ternary alloys has increased. A pronounced increment in hardness during aging as a result of adding zinc to the binary Mg-2.5Ca can be seen in Fig 6.8 and in Table 6.3 as well. However, according to the hardness data, zinc has not significantly reduced the time to reach the peak-aged condition. It

should be stressed that current results on the increased hardness are consistent with the literature reports. [Nie and Muddle 1997, Bamberger *et al*. 2005]. The maximum age hardening response in the current system is 14 VHN and 15 VHN at 200°C and 220°C, respectively. This response is less than what is reported for commercial AZ91 alloy, showing increase in hardness from 58 VHN to 82 VHN after 10 hours of aging at 200°C [Celotto 2000].

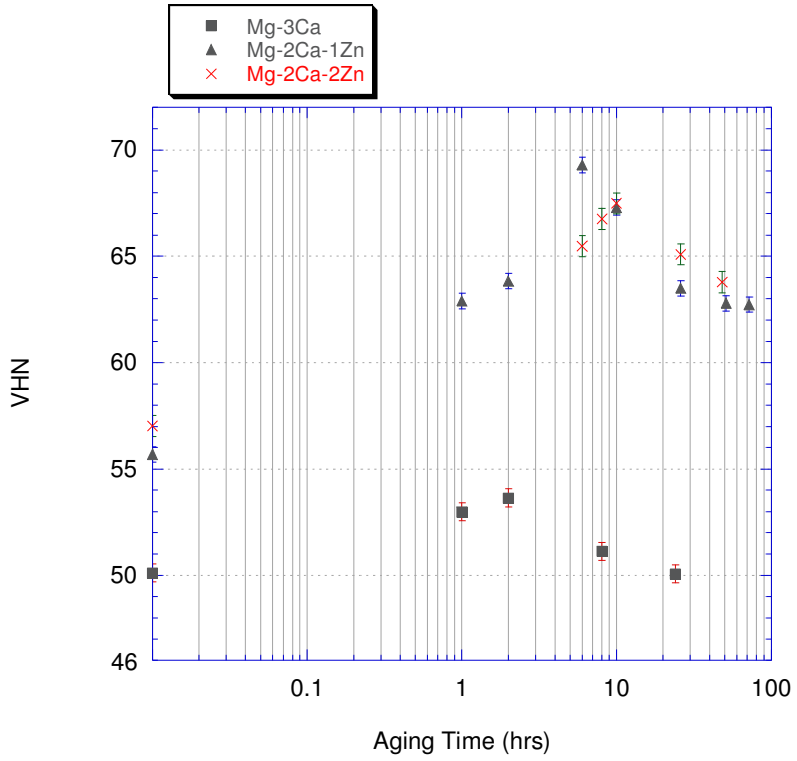


Figure 6.8: Evolution of hardness in the binary and ternary alloys as a result of isothermal aging at 175°C.

The potential mechanisms involved in promoting hardness as a result of adding zinc are as follows:

1. Adding zinc to the binary Mg-Ca alloys likely results in the formation of Zn-containing transitional and equilibrium precipitates during aging, in addition to solely $Mg_2Ca$ particles. Particularly $Ca_2Mg_6Zn_3$ can precipitate during isothermal aging after homogenization heat treatment in the ternary alloys [Levi *et al*. 2006]. Crystal structure of this phase is different from the $Mg_2Ca$. The XRD results of the present investigation on the ternary alloys aged for six hours at 175°C confirm the presence of $Ca_2Mg_6Zn_3$. Nie and Muddle [1997] showed lower misfit between an Mg-Ca-Zn ternary phase and the magnesium matrix compared to the $Mg_2Ca$ and matrix by 50%, although they did not directly mention $Ca_2Mg_6Zn_3$. In other words, the energy barrier for nucleation of the ternary phase might be lower and therefore a larger density of hardening precipitates might form in the ternary alloy. In the ternary alloys, the participation of zinc in the $Mg_2Ca$ particles possibly results in the formation of $(Mg)_2Ca$-Zn type precipitates, as also suggested by Oh *et al.* [2005]. The presence of zinc in $Mg_2Ca$ precipitates is shown to lower the lattice parameters of this phase [Oh *et al.* 2005]. These precipitates have likely lower misfit energy barrier for nucleation with magnesium matrix containing zinc. Oh *et al.* [2005] has related hardening of Mg-0.3 at% Ca-0.3 at% Zn to the formation of nanoscale precipitates of $Mg_2Ca$ containing 8 at% Zn, Fig 6.9.

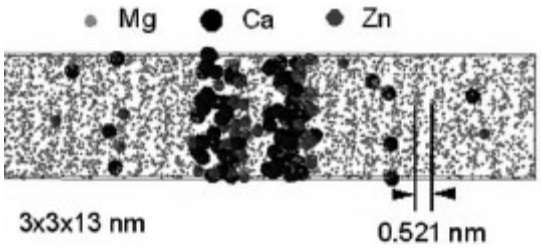


Figure 6.9: 3 DAP elemental map obtained from the selected volume of 3×3×11 $nm^3$ of Mg-3 at% Ca-3 at% Zn aged for 60 ks.

Table 6.3 demonstrates that larger maximum hardness values are generally associated with larger total heat effects compared to the binary alloy. Also the time to the maximum hardness closely match $t_f$ from IC. This may reflect a different precipitation behavior compared to the binary alloy. This can be further evaluated by plotting the isothermal aging results from IC and hardness tests as shown in Fig 6.10.

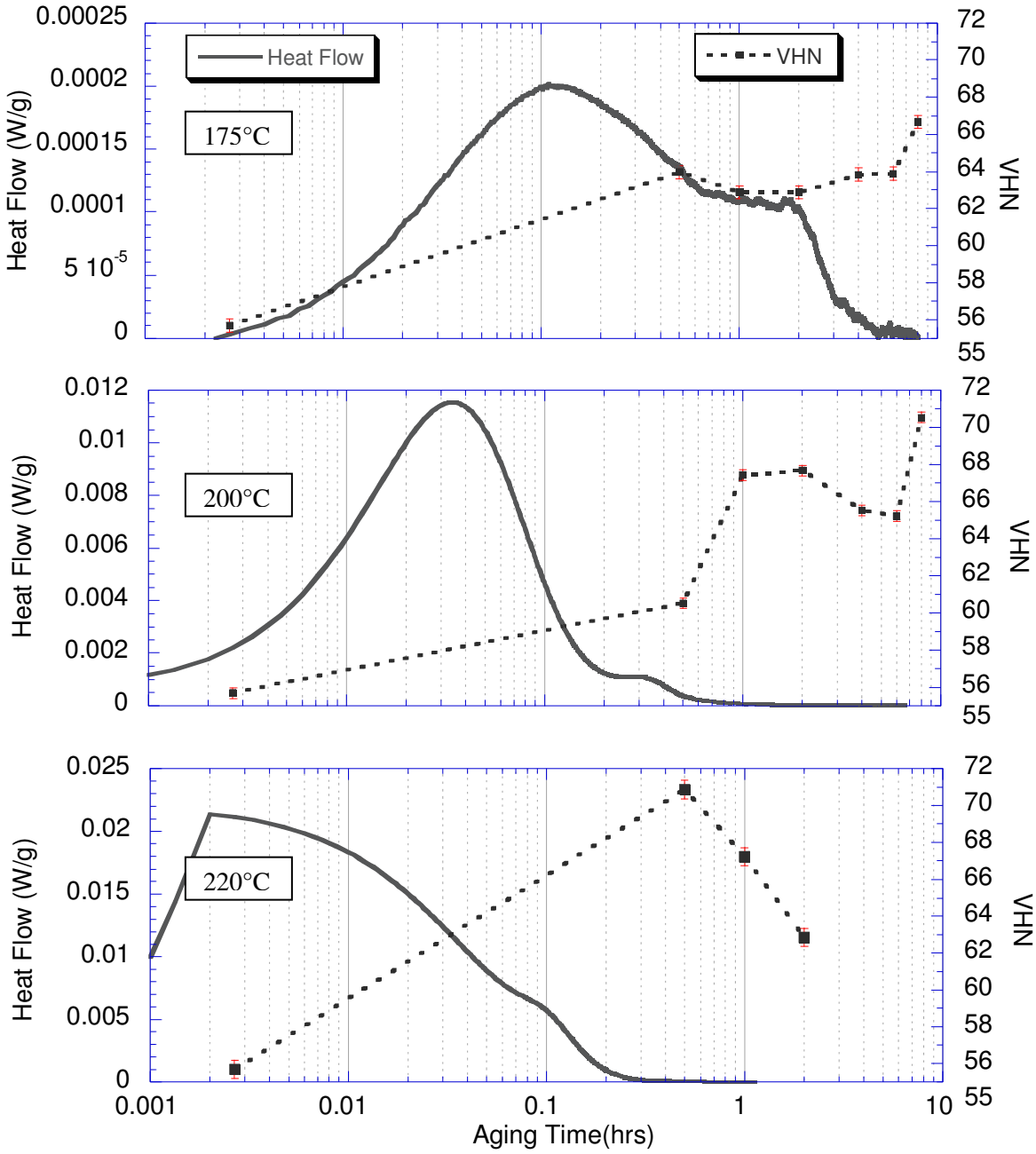


Figure 6.10: Isothermal hardness evolution superimposed on the isothermal calorimetry traces of the Mg-2Ca-1Zn alloy.

Fig 6.10 shows that the increase in hardness from the very beginning of aging at each temperature is associated with the exothermic event representing formation of precipitates. This behavior is similar to the behavior of AA6111 shown in Fig 6.7. This suggests that coherent precipitates during aging of Mg-2Ca-1Zn alloy form and result in the pronounced hardening of the alloy. Oh *et al.* [2005] relates hardening of dilute Mg-Ca-Zn alloys to formation of coherent GP zones. Exact mechanism of hardening, however, is not known and needs further investigation.

In the analysis of IC traces of the Mg-2Ca-1Zn, Figs 5.21 (a and b), presence of the plateau region is noticeable. The plateau region in traces of 175°C and 200°C and a shoulder in trace of 220°C suggest the formation of more than one type of phase during isothermal aging supported by the XRD results. As Fig 6.11 shows the plateau can happen if there are two overlapping exothermic effects. Since there is not a major increment in hardness associated with the plateau, Fig 6.10, it is possible that this plateau is partly due to the formation of equilibrium (e.g. $Mg_2Ca$) precipitates which are shown to have a little effect in increasing hardness.

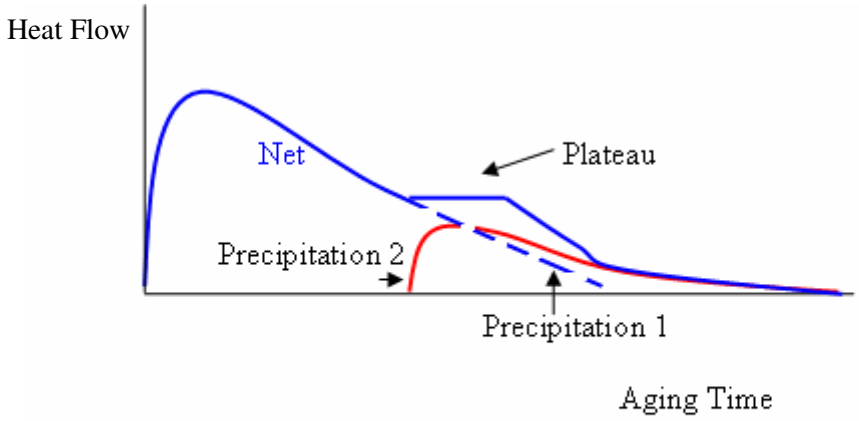


Figure 6.11: Schematics of the possible overlapping thermal events during isothermal calorimetry.

Further to the above, the combined non-isothermal aging results in Fig 6.12 suggests that DSC peaks I and II are associated with the formation of coherent/metastable phases, while the dissolution of the phase associated with peak II results in decrease in hardness. Recent HRTEM studies by Oh *et al.* [2005] have shown formation of GP zones during precipitation process of dilute Mg-Ca-Zn alloys. Continuous increase of hardness over 150°C-200°C and no decrease of hardness on trough III which is an endothermic heat effect can be due to overlap of endothermic event with exothermic effects which effectively contribute to hardening. It is likely that some clusters or GP zones formed at peak I are dissolving, producing fresh solutes for evolution of the second exothermic phase, i.e. peak II. The maximum hardness level which is achieved by the formation of the phase associated with Peak II in Fig. 6.12 is approximately the same as the maximum hardness achieved by isothermal aging to the peak-aged condition at all three tested temperatures. Thus this

exothermic peak is associated with the formation of the most effective hardening phase, termed phase II, hereafter. The dissolution of phase II, which is reflected by trough IV and possibly coincides with the formation of an equilibrium phase, results in the decrease in hardness.

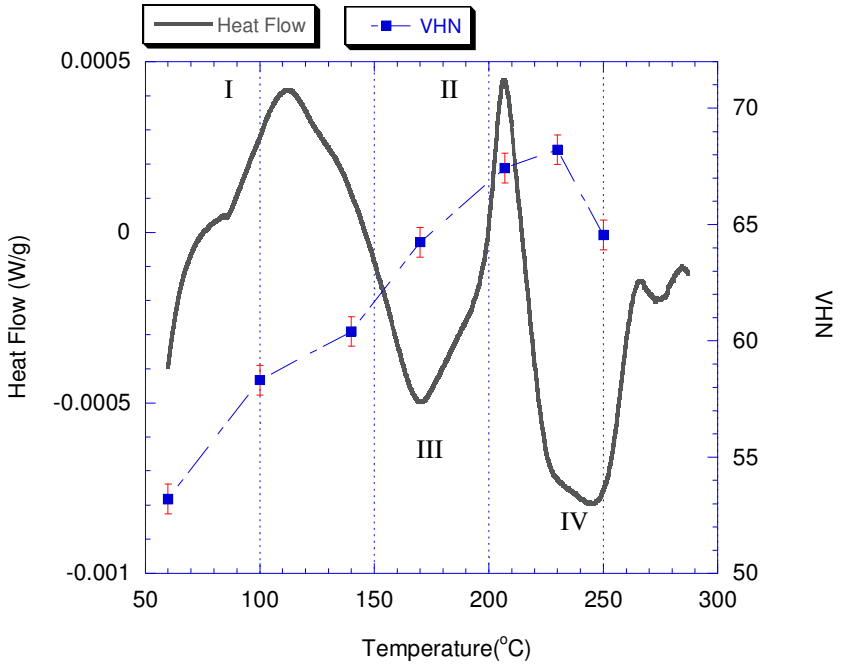


Figure 6.12: Non-isothermal hardness evolution superimposed on the DSC trace of the Mg-2Ca-1Zn.

#### 6.4.3.1 Precipitation Kinetics

The isothermal calorimetry traces are used to (a) estimate the relative volume fraction of precipitates as a function of aging time and (b) obtain the precipitation kinetics parameters. This is particularly useful, considering that the precipitation reactions analyzed by isothermal calorimetry well describe the hardening behavior of the alloy. The analysis method follows

the approach developed by Esmaeili [2002], as described in Chapter 2, and the JMAK model. Accordingly, heat flow data from the IC curves, i.e. $\left(\frac{dQ}{dt}\right)$, is used to determine the relative volume fraction of precipitates after time t according to equation (2.14). The results of the analysis are shown in Fig. 6.14. To obtain n and k parameters of the JMAK model, the parameter ln ln$(\frac{1}{1-f_r})$ is plotted vs. ln (t). The y-axis intercept and the slope of the resultant line in the range of 5-95% $f_r$ are then used to obtain the JMAK parameters.

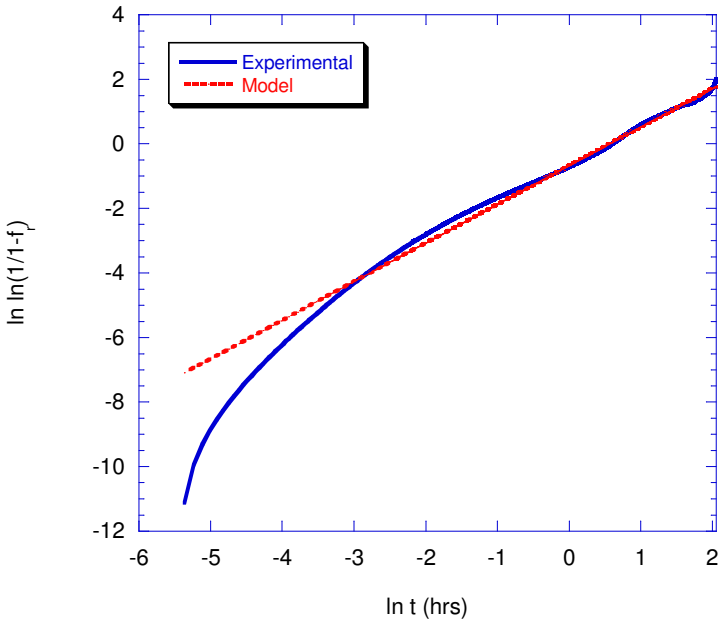


Figure 6.13: Procedure of obtaining kinetics parameters from experimental isothermal trace of Mg-2Ca-1Zn.

The results of the JMAK analysis (i.e. equation 2.15) are also plotted in Figure 6.14. As the figure shows, increasing aging temperature from 175°C to 220°C has shortened time for formation of total volume fraction of precipitates which is due to the faster diffusion of alloying elements and thus faster kinetics of the phase transformation. JMAK parameters obtained from the above procedure for the alloy at aging temperatures of 175°C, 200°C and 220°C are shown in Table 6.4.

Table 6.4: Kinetics parameters, n and k for the Mg-2Ca-1Zn alloy.

| Aging Temperature (°C) | n | k($hr^{-1}$) |
|---|---|---|
| 175 | 1.19 | 0.51 |
| 200 | 0.56 | 2.65 |
| 220 | 0.81 | 8.38 |

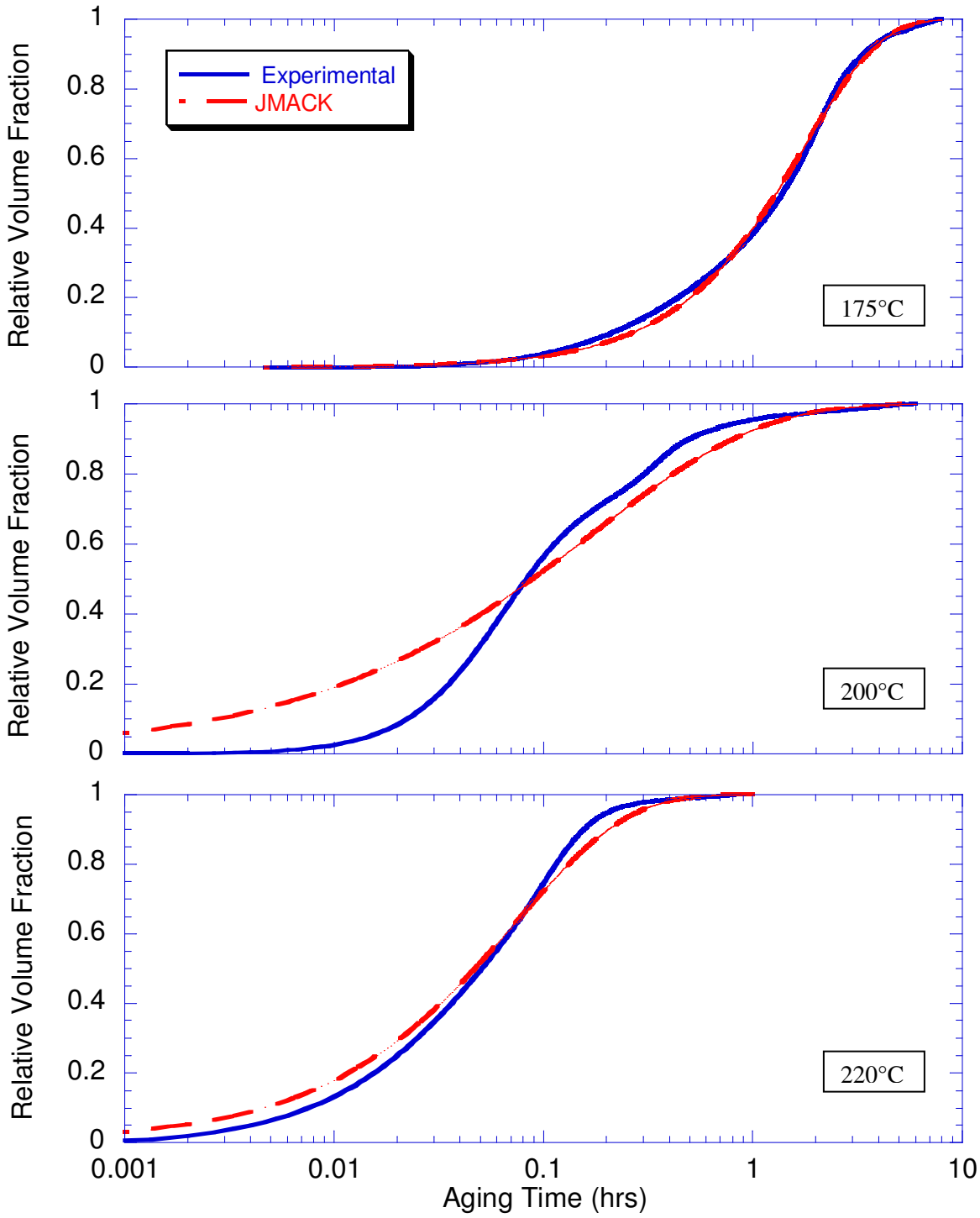


Figure 6.14: Evolution of volume fraction of precipitates for Mg-2Ca-1Zn.

The kinetic parameter k is strongly temperature dependent, including both nucleation and growth parameters, and follows Arrhenius-type relationship with temperature as follows [Esmaeili *et al.* 2003a]:

$$k = k_0 \exp\left(\frac{-Q}{RT}\right) \tag{6.6}$$

where Q is an apparent activation energy in J/mol, T is absolute temperature in Kelvin, R is the universal gas constant and $k_0$ is the proportionality constant. Q is obtained from the slope of the plot of ln(k) vs.1/T, Fig 6.13. Considering the reported values for k in Table 6.6 and the slope of the line fitted to the values at 175°C, 200°C and 220°C (Fig. 6.15), Q will be 110.817 kJ/mol. It should be noted that this estimated energy is not considered as the activation energy for precipitation, as it stems from the sum of the positive and negative energies associated with the nucleation and diffusional growth mechanisms [Esmaeili *et al.* 2003a, Berkenpas *et al.* 1986].

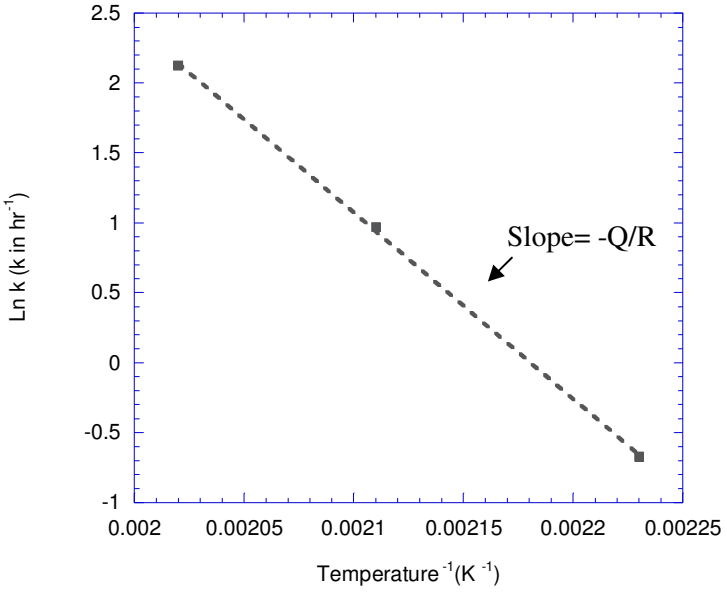


Figure 6.15: Plot of JMAK parameter k vs. inverse of the absolute temperature.

### 6.4.4 Aging Behavior of Mg-2Ca-2Zn

Increasing zinc content of the alloy in Mg-2Ca-2Zn, as shown in Table 6.3 and also in Fig 6.8, has not significantly changed the aging behavior of the alloy. As Fig 6.8 shows, level of hardness increase compared to the binary alloy is almost the same. As Table 6.3 illustrates, aging response as total evolved heat shows close values to that of the Mg-2Ca-1Zn alloy. Also, larger maximum hardness values are associated with larger total heat effects compared to the binary Mg-2.5Ca.

Fig 6.16 shows that increase in hardness from the very beginning of aging at each temperature is associated with the exothermic event representing formation of precipitates. This behavior is similar to the alloys AA6111 and Mg-2Ca-1Zn, Figs 6.7 and 6.10,

respectively. As discussed in the case of Mg-2Ca-1Zn this can be attributed to the evolution of coherent precipitates during aging of the alloy.

IC traces show similar pattern as the Mg-2Ca-1Zn alloy. The plateau in the IC traces of the alloy can be interpreted as a concurrent precipitation of more than one type of precipitates which is illustrated in Fig 6.11.

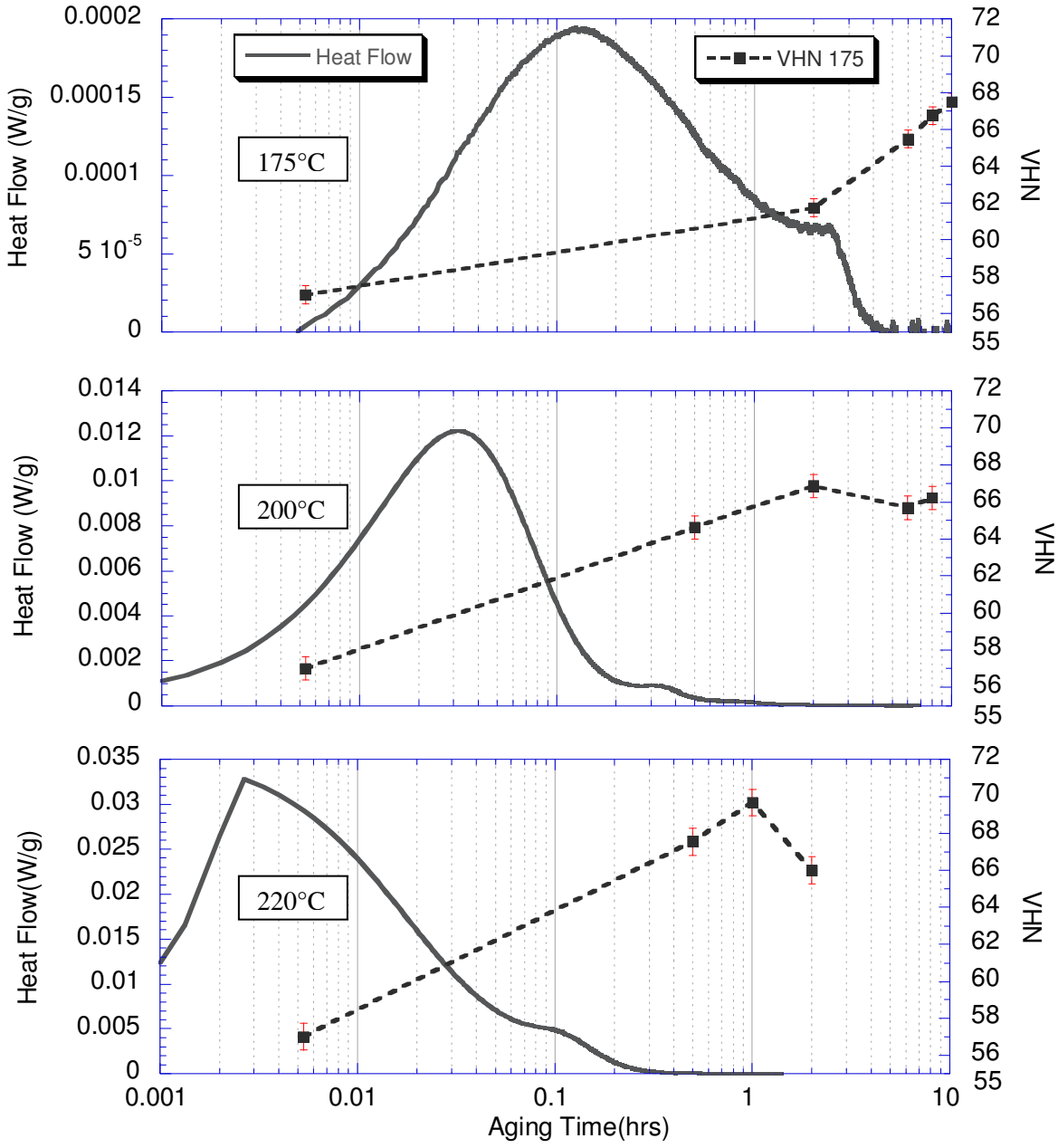


Figure 6.16: Isothermal hardness evolution superimposed on the isothermal calorimetry traces of the Mg-2Ca-2Zn alloy.

Considering the non-isothermal aging tests, it appears that the first exothermic peak, i.e. Peak I in Fig. 6.17, does not correspond to an increase in hardness in Mg-2Ca-2Zn alloy. However, the non-isothermal hardness evolution in the range of 140 to 250°C shows similar increasing pattern as in the case of Mg-2Ca-1Zn alloy. This increase in hardness is associated with the major exothermic peaks, II and III. The fluctuations in hardness might be purely due to the scatter in hardness data or the fact that the hardness samples have been aged in the air furnace and there might be a lag in the temperature of the sample due to the furnace/sample size and heating of the sample to the set temperature. On the other hand, the DSC temperature profile accurately shows the sample temperature. Formation of precipitates associated with peak III might be responsible for the increase in hardness beyond that in the Mg-2Ca-1Zn alloy case in temperature range of 230°C-250°C. The major dissolution effects designated as troughs V and VI seem to be due to the dissolution of some preceding precipitates, producing fresh solute atoms for the formation of the precipitates corresponding to peaks II and IV, respectively. This additional peak might be due to precipitates formed by impurities such as Cu, Ce and La. It should be noted that the TEM investigation on the aged ternary alloys of the present investigation has confirmed the presence of Ce and La-containing precipitates.

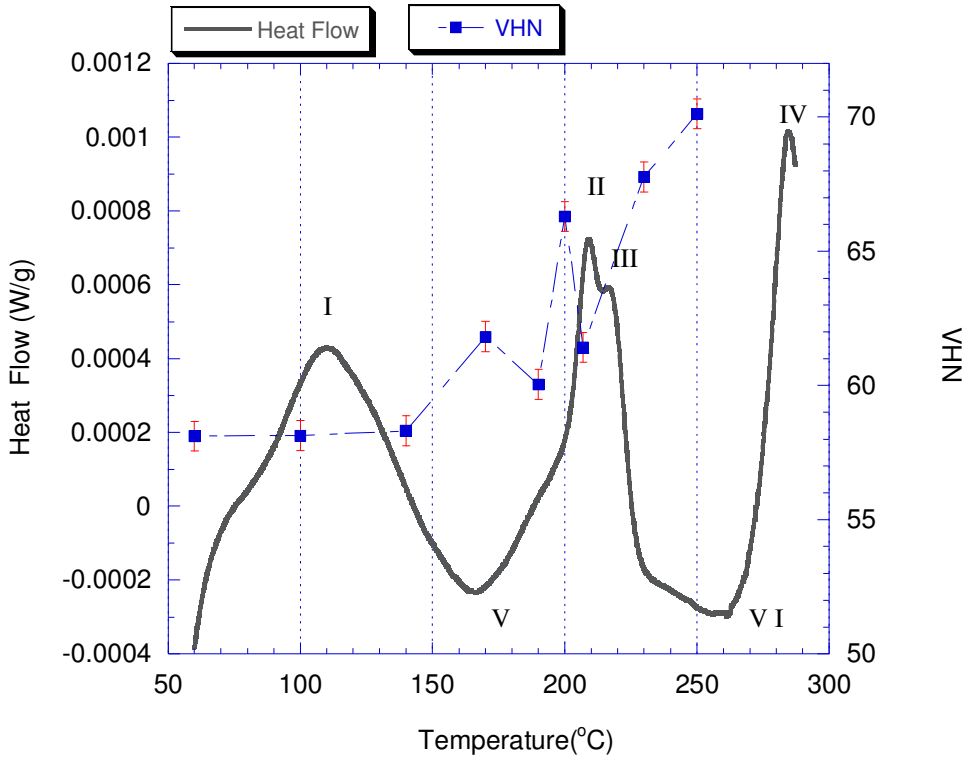


Figure 6.17: Non-isothermal hardness evolution superimposed on the DSC trace of the Mg-2Ca-2Zn.

#### 6.4.4.1 Precipitation Kinetics

Similar to the procedure explained for the Mg-2Ca-1Zn alloy in section 6.4.3.1, the evolution of the relative volume fraction of precipitates during isothermal aging has been evaluated using the isothermal calorimetry results. The analysis results have been shown in Fig. 6.18. The JMAK analysis is also performed for the Mg-2Ca-2Zn alloy. The results of the JMAK fit to the data estimated for the relative volume fraction of precipitates are shown in Fig 6.18, as well. The JMAK parameters for the alloy obtained from experimental IC data at aging temperatures of 175°C, 200°C and 220°C are listed in Table 6.5. Comparison of the kinetic parameters of the Mg-2Ca-2Zn alloy with the corresponding parameters of the Mg-2Ca-1Zn alloy shows that both n and k are relatively close in the two alloys. In both alloys, k

significantly increases with increasing temperature, while n varies between approximately 0.5 and 1.2.

Table 6.5: JMAK parameters for the alloy Mg-2Ca-2Zn.

| Aging Temperature (℃) | n | k($hr^{-1}$) |
|---|---|---|
| 175 | 1.08 | 0.71 |
| 200 | 0.53 | 2.32 |
| 220 | 0.71 | 6.77 |

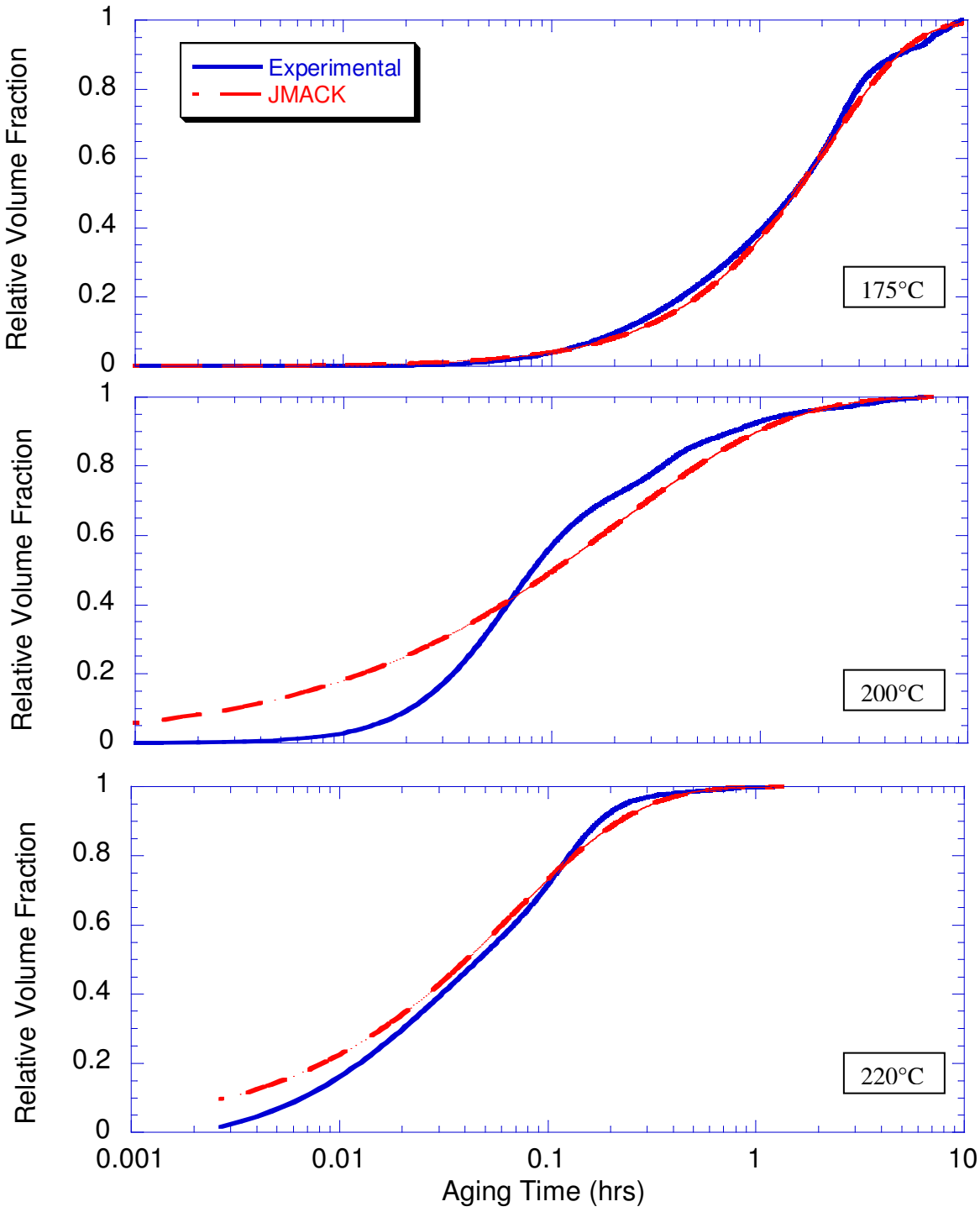


Figure 6.18: Evolution of volume fraction of precipitates for the Mg-2Ca-2Zn alloy.

Arrhenius relationship of k with temperature as described in equation 6.6 is used to find Q and $k_0$ values. The resultant plot is shown in 6.19. The value for Q, which is obtained from the slope of the plot of the ln(k) vs.1/T, is found to be 92.23 kJ/mol. As mentioned earlier, this apparent activation energy is considered as the sum of positive and negative energies when both nucleation and growth mechanisms govern the transformation kinetics. The values for the $k_0$ parameter are 29.06 ($hr^{-1}$) and 24.36 ($hr^{-1}$) in Mg-2Ca-1Zn and Mg-2Ca-2Zn alloys, respectively.

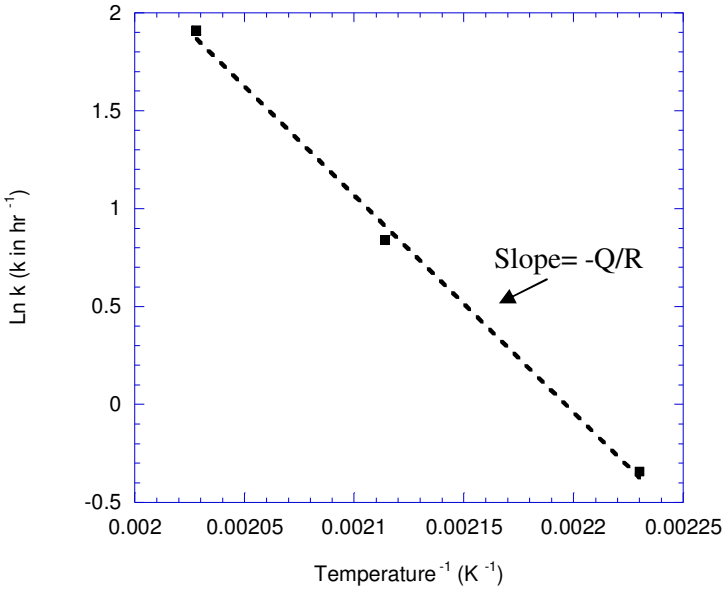


Figure 6.19: Plot of JMAK parameter k vs. inverse of an absolute temperature.

Finally, kinetics parameters of the ternary alloys are compared in Table 6.6. It should be noted that in this table the value of n for each alloy is the average of the previously tabulated n values at three isothermal aging temperatures. As summarized, the apparent activation energy in the ternary alloy containing 2 wt.% zinc is smaller than that in the alloy containing 1 wt% zinc. Thus it is possible that the higher zinc content of the matrix affects diffusional processes during aging by lowering the activation energy for diffusion.

Table 6.6: Apparent activation energy, Q, and kinetic parameters for the Mg-2Ca-1Zn and Mg-2Ca-2Zn alloys.

| Alloy | Q (kJ/mol) | $k_0$ ($hr^{-1}$) | n |
|---|---|---|---|
| Mg-2Ca-1Zn | 110.82 | 29.06 | 0.85 |
| Mg-2Ca-2Zn | 92.23 | 24.36 | 0.77 |

### 6.4.5 Summary on the Precipitation Sequence in the Alloys

To wrap up the discussion chapter, summary on the precipitation sequence of the alloys of the present investigation is presented. It should be emphasized that the terminology used for describing the precipitation sequence from DSC results follows the customary practice of designating peaks when the exact identities of the precipitates are not known. The identification of these phases, as well as their orientation relationship with the matrix and hardening mechanisms need future detailed TEM study. As Fig 6.20 shows, the precipitation sequences for the ternary alloys are relatively similar. The sequence is however different for the binary alloy, and while there are multiple exothermic peaks for the ternary alloys, there is

only a large single exothermic peak for the binary alloy. Finally, it should be mentioned that melting points of the alloys are higher than the temperature range of the DSC runs. Therefore, the melting events or any other possible phase transformation reactions at temperatures higher than 300°C have not been recorded in this study.

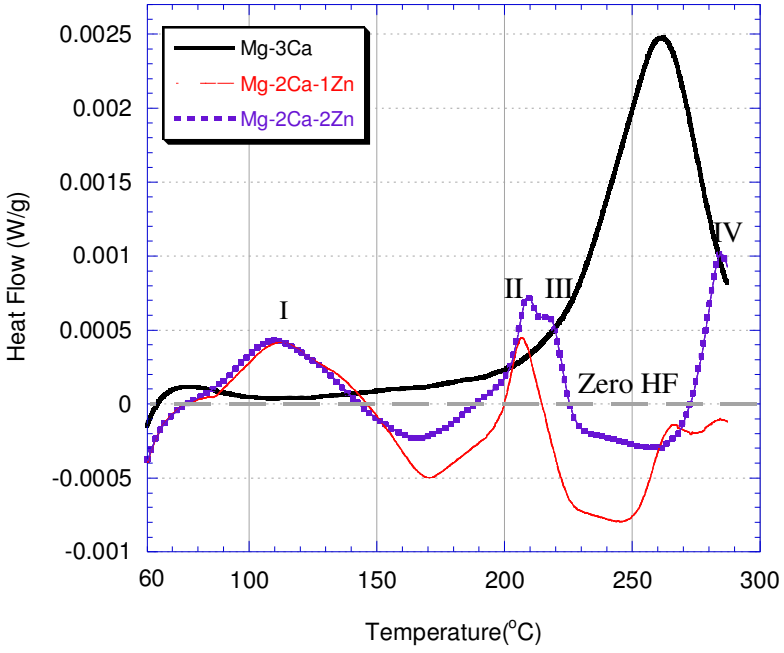


Figure 6.20: DSC traces of Mg-Ca-Zn alloys in the temperature range over 60°C -300°C.

# Chapter 7
# Conclusions and Suggestions for the Future Work

## 7.1 Conclusions

The goals of the present investigation were to (a) study the microstructural evolution during heat treatment and (b) assess precipitation hardening behavior of Mg-Ca-Zn alloys. The goals were achieved by a systematic study involving optical and electron microscopy, hardness measurements, DSC and IC and XRD analysis. The important conclusions of this work are as follows:

- Microstructure of the as-cast Mg-2.5Ca is comprised of dendritic structure of α-Mg and lamellar eutectic of α-Mg+$Mg_2Ca$ within dendrites. Homogenization has resulted in the formation of magnesium grains and $Mg_2Ca$ particles within the grains and at the grain boundaries. EDS studies confirmed the small solubility of Ca in the Mg matrix. The calculation of the diffusion distance and the microscopy results have confirmed the effectiveness of the homogenization practice in eliminating the dendritic structure.

- Aging response of the binary alloy at 175°C, 200°C and 220°C is investigated. In all three aging temperatures only a slight increase in hardness is obtained, i.e. from 50 VHN in the homogenized condition to approximately 53 VHN in the peak hardness condition. This is related to the precipitation behavior of the alloy and the lack of evidence for the formation of coherent precipitates. It is suggested that the precipitate formed in the binary alloy is the equilibrium $Mg_2Ca$.

- Microsrtucture of the as-cast ternary alloys, Mg-2Ca-1Zn and Mg-2Ca-2Zn, are comprised of primary α-Mg dendrites with interdendritic regions comprised of multiple phases including $Mg_2Ca$ and $Ca_2Mg_6Zn_3$.

- During homogenization of the ternary alloys, as a result of diffusion, the dendritic microstructure of α-Mg changes to the magnesium grains with Ca and Zn containing particles at the grain boundaries. The EDS results do not detect major difference in the calcium content of magnesium grains after homogenization heat treatment, confirming the low solubility of Ca in the magnesium matrix. The calculation of the diffusion distances suggested that Zn diffusion plays an important role in the solid-state processes that occur during homogenization.

- As a result of adding zinc to the binary Mg-Ca alloy, the aging response is enhanced in the ternary alloys. Aging curves show a peak hardness of approximately 70VHN at the three aging temperatures of 175°C, 200°C and 220°C for both alloys. Hardness increase in the peak-aged condition from the as-homogenized condition is approximately 14 VHN. This is attributed to formation of coherent precipitates which are likely to hinder dislocation movement much more effectively. The effect of Zinc in increasing hardness is in agreement with the results reported on similar alloys in the literature.

- In aging curves of the ternary alloys, three regions of under-aged, peak-aged and over-aged conditions are identified. Increasing aging temperature from 175°C to 220°C has substantially reduced the time to the peak-hardness from approximately

8 hours to 1 hour in both alloys. This suggests faster rates of precipitate formation at higher temperatures. No decrease in peak hardness, however, is seen as a result of aging at higher temperatures. The time required to reach the peak-aged condition from the microhardness measurements is in good agreement with the time to reach the baseline heat flow during isothermal calorimetry experiments at the tested aging temperatures.

- Isothermal calorimetry traces of the ternary alloys are used to determine the parameters for the kinetics of precipitation in these alloys. The kinetics of precipitation is modeled using the IC traces and the JMAK model. The JMAK parameter n is close for both ternary alloys while the apparent activation energy, Q, was found to be lower in Mg-2Ca-2Zn alloy (92 kJ/mol compared to 111 kJ/mol for the Mg-2Ca-1Zn alloy).
- The isothermal calorimetry experiments suggested the formation of more than one phase during isothermal aging of the ternary alloys. Similarly, the DSC results confirm that the ternary alloys undergo multiple precipitation processes during a non-isothermal aging process, while the binary alloy shows only one precipitation peak.
- The combined DSC-hardness results provide interesting information on the hardening effect of the precipitation processes in each of the alloys studied in this work.

## 7.2 Suggestions for the Future Work

The recommendations to further study microstructural characteristics and aging response of the alloys are summarized as follows:

- TEM investigations of the as-cast and homogenized alloys are recommended. In the binary alloy it will help determine microstructural changes in the eutectic mixture. In the case of ternary alloys, studying grain boundary particles after homogenization heat treatment with the aid of diffraction patterns, will determine how zinc participate in the Laves phases in these particle.

- For each alloy of the present investigation, with aid of presented hardness evolution during DSC, shape and orientation relationships of the hardening phase can be determined by TEM investigations.

- The sample used for the isothermal calorimetry trace of the binary Mg-3Ca at 220°C, is suggested be studied by the TEM to investigate whether precipitation occurs homogeneously within α-Mg grains or the large exothermic heat effect at this temperature is due to precipitation on already available $Mg_2Ca$ particles. It will also help determine number density of precipitates and orientation relationship of $Mg_2Ca$ with the magnesium matrix. Either IC samples of the ternary alloys at 200°C or 220°C is suggested be studied by TEM to investigate precipitates evolved during the IC test. This will shed light on the number density and types of precipitates and that evolve during aging.

- The role of calcium in the precipitation response of the ternary alloys can be determined by studying the hardness evolution in the alloys containing higher percentages of calcium, i.e. higher calcium content than 2.5 wt%.
- Tensile tests on the homogenized and aged samples are suggested be performed to study effect of aging on the mechanical behavior of the alloys of the present investigation.

# References


Aaronson HI and Legoues FK. (1992), Metallurgical Transactions A, 23A: 1915.

AIST,site viewed on:
http://www.aist.go.jp/aist_e/research_units/research_section/mrisus/mrisus_main.html.

Aghion E, Bronfin B, Von Buch F, Schumann S and Friedrich H. (2003), Journal of Metals, 30.

Ashby MF and Jones DRH. (2006), Engineering Materials 2- an Introduction to Microstructures, Processing and Design, 3rd ed., Butterworth-Heinemann, Oxford, UK.

Avrami M. (1939), Journal of Chemical Physics, 9: 1103.

Bamberger M, Levi G and Vander Sande JB. (2005), Metallurgical and Materials Transactions A, 37A: 481.

Berkenpas MB, Barnard JA, Ramanujan RV and Aaronson HI. (1986), Scripta Metall, 20: 323.

Bettles CJ and Gibson MA. (2005), Journal of Metals, 46.

Bettles CJ, Gibson MA and Venkatesan K. (2004), Scripta Materialia, 51:193.

Borg RJ and Dienes GJ. (1988), an Introduction to Solid State Diffusion, Academic Press, San Diego, CA, USA.

Brown MA and Ashby MF. (1980), Acta Metallurgica, 28:1085.

Brubaker CO and Liu ZK. (2004), Journal of Alloys and Compounds, 370: 114.

Cahn RW and Hassen P. (1983), Physical Metallurgy, 3rd ed., North-Holland Physics Publishing, Amsterdam, Netherlands.

Celotto S. (2000), Acta Materialia, 48:1775.

Clark JB. (1968), Acta Metallurgica, 16:141.

Clark JB. (1965), Acta Metallurgica, 13: 1281

Cluff D and Esmaeili S. (2008), Journal of Materials Science, 43: 1121.

Cohen S, Goren-Muginstein G, Avraham S, Rashokova B, Dehm G and M.Bamberger (2005), Z.Metallkd, 96:9:1081.

Cottrell A. (1998), Concepts in the Electron Theory of Alloys, IOM Communications, London, UK.

Courtney TH. (2000), Mechanical Behaviour of Materials, 2nd ed., McGraw-Hill, Boston, MA, USA.

Das S. (2003), Journal of Metals, pp:22.

Doherty RD. (1996), in Physical Metallurgy, 4th ed., eds., Cahn RW and Hassen P., Vol. 2, North Holland, Amsterdam.

Embury JD and Nicholson RB. (1965), Acta Metallurgica, 13: 403.

Esmaeili S, Vaumousee D, Zandbergen MW, Poole WJ, Cerezo A and Lloyd DJ. (2007), Philosophical Magazine, 85: 25: 3797.

Esmaeili S and Lloyd DJ. (2006), Materials Science Forum, 519:169.

Esmaeili S and Lloyd DJ. (2005. a), Acta Materialia , 53:5257.

Esmaeili S and Lloyd DJ (2005. b); Materials Characterization; 55; 307-319.

Esmaeili S and Lloyd DJ. (2004), Scripta Materialia , 50:155.

Esmaeili S, Lloyd DJ and Poole WJ. (2003. a), Acta Materialia, 51:2243.

Esmaeili S, Lloyd DJ and Poole WJ. (2003. b), Acta Materialia, 51:3467.

Esmaeili S. (2002), *Precipitation Hardening Behaviour of AA6111*, Vancouver, The University of British Columbia, Department of Metals and Materials Engineering, Ph.D. thesis.

Finkel A, Shepeleva L, Bamberger M, Rabkin E. (2006), Z.Metallkd; 97:1:64.

Fores FH, Eliezer D and Aghion E. (1998), Journal of Metals, 30.

Gao N, Starink MJ, Davin L, Cerezo A,Wang SC and Gregson PJ. (2005), Materials Science and Technology, 21: 9: 1010.

Gao X and Nie JF. (2007), Scripta Materialia, 56: 8: 645.

Gao X, Zhu SM, Muddle BC and Nie JF. (2005), Scripta Materialia, 53:1321.

Gladman T. (1999), Materials Science and Technology, 15: 30.

Glicksman ME. (2000), Diffusion in Solids- Field Theory, Solid-State Principles and Applications, John Wiley and Sons, New York, NY, USA.

Goldstein J, Newbury DE, Echlin P, Joy DC, Fiori C, Lifshin E. (1981), Scanning Electron Microscopy and X-ray Microanalysis, Plenum Press, New York, NY, USA.

Gupta D, Vieregee K and Gust W. (1998), Acta Materialia, 47:5.

Han Q, Kad BK and Viswanathan S. (2004), Philosophical Magazine, 84: 36: 3843.

Hassen P. (1996), Physical Metallurgy, 3rd ed., Cambridge University Press, Cambridge, UK.

Harosh S, Miller L, Levi G and Bamberger M (2007), Journal of Materials Science, 42: 9983.

Hort N, Huang Y and Kainer KU. (2006), Advanced Engineering Materials, 8: 4: 235.

Hosford WF. (2005), Physical Metallurgy, CRC Press, Taylor and Francis Group, Boca Raton, FL,USA.

Hosford WF. (2007), Materials Science: an Intermediate Text, Cambridge University Press, New York, NY, USA.

Hutchinson CR, NIE JF and Gorsse S. (2005), Metallurgical and Materials Transactions A, 36A: 2093.

Jackson KA. (2004), Kinetic Processes- Crystal Growth, Diffusion, and Phase Transitions in Materials, Wiley-VCH, Weinheim, Germany.

Jardim PM, Solorzano G and Vander Sande JB. (2004), Materials Science and Engineering A, 381: 196.

Jardim PM, Solorzano G and Vander Sande JB. (2002), Microscopy and Microanalysis, 8: 487.

King JF. (2007), Materials Science and Technology, 23: 1: 1.

Knipling KE, Dunand DC and Seidman DN. (2006), Z.Metallkd., 97:3:246.

Kurz W and Fisher DJ. (1989), Fundamentals of Solidification, 3rd ed.,Trans Tech Publications Ltd, Switzerland.

Langelier B and Esmaeili S. (2006), University of Waterloo, Department of Mechanical and Mechatronics Engineering, unpublished results.

Larionova TV, Park WW and You BS. (2001), Scripta Materialia, 45: 7.

Levi G, Avraham S, Zilberov A and Bamberger M. (2006), Acta Materialia 54:523.

Lloyd DJ, Evans DR and Gupta AK. (2000), Canadian Metallurgical Quarterly, 39: 4: 475.

Manning JR. (1968), Diffusion Kinetics for Atoms in Crystals, D.Van Nostrand Company, Princeton, NJ, USA.

Mendis CL, Bettels CJ, Gibson MA, Goresse S and Hutchinson (2006), Philosophical Magazine, 86: 7: 443.

Mendis CL, Bettels CJ, Gibson MA and Hutchinson CR (2006), Materials Science and Engineering A, 435: 163.

Montgomery DC, Runger GC and Hubele NF. (1998), Engineering Statistics, John Wiley and Sons, New York, NY, USA.

Mordike BL and Ebert. (2001), Materials Science and Engineering A, 302: 37.

Nayeb-Hashemi AA and Clark JB. (1988), Alloy Phase Diagrams, ASM Metals Handbook, Vol 3.

Nembach E. (1997), Particle Strengthening of Metals, John Wiley and Sons, New York, NY, USA.

Nie JF. (2003); Scripta Materialia, 48:1009.

Nie JF and Muddle BC. (1997), Scripta Materialia, 37:10:1475.

Oh JC, Ohkubo T, Mukai T and Hono K. (2005), Scripta Materialia, 53: 675.

Padfield TV. (2004), Metallography and Microstructures of Magnesium and its Alloy, ASM Metals Handbook Vol.9.

Papon P, Leblond J and Meijer PHE. (2006), The Physics of Phase Transitions- Concepts and Applications, 2nd ed., Springer, Netherlands.

Peckner D. (1964), The Strengthening of Metals, Reinhold Publishing Corporation, New York, NY, USA.

Ping DH, Hono K and Nie JF. (2003), Scripta Materialia, 48: 1017.

Poetter D. (2006), Engineering Diploma, University Paderbrn, Germany.

Polmear I. (2006), Light Alloys from Traditional Alloys to Nanocrystals, 4th ed., Butterworth-Heinemann, Oxford, UK.

Reed-Hill RE and Abbaschian R. (1991), Physical Metallurgy Principles, 3rd ed., PWS Publishing Company, Boston, MA, USA.

Rostoker W and Dvorak. (1977), Interpretation of Metallographic Structures, 2nd ed., Academic Press, New York, NY, USA.

Sepehrband P and Esmaeili S (2008)., "Application of Recently-Developed Approaches to Microstructural Characterization and Yield Strength Modeling of Aluminum Alloy AA7030", in print, Materials Science and Engineering A.

Shercliff HR and Ashby MF. (1990), Acta Metall. Mater, 38: 10: 1789.

Smallman RE. (1985), Modern Physical Metallurgy, 4th ed., Anchor-Brendon, Tiptree, Essex, UK.
Song GS and Kral MV. (2005), Materials Characterization, 54:279.

Starink MJ, Gao N, Davin L, Yan J and Cerezo A. (2005), Philosophical Magazine, 85:13:1395.

Starink MJ. (2001), Journal of Materials Science, 36:4433.

Starink MJ and Zahra AM. (1998), Philosophical Magazine A, 77: 1: 187.

Suzuki A, Saddock ND, TerBush JR, Powell BR, Jones JW and Pollock TM. (2007), Magnesium Technology 2007, TMS.

Suzuki A, Saddock ND, Jones JW and Pollock TM. (2005), Acta Materialia, 53:2823.

Suzuki A, Saddock ND, Jones JW and Pollock TM. (2004), Scripta Materialia, 51:1005.

Villars P and Calvert LD. (1985), Pearson's Handbook of Crystallographic Data for Intermetallic Phases, ASM, Metals Park, OH, USA.
Warren BE. (1969), X-ray Diffraction, Addison-Wesley Publishing Company, USA.

Watari H (2006), Japanese Science and Technology Quarterly Report, No. 18, www.nistep.go.jp.

Weiss D, Kaya AA, Aghion E and Eliezer D (2002), Journal of Materials Science, 37: 5371.

Westbrook JH. (1967), Intermetallic Compounds, Wiely, NewYork, NY, USA.

Westbrook JH and Fleisher RL. (1995), Intermetallic Compounds- Principles and Practice, Volume 1- Principles, John Wiley and Sons, Chichester, Sussex, UK.

Witte F, Kaese V, Haferkamp H, Switzer E, Mayer-Linderberg A, Wirth CJ and Winderhagen H. (2005), Biomaterials, 26: 3557.

You BS, Park WW and Chung IS. (2000), Scripta Materialia, 42: 1089.

Zhong Y. Investigation in Mg-Al-Ca-Sr-Zn Sytem by Computational Thermodynamics Approach Coupled with First Principles Energetics and Experimnets, The Pennsylvania State University, Department of Metals and Materials Engineering, PhD Thesis.